HYDRAULIC FRACTURE INITIATION AND PROPAGATION UNDER SUBCRITICAL CONDITIONS

by

Guanyi Lu

B.E. in Civil Engineering, Tongji University, China, 2009

Submitted to the Graduate Faculty of

the Swanson School of Engineering in partial fulfillment

of the requirements for the degree of

Doctor of Philosophy

University of Pittsburgh

2018

UNIVERSITY OF PITTSBURGH

SWANSON SCHOOL OF ENGINEERING

This dissertation was presented

by

Guanyi Lu

It was defended on

October 31, 2017

and approved by

Andrew P. Bunger, Ph.D., Assistant Professor, Department of Civil and Environmental Engineering & Department of Chemical and Petroleum Engineering

Jeen-Shang Lin, Ph.D., Associate Professor, Department of Civil and Environmental Engineering

Hao Sun, Ph.D., Assistant Professor, Department of Civil and Environmental Engineering

William Slaughter, Ph.D., Associate Professor, Department of Mechanical Engineering & Materials Science

Dissertation Director: Andrew P. Bunger, Ph.D., Assistant Professor, Department of Civil and Environmental Engineering & Department of Chemical and Petroleum Engineering

HYDRAULIC FRACTURE INITIATION AND PROPAGATION UNDER SUBCRITICAL CONDITIONS

Guanyi Lu, PhD

University of Pittsburgh, 2018

Multi-stage hydraulic fracturing (HF) is an essential technology for completion of horizontal wells in unconventional hydrocarbon reservoirs. In engineering design for multi-stage HF treatments of horizontal well stimulation, it is ideal to promote simultaneous growth of all fractures in each stage in order to reduce the number of non-producing perforation clusters. While increased attention has been given to studies of multiple HF growth, subcritical crack growth is not typically considered as a factor affecting the HF process. However, laboratory experiments have shown that subcritical crack growth plays a pivotal role in the initiation of hydraulic fracture(s).

Inspired by laboratory observations, this research is aimed at the study of the behavior of single/multiple hydraulic fracture(s) under subcritical growth conditions. This work consists of three main parts. First, a numerical model accounting for the subcritical crack growth is developed for simulating the initiation and propagation of single hydraulic fracture. It is seen that subcritical crack growth leads to significant changes in both the evolution of crack length and the wellbore peak pressure. Then, this model is extended to the case of simultaneous growth of multiple hydraulic fractures. A parametric study is carried out to investigate the competition between the effect of stress shadowing and subcritical crack growth. Finally, laboratory HF experiments are performed to explore the occurrence of time-dependent HF initiation in various rocks.

By showing the existence of time-dependent HF initiation and explaining that its underlying mechanism is due to the stable growth of the hydraulic fracture under subcritical

conditions, this research leads to new insights for promoting more evenly growth of multiple hydraulic fractures in multi-stage HF treatments. Most importantly, this work shows that reducing the subcritical index shortens the time delay associated with hydraulic fracture initiation at wellbore pressures that are insufficient to induce instantaneous initiation. The experiments show that choice of fluid can impact the effective subcritical index, thereby leading to the practically-relevant outcome that fluid(s) can be chosen in order to promote initiation and growth of multiple hydraulic fractures and/or single hydraulic fractures under conditions where the required wellbore pressure for instantaneous initiation cannot be reached.

TABLE OF CONTENTS

LIST OF TABLES

LIST OF FIGURES

PREFACE

To numerous people who have helped me during my PhD study, I wish to express my heartfelt gratitude. The achievements I have made today would not have been possible without your support and encouragement.

I would like to thank my advisor, Dr. Andrew Bunger, who provided me the opportunity to work on this exciting and challenging research topic. Thank you for broadening my horizons in this amazing scientific field, guiding me into the right path, and encouraging me to think independently. Andrew's contributions to this work, through our numerous discussions are greatly appreciated. Working together with him has been a wonderful experience that I will always cherish. Thanks also to the other members in my committee, Dr. Jeen-Shang Lin, Dr. William Slaughter, and Dr. Hao Sun, for providing their valuable suggestions and helping me to improve my research.

Financial support from Schlumberger is gratefully acknowledged. I want to thank my colleagues at Schlumberger, Dr. Romain Prioul, Dr. Elizaveta Gordeliy, and Dr. Gallyam Aidagulov. Their inputs into this work are substantial. It is a privilege for me to work together with these professionals that I have learned quite a lot from each of them.

I gratefully acknowledge the contributions to this work by my coleagues at University of Pittsburgh, Charles Hager (Scooter), Efosa Uwaifo, Qihang Ou, Victor Hugo Meireles, Brandon Ames, and Jesse Rippole. Each of them has a particular impact on this research. Moreover, I would like to thank my fellow graduate students in our research group, Navid Zolfaghari, Pengju Xing, Wei Fu, Qiao Lu, Di Wang, Delal Gunaydin, Yao Huang, and Yunxing Lu. I appreciate the research discussions in the office, as well as I cherish our friendship.

I am also grateful to my parents for raising me in a home filled with happiness, for building up the atmosphere of study and showing me the elegance of reasoning and devising in engineering when I was a child, and most importantly, for always being so supportive to every single choice I have made in my life. Last but not least, I wish to thank my excellent wife, Lijia Lu, for giving up her promising career in China and moving together with me to the United States, and for believing in me and giving me encouragement whenever I needed it. Lijia's kindness and enthusiasm has been and will always be inspiring me to be a better person.

I. INTRODUCTION

Multi-stage hydraulic fracturing (HF) is a widely used technique in stimulation of oil and gas production from horizontal wellbores. Typically, the well is stimulated in stages. In each fracturing stage, fluid is continuously injected into an isolated section along the well with goal of inducing the simultaneous initiation and propagation of multiple hydraulic fractures. This technology has been proven to be both useful and far from optimal. Numerical simulators therefore play a key role by allowing explanation of the impact on pumping parameters, rock properties, and so forth on the effectiveness of a proposed stimulation. However, predicting the propagation of multiple fractures is challenging since it depends on the interplay among various factors such as the stress shadowing effect, the partitioning of the influx to each fracture, and the coupled fluid flow with elastic deformation in the cracks. To address these challenges, numerous research activities have been undertaken to address the problem of the initiation and subsequent growth of single/multiple hydraulic fracture(s) and to understand the physical mechanisms governing the HF process (Abbas and Lecampion, 2013; Abbas et al., 2013; Bunger, 2013; Bunger et al., 2014, 2010, 2012; Detournay and Carbonell, 1997; Haimson and Fairhurst, 1967; Hubbert and Willis, 1957; Lakirouhani et al., 2016; Lecampion and Desroches, 2015; Peirce and Bunger, 2015; Wu and Olson, 2016). In these studies, the effect of various factors (e.g., compressibility of the injection system, in-situ stresses, fluid viscosity, borehole radius, stress interference among multiple fractures, and the perforation friction) on HF initiation and propagation has been investigated. Nevertheless, a long recognized but often ignored characteristic of rock, namely, time-dependent breakage and/or subcritical crack growth, has only recently been considered. Conventional approaches to solve the HF problem assume no fracture initiation before some critical condition is met. Such critical conditions include a requirement that the maximum induced tensile stress

meets or exceeds the tensile strength of the rock (Haimson and Fairhurst, 1967; Hubbert and Willis, 1957), that the Mode I stress intensity factor equals the fracture toughness of the rock (Abbas and Lecampion, 2013; Bunger et al., 2010; Detournay and Carbonell, 1997; Lakirouhani et al., 2016; Lecampion and Desroches, 2015), and/or the crack is able to propagate through satisfaction of a traction-separation failure condition applied to a cohesive zone at the leading edge (Lecampion, 2012b). However, numerous studies show that rocks can be caused to fail after a period of time when subjected to stresses that are insufficient to satisfy a critical (instantaneous) failure criterion (Atkinson, 1984; Cruden, 1974; Fernau et al., 2016; Kear and Bunger, 2014; Lu et al., 2015; Scholz, 1972). Furthermore, laboratory HF experiments on granite (Lu et al., 2015) have shown that a wellbore pressure that is lower than the critical value required for instantaneous HF initiation can lead to breakdown in a delayed manner. This phenomenon, referred to as time-dependent HF initiation, is argued by Bunger and Lu (2015) as one of the fundamental mechanisms for simultaneous generation of multiple hydraulic fractures, and has a significant impact on the propagation of the fractures, especially in an early stage of the HF growth (Lu et al., 2017a).

This work aims to demonstrate the occurrence of time-dependent initiation of HF by both numerical simulation and laboratory experiments. Numerical models are firstly developed for the initiation and propagation of single and multiple hydraulic fracture(s) under subcritical conditions. Unlike conventional numerical models for hydraulic fracture growth that impose a propagation condition based on Linear Elastic Fracture Mechanics, in which crack growth only occurs when the stress intensity factor, K_{I}, achieves a value euqal to the material fracture toughness, K_{IC}, we allow the fractures to propagate under subcritical conditions ($K_I < K_{\mathrm{IC}}$). Such crack growth is governed by an empirical power law, referred to as the subcritical crack growth law (Atkinson, 1984; Charles, 1958), for describing the relation between the fracture tip velocity, V, and the stress intensity factor, K_{I}

$$V = A\left(\frac{K_{\mathrm{I}}}{K_{\mathrm{IC}}}\right)^{n} \tag{I.1}$$

where n is the subcritical crack growth index, and A is a constant characteristic velocity typically taken as an upper bound on the crack propagation speed when $K_I \to K_{\mathrm{IC}}$. Using the subcritical crack growth law (Eq. I.1), numerical simulation is carried out for solving

the problems of single/multiple HF propagation. Furthermore, the influence of subcritical crack growth, as well as other factors are studied.

Once this model has been developed and its implications for multiple HF growth are shown, the approach is validated relative to laboratory experiments. Specifically, the existence of time-dependent HF initiation is examined by laboratory HF experiments on granite, sandstone, and limestone specimens. The experiments show that by maintaining a subcritical wellbore pressure (lower than the pre-determined instantaneous breakdown pressure), HF initiation can be achieved after some period of time. More importantly, this time duration of HF breakdown is shown to be correlated with the wellbore pressure. By comparing the experimental data with the numerical prediction obtained from the subcritical HF model, good agreement is found in this lifetime versus wellbore pressure correlation. Thus, the occurrence of time-dependent initiation is demonstrated and well explained by the theory of subcritical crack growth. Moreover, key factors impacting the behavior of delayed initiation, such as the fluid viscosity and the confining stresses are further investigated. The results reveal a possible dependence of the value of subcritical index on the viscosity of the injected fluid, as well as the applied confining stresses. This finding suggests that the choice of the injection fluid, and in-situ stress condition can profoundly influence both the initiation and growth of hydraulic fracture(s).

II. MODELING INITIATION AND PROPAGATION OF A HYDRAULIC FRACTURE UNDER SUBCRITICAL CONDITIONS

A. PREAMBLE

This chapter consists of a preprint of Lu et al. (2017a). Here, the goal is to develop a numerical simulatior for solving the problem of initiation and propagation of a single hydraulic fracture under subcritical conditions. The results are firstly verified against available analytical and numerical solutions. Then the numerical model is used to study the behavior of time-dependent initiation and the impact of the main factors on growth of a single hydraulic fracture.

B. ABSTRACT

A numerical model has been developed for simulating the initiation and propagation of a plane strain or axisymmetric hydraulic fracture from an openhole wellbore in an impermeable homogeneous rock formation. The main novelty is inclusion of a subcritical growth law, thereby allowing consideration of hydraulic fracture growth when the wellbore pressure is otherwise considered insufficient to initiate fracturing. To enable tracking the moving crack front in the simulations, we develop a new tip asymptotics based on a subcritical crack growth law. The results are first validated against available analytical solutions for plane strain and axisymmetric hydraulic fractures. A comparison is presented between the solutions of the subcritical growth model and a conventional hydraulic fracture model in which fracture growth is not allowed until the stress intensity factor equals the fracture toughness

of the rock. This comparison, as well as a study of the influence of the relevant parameters appearing in the subcritical growth law, indicates significant influence of subcritical growth on the evolution of the crack length and the wellbore pressure. Notably, this model provides the capability to simulate delayed growth of hydraulic fractures under pressures that are insufficient to generate instantaneous growth, which is a behavior observed in experiments but not considered by conventional hydraulic fracturing models.

C. INTRODUCTION

Hydraulic fracturing is a widely used technique for stimulation of oil and gas production from subsurface reservoirs. Predicting the initiation of hydraulic fractures (HFs) is important for a variety of reasons, including the interpretation of pressure records to estimate in situ stresses (e.g. Haimson and Fairhurst, 1969; Haimson and Cornet, 2003), relating laboratory experiments to field-scale applications (e.g. Lhomme et al., 2005), and predicting/promoting conditions for initiation of multiple hydraulic fractures from different locations along a well (Bunger and Lu, 2015). Simulating HF initiation is also challenging, involving interplay among compressibility of the injection system, viscous fluid flow, and the stress field surrounding a wellbore (Abbas and Lecampion, 2013; Bunger et al., 2010; Lhomme et al., 2005).

In the conventional approach, the HF is taken to initiate and propagate under the condition that the mode I (opening) stress intensity factor, K_{I}, reaches the value of the critical stress intensity factor or the fracture toughness, K_{IC}. Such a model predicts that no fracturing will occur until $K_I = K_{\mathrm{IC}}$. However, there is evidence that fractures can propagate under stresses that are insufficient to satisfy this condition, with velocities several orders of magnitude smaller than the rupture velocity (Atkinson, 1984, 1987). This phenomenon is known as subcritical crack growth, and it has long been considered an important aspect of the failure of rocks, especially in geoscience applications such as prediction of the development of natural fracture sets in rocks (Gale et al., 2007; Holder et al., 2001; Olson, 1993, 2004).

Subcritical growth is also implied by laboratory experiments on HF initiation and growth. Results from laboratory HF experiments with acoustic emission (AE) detection devices on crystalline rock (Bunger et al., 2015) show that microseismic events take place prior to peak pressure. Hydraulic fracturing experiments on granite (Lu et al., 2015) also show that a wellbore pressure that is lower than the critical pressure required for instantaneous initiation of hydraulic fractures can lead to hydraulic fracture growth in a delayed manner. Furthermore, it has been argued on theoretical grounds that the occurrence of subcritical initiation of HFs is vital for creating multiple hydraulic fractures that will grow ostensibly at the same time (Bunger and Lu, 2015). In turn, the ability to initiate and propagate multiple, simultaneous hydraulic fractures is one of the critical elements to the success of multistage hydraulic fracturing of horizontal wells (e.g. Fisher et al., 2004; Soliman et al., 1990), which is the technique widely credited with unlocking organic-rich shale gas and oil resources.

Hence, subcritical growth of HFs can be proposed as one of the processes at the core of the success of the shale resource revolution in the past two decades. However, it is rarely considered in relation to HF modeling in general and modeling of HF initiation in particular. Fully coupled HF initiation models that include injection system compressibility and near-wellbore stresses have not considered subcritical growth (Abbas and Lecampion, 2013; Abbas et al., 2013; Lakirouhani et al., 2016; Lhomme et al., 2005). When subcritical growth is considered, it is in the context of partially coupled (although useful in their own right) simulations wherein a temporally constant and spatially uniform pressure is imposed within the HFs (Olson and Dahi-Taleghani, 2009).

Including subcritical growth within the context of a fully coupled HF simulator is not only important, but it is also considerably challenging. The main challenge is associated with the modification of the conventional propagation criterion. In subcritical growth, the correspondence between the fracture tip velocity, V, and the stress intensity factor, K_{I}, can be described by an empirical power law (Charles, 1958)

$$V = A\left(\frac{K_{\mathrm{I}}}{K_{\mathrm{IC}}}\right)^{n} \tag{II.1}$$

where n is the subcritical crack growth index, and A is a constant. This equation has been used to examine time-dependent failures of various brittle materials (Atkinson, 1984; Charles,

1958; Evans, 1972; Swanson, 1984). In a purely fracture mechanics simulator (i.e., not related to hydraulic fracture and therefore not considering fluid injection and flow), the subcritical tip velocity V is the relevant characteristic velocity in the system. For HF simulation, the situation is different because coupling with fluid flow means that the algorithm must deal with a system that not only has a characteristic fracture velocity (V), but also a characteristic fluid velocity within the fracture that must, in turn, be compatible with fluid mass balance. In addition to demonstrating the potential importance of subcritical growth for HF initiation, overcoming this algorithmic challenge comprises one of the main contributions presented here.

This paper, then, presents a numerical model for the initiation and subsequent propagation of a single hydraulic fracture that accounts for the subcritical fracture growth (SCRIF, standing for "SubCRitical Initiation of hydraulic Fractures"). The fracture can be propagated under either plane strain or axisymmetric conditions. The structure of this paper is as follows. The problem formulation is described in Section II.D. In Section II.E, we present the scaling of the governing equations. The numerical algorithm for solving the nonlinear system and capturing the hydraulic fracture propagation is introduced in Section II.F. In Section II.G, we verify and analyze the results. Finally, discussion and concluding remarks are given in Section II.H.

D. PROBLEM FORMULATION

1. Model description

We consider the problem of the initiation and propagation of a single hydraulic fracture in an impermeable linearly elastic rock characterized by a Young's modulus E, a Poisson's ratio ν, and a fracture toughness K_{IC}. A Newtonian fluid with viscosity μ is injected at a constant rate Q_0 into the system with a finite compressibility U. Two geometries are studied in this problem, based on the orientation of the wellbore:

I. A longitudinal bi-wing fracture under plane strain conditions (Fig. II.1) with an initial length l_0 emanating from a vertical wellbore with the radius a under the minimum and maximum (or intermediate) in-situ stresses σ_h and σ_H (after Bunger et al., 2010; Lakirouhani et al., 2008).

II. An axisymmetric transverse fracture (Fig. II.2) propagating from a horizontal well under minimum in-situ stress σ_h, acting orthogonal to the fracture plane, with a non-negligible influence of the wellbore of radius a (after Abbas and Lecampion, 2013; Lecampion and Desroches, 2015).

In our model, the separation between the fracture tip and the fluid front is assumed to be very small compared to the fracture length (i.e., the so-called "fluid lag" is negligible in this problem). We also assume that the fracture remains planar. Fluid leak-off to the rock is assumed to be negligible. The validity of this assumption at the early stage of HF treatment is discussed in Appendix A.A. We thus seek a solution as a function of the coordinate x and time t, namely: the fracture length $l(t)$, the crack width $w(x,t)$, the wellbore pressure $p_w(t)$, and the net pressure $p_{net}(x,t) = p_f(x,t) - \sigma_n(x)$ acting on the fracture, where p_f and σ_n denote, correspondingly, the fluid pressure and the normal compressive stress induced by the in-situ stresses. In these expressions, x is the coordinate along the direction of crack propagation, and $x = 0$ corresponds to the center of the wellbore. Accordingly, we have $x \in (x_0, x_{tip})$ along the crack, where $x_0 = a$; $x_{tip} = l(t) + a$.

2. Governing equations

a. Propagation condition The conventional model assumes that the fracture propagates under quasi-static equilibrium, with $K_{\mathrm{I}} = K_{\mathrm{IC}}$, and that the asymptotic behavior of the fracture opening at the fracture tip is given by the classical square-root ("k") asymptote (Irwin, 1957),

$$w \sim \sqrt{\frac{32}{\pi}} \frac{K_{\mathrm{IC}}}{E'} (x_{tip} - x)^{1/2}, \quad x \to x_{tip} \tag{II.2}$$

where $E' = E/(1-\nu^2)$ is the plane strain elastic modulus. We refer to this behavior as the toughness (k) asymptote.

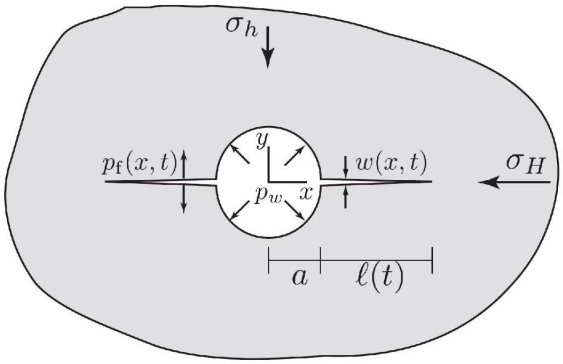

Figure II.1: A plane strain model of a longitudinal hydraulic fracture of length $l(t)$ propagating from a wellbore of radius a, drilled in the direction of intermediate (or maximum) far-field stress (after Bunger et al., 2010; Lakirouhani et al., 2008).

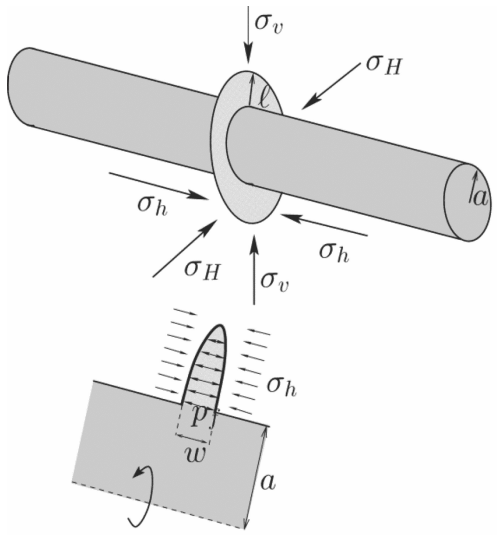

Figure II.2: An axisymmetric transverse fracture propagating from a wellbore drilled in the direction of minimum far-field stress (after Abbas and Lecampion, 2013; Lecampion and Desroches, 2015).

For the subcritical propagation criterion, $K_{\mathrm{I}} < K_{\mathrm{IC}}$, and the k asymptote (Eq. II.2) is instead given by

$$w \sim \sqrt{\frac{32}{\pi}} \frac{K_{\mathrm{I}}}{E'} (x_{tip} - x)^{1/2}, \quad x \to x_{tip}$$

Further, the tip velocity V is controlled by Eq. (II.1), which allows expression of K_{I} by rearranging Eq. (II.1), namely

$$K_{\mathrm{I}} = K_{\mathrm{IC}} \cdot \left(\frac{V}{A}\right)^{1/n}$$

By substitution, the modified k asymptote can be written as

$$w \sim \sqrt{\frac{32}{\pi}} \frac{K_{\mathrm{IC}}}{E'} (x_{tip} - x)^{1/2} \cdot \left(\frac{V}{A}\right)^{1/n}, \quad x \to x_{tip} \tag{II.3}$$

Hence, the subcritical growth can be accounted for in the solution method via a modification of the conventional k asymptote. In doing so, the propagation condition gains dependence on laboratory-determined subcritical growth parameters A and n, as well as an additional coupling with the global solution for the HF growth via the propagation velocity V. Put another way, because V is a part of the solution and not a prescribed parameter, the tip propagation condition is coupled to the global solution and so it is anticipated that an iterative solution will be required (indeed, this will be detailed later).

It is also worthwhile to note that there exists a lower limit for the stress intensity factor, K_{I}^*, at which the subcritical growth stops. Fig. II.3 shows the evolution of the crack tip velocity with the stress intensity factor (after Atkinson, 1987; Olson, 1993). Following Atkinson (1987) and Olson (1993), we assume that the crack starts to grow when $K_{\mathrm{I}} = K_{\mathrm{I}}^* = K_{\mathrm{IC}}/10$, and require that $K_{\mathrm{I}}^* \leq K_{\mathrm{I}} \leq K_{\mathrm{IC}}$ for the subcritical fracture propagation. Consequently, the velocity term in Eq. (II.3) has the range: $0.1^n \leq \frac{V}{A} \leq 1$, where the practical range of n for rocks is $10 \leq n \leq 200$ (Olson, 2004).

This modification of the propagation criterion is the main novelty of the model underlying the HF simulator presented here. The additional components of the model follow various past contributions, and are presented for the sake of completeness in the following subsections.

b. Linear elasticity For an axisymmetric fracture subject to a normal load and in the absence of a shear (tangential) load, the relation between the fracture width w and the net

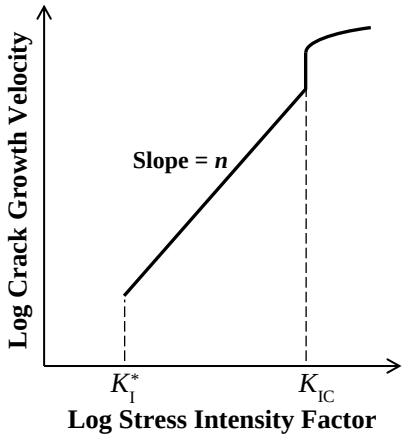

Figure II.3: Log-log plot of the crack tip velocity and the stress intensity factor (after Atkinson, 1987; Olson, 1993). Subcritical crack growth commences when K_I becomes larger than K_I^*.

pressure acting on the fracture is represented by a boundary integral equation, following the distributed dislocation formulation (Hills et al., 1996)

$$p_f(x,t) - \sigma_n(x) = \int_\Sigma h(x,x') \frac{\partial w}{\partial x'} dx' \tag{II.4}$$

where $\sigma_n = \sigma_h$ is the normal stress, and the integration is carried over Σ, which represents the crack (i.e., $\sum = \{x' : x' \in (x_0, x_{tip})\}$). In Eq. (II.4), the elastic kernel $h(x,x')$ represents the stress at x caused by an axisymmetric dislocation of radius x' in an infinite domain with the cylindrical cavity of radius a. The mathematical expression for this kernel was obtained in Keer et al. (1977) and is given in Appendix A.B. This integral kernel includes the wellbore effect directly.

For the plane strain model of a bi-wing fracture emanating from a circular wellbore, the displacement discontinuity (DD) formulation is used (Crouch and Starfield, 1983)

$$\begin{aligned} p_f(s,t) - \sigma_n(s) &= \int_\Sigma \left[H_{nn}(s,s') [u_n](s',t) + H_{ns}(s,s') [u_s](s',t) \right] ds' \\ 0 &= \int_\Sigma \left[H_{sn}(s,s') [u_n](s',t) + H_{ss}(s,s') [u_s](s',t) \right] ds' \end{aligned} \tag{II.5}$$

where $\sigma_n(s)$ is the normal compressive stress along the fracture resulting from the far-field stress, and the involved kernels H represent the stresses (normal or tangential) at s caused by a unit displacement discontinuity (normal or tangential) at point s'. In this case, the tangential displacement jump $[u_s]$ is included in addition to the normal displacement jump $[u_n]$ (equal to the crack width w along the crack), and the integration contour Σ is the union of the crack and the circular wellbore wall.

For the plane strain model, we use the integral kernels that do not account for the wellbore directly (Crouch and Starfield, 1983); therefore, the wellbore wall is included in the integration contour and is discretized by the DD elements as well as the crack, similarly as done in Zhang et al. (2011). We first decompose the total stress field in the plane strain problem (Fig. II.1) into a superposition of (i) the stress around a traction-free circular hole under biaxial far-field compression in an infinite plane without a fracture, and (ii) the stress around the pressurized circular hole (wellbore) and the pressurized fracture with zero far-field stress. The solution for the stress in problem (i) is given by the Kirsch solution (Kirsch, 1898). The solution for problem (ii) is then obtained by solving Eq. (II.5). According to such superposition, available due to the linearity of the elasticity problem, the total loading on the circular boundary of the wellbore in Eq. (II.5) is given by the fluid pressure p_f (equal to the wellbore pressure p_w). The influence of the wellbore pressure onto the bi-wing fracture is taken into account by the influence matrix according to the DD method, as shown in Appendix A.B. The normal stress $\sigma_n(s)$ acting on the plane of the HF growth, where $s = x$, is given by the Kirsch solution (Kirsch, 1898),

$$\sigma_n(x) = \sigma_h \left(1 + \frac{a^2}{x^2}\right) + \frac{\sigma_H - \sigma_h}{2} \left(\frac{a^2}{x^2} - 3\frac{a^4}{x^4}\right)$$

Further details of the integral kernels and the discretization of the boundary integral equations (II.4) and (II.5) for both geometries are given in Appendix A.B.

c. Lubrication The Poiseuille law for the fluid flux $q(x,t)$ is given by (e.g. Batchelor, 1967)

$$q = -\frac{w^3}{\mu'}\frac{\partial p_f}{\partial x} \quad \text{for} \quad x \in (x_0, x_{tip}) \tag{II.6}$$

where $\mu' = 12\mu$ for dynamic viscosity μ. The local continuity equation is derived based on the fluid mass balance

$$\frac{\partial w}{\partial t} + \frac{1}{x^{d-1}} \frac{\partial}{\partial x} \left(x^{d-1} q \right) = 0 \tag{II.7}$$

with $d = 1$ for plane strain and $d = 2$ for axisymmetry. The Reynolds' lubrication equation is then deduced by substituting Eq. (II.6) into Eq. (II.7):

$$\frac{\partial w}{\partial t} = \frac{1}{\mu' x^{d-1}} \frac{\partial}{\partial x} \left(x^{d-1} w^3 \frac{\partial p_f}{\partial x} \right) \tag{II.8}$$

d. Boundary and initial conditions The crack-tip boundary condition imposes vanishing fluid flux and fracture width at the fracture tip (Detournay and Peirce, 2014)

$$x = x_{tip} : \quad w\left(x,t\right) = 0, \quad q\left(x,t\right) = 0 \tag{II.9}$$

The inlet boundary condition for the fluid flux entering the fracture from the wellbore is derived from the mass balance accounting for the injection rate and the compressibility effect (Abbas and Lecampion, 2013; Lakirouhani et al., 2016; Lhomme et al., 2005)

$$x \to x_0 : \quad q\left(x,t\right) = \frac{1}{2\left(\pi x\right)^{d-1}} \left(Q_0 - U \frac{\mathrm{d}p_w}{\mathrm{d}t} \right) \tag{II.10}$$

where q is the fluid influx to the crack and Q_0 is the constant injection rate. U is the system compressibility (volumetric compliance of the injection system), which is computed by $U \approx c_f V_0$ where c_f is the fluid compressibility and V_0 is the injection system volume. (In practice, wellbore deformation may also contribute to the total system compressibility.) Note that the dimensions of Q_0 and U under the plane strain condition ($Q_0 \sim {}^{m^2}/_{\mathrm{s}}$; $U \sim {}^{\mathrm{m}^2}/_{\mathrm{Pa}}$) are different from those of an axisymmetric fracture ($Q_0 \sim {}^{m^3}/_{\mathrm{s}}$; $U \sim {}^{\mathrm{m}^3}/_{\mathrm{Pa}}$), because in the case of a plane strain crack, they represent the injection rate and the system compressibility per unit height.

Note also that although the injection system is compressible, we consider that the compressibility of the fluid has a negligible effect on the continuity equation (II.7). This assumption can be readily proven valid as long as the product of the fluid compressibility c_f with

the fluid net pressure, defined as $p_{net} = p_f - \sigma_h$, is small relative to one. (This definition of the net pressure is valid for the axisymmetric geometry; for plane strain, a similar argument would hold with the net pressure defined by $p_{net} = p_f - \sigma_n$.) To illustrate, consider the fluid density within the fracture to be given by

$$\rho(x,t) = \frac{\rho_0}{1 - c_f p_{net}(x,t)},$$

where ρ_0 is the density of the fluid when $p_f = \sigma_h$ ($p_{net} = 0$). Hence, it is clearly seen that the fluid density can be taken as a constant (ρ_0) throughout the domain of the HF and throughout time as long as $c_f p_{net} \ll 1$. For example, if we consider a typical upper bound on p_{net} in the order of tens of MPa, then neglecting compressibility of the fluid within the fracture is justified for most fluids including water (taking $c_f \approx 0.0002$ MPa^{-1}) and even supercritical CO_2 (taking $c_f \approx 0.005$ MPa^{-1} at typical reservoir temperature and pressure).

The initial condition at $t = 0$ is given by a small opening along the initial defect. As long as the opening is small enough, its details will not impact the final solution. Hence, for convenience, the initial condition is chosen as the pressure distribution p_f generating a small, uniform, positive net pressure acting along the interior faces of the initial crack, that is

$$t = 0: \quad p_f(x,t) = \sigma_n(x) + p_i, \;\; l = l_0 \quad (x_0 < x < x_0 + l_0) \tag{II.11}$$

where p_i is a small initial net pressure assumed to exist in the crack, and l_0 is the initial fracture length. Finally, taking into account the boundary conditions (II.9)and (II.10), a global volume balance equation can be derived by integrating the continuity equation (II.7) over time and space

$$2\int_{x_0}^{x_{tip}} (\pi x)^{d-1} \left(w(x,t) - w(x,0)\right) dx = Q_0 t - U\left(p_w(t) - p_w(0)\right) \tag{II.12}$$

E. SCALING

Here we introduce the dimensionless variables

$$\begin{gathered}\gamma=\frac{l}{l_*},\quad \mathcal{A}=\frac{a}{l_*},\qquad \xi=\frac{x}{l_*},\quad \Omega=\frac{w}{w_*},\qquad \Psi=\frac{q}{q_*},\quad \tau=\frac{t}{t_*};\\ \Phi_H=\frac{\sigma_H}{p_*},\quad \Phi_h=\frac{\sigma_h}{p_*},\quad \Phi_D=\frac{\sigma_H-\sigma_h}{p_*};\\ \Pi_w=\frac{p_w}{p_*},\quad \Pi_f=\frac{p_f}{p_*},\quad \Pi_{net}=\frac{p_{net}}{p_*}.\end{gathered}\tag{II.13}$$

where t_*, l_*, w_*, p_*, and q_* are the characteristic scales for time, length, crack width, net pressure, and fluid flux. Then we introduce the so-called compressibility-toughness (UK) scaling given by Bunger et al. (2010); Lakirouhani et al. (2008, 2016) for plane strain, and by Abbas and Lecampion (2013); Lhomme et al. (2005) for axisymmetric fractures. This scaling is based on the characteristic time and length scales associated with the release of the volume compressed in the injection system prior to fracture initiation. Therefore, when the fracture attains a length much greater than the characteristic length describe below, the impact of the compressed volume in the injection system vanishes. Similarly, when the injection time greatly exceeds the characteristic time described below, the impact of the compressed volume in the injection system vanishes. To find these characteristic quantities, the governing equations are rewritten in terms of the dimensionless variables (Eq. II.13) and the dimensionless groups that are combinations of the parameters K_{IC}, E', μ', Q_0 and U (Abbas and Lecampion, 2013). The dimensionless groups associated with injection rate, compressibility, and fracture toughness are set to be 1, and the characteristic scales can be obtained as follows

$$\begin{gathered}l_*=(E'U)^{\frac{1}{d+1}},\quad t_*=\sqrt{\frac{32}{\pi}}\frac{K_{\mathrm{IC}}U^{\frac{2d+1}{2d+2}}}{Q_0E'^{\frac{1}{2d+2}}},\quad p_*=\sqrt{\frac{32}{\pi}}\frac{K_{\mathrm{IC}}}{(E'U)^{\frac{1}{2d+2}}},\\ w_*=\sqrt{\frac{32}{\pi}}\frac{K_{\mathrm{IC}}U^{\frac{1}{2d+2}}}{E'^{\frac{2d+1}{2d+2}}},\quad q_*=\frac{Q_0}{(E'U)^{\frac{d-1}{d+1}}}.\end{gathered}\tag{II.14}$$

The corresponding dimensionless viscosity is

$$\mathcal{M}=\left(\frac{\pi}{32}\right)^2\frac{\mu'Q_0E'^{\frac{2d+4}{d+1}}}{K_{\mathrm{IC}}{}^4U^{\frac{d-1}{d+1}}}\tag{II.15}$$

and the dimensionless subcritical constant is given by

$$\alpha = \sqrt{\frac{32}{\pi}} \frac{U^{\frac{2d-1}{2d+2}} K_{\mathrm{IC}}}{E'^{\frac{3}{2d+2}} Q_0} A \tag{II.16}$$

Typical orders of magnitudes of the characteristic scales can be estimated by substitution of the actual ranges of the parameters based on typical field data into the above expressions: taking $A = O(10^3)$ $^m/_{\mathrm{s}}$ (using the O notation to indicate order of magnitude), $E = O(10^{10})$ Pa, $\sigma_H = O(10^7)$ Pa, $\sigma_h = O(10^7)$ Pa, $\nu \sim 0.3$, $K_{\mathrm{IC}} = O(10^6)$ $\mathrm{Pa} \cdot \mathrm{m}^{1/2}$, $U = O(10^{-11})$ $^{\mathrm{m}^2}/_{\mathrm{Pa}}$ ($^{\mathrm{m}^3}/_{\mathrm{Pa}}$), $\mu = O(10^{-3})$ $\mathrm{Pa} \cdot \mathrm{s}$, $a = O(10^{-2})$ m, and $Q_0 = O(10^{-3})$ $^{m^2}/_{\mathrm{s}}$ (plane strain) or $Q_0 = O(10^{-2})$ $^{m^3}/_{\mathrm{s}}$ (axisymmetry), the ranges of the characteristic scales and the dimensionless parameters are approximated as

$$l_* = O(1)\ \mathrm{m}, \quad t_* = O(0.1)\ \mathrm{second}, \quad p_* = O(10^7)\ \mathrm{Pa}, \quad w_* = O(10^{-4})\ \mathrm{m},$$
$$q_* = O(10^{-3})\ ^{m^2}/_{\mathrm{s}}, \quad \mathcal{M} = O(0.1), \quad \mathcal{A} = O(10^{-2}),$$
$$\alpha = O(100), \quad \Phi_H = O(1), \quad \Phi_h = O(1),$$

for plane strain, and

$$l_* = O(1)\ \mathrm{m}, \quad t_* = O(10^{-2})\ \mathrm{second}, \quad p_* = O(10^7)\ \mathrm{Pa}, \quad w_* = O(10^{-4})\ \mathrm{m},$$
$$q_* = O(10^{-2})\ ^{m^3}/_{\mathrm{s}}, \quad \mathcal{M} = O(1), \quad \mathcal{A} = O(10^{-2}),$$
$$\alpha = O(10), \quad \Phi_h = O(1),$$

for axisymmetry. Based on the scaling method, we can rewrite the governing equations and boundary and initial conditions in the following dimensionless form.

a. Elasticity For the axi-symmetric dislocation formulation, we get

$$\Pi_{net} = \int_{\Sigma} \hat{h}\left(\xi, \zeta\right) \frac{\partial \Omega}{\partial \zeta} d\zeta \tag{II.17}$$

where $\xi = \frac{x}{l_*}$ and $\zeta = \frac{x'}{l_*}$. The integral equation for the plane strain model with the DD kernels can be similarly formulated in the scaled form.

b. Poiseuille law The scaled Poiseuille law is given by

$$\Psi = -\frac{1}{\mathcal{M}}\Omega^3\frac{\partial \Pi_f}{\partial \xi} \quad \text{for } \xi \in (\xi_0, \xi_{tip}) \tag{II.18}$$

where $\xi_0 = \frac{x_0}{l_*}$ and $\xi_{tip} = \frac{x_{tip}}{l_*}$.

c. Continuity

$$\frac{\partial \Omega}{\partial \tau} + \frac{1}{\xi^{d-1}}\frac{\partial \bar{\Psi}}{\partial \xi} = 0 \tag{II.19}$$

in which the modified fluid flux is introduced as $\bar{\Psi} = \xi^{d-1}\Psi$.

d. Lubrication Scaling the lubrication equation results in

$$\frac{\partial \Omega}{\partial \tau} = \frac{1}{\mathcal{M}\xi^{d-1}}\frac{\partial}{\partial \xi}\left(\xi^{d-1}\Omega^3\frac{\partial \Pi_f}{\partial \xi}\right) \tag{II.20}$$

e. Propagation condition The propagation condition is given by

$$\Omega \sim (\xi_{tip} - \xi)^{1/2}\left(\frac{\upsilon}{\alpha}\right)^{1/n}, \quad \xi \to \xi_{tip}, \upsilon \leq \alpha \tag{II.21}$$

where $\upsilon = \frac{d\gamma}{d\tau}$ is the dimensionless fracture tip velocity. Recall that the subcritical model is used when the fracture is propagating under the condition that $K_{\mathrm{I}} < K_{\mathrm{IC}}$, which is expressed equivalently as the condition $\upsilon < \alpha$ after Eq. (II.21). Note, then, that in the algorithm, once the critical condition is reached, the tip asymptotics under the subcritical velocity criterion will immediately reduce to the classical propagation criterion using the k asymptote.

f. Fracture tip boundary condition The boundary condition at the tip is given by

$$\xi = \xi_{tip}: \quad \Omega(\xi, \tau) = 0, \quad \bar{\Psi}(\xi, \tau) = 0 \tag{II.22}$$

g. Inlet boundary condition The inlet boundary condition is

$$\xi \to \xi_0: \quad \bar{\Psi}(\xi, \tau) = \frac{1}{2\pi^{d-1}}\left(1 - \frac{\mathrm{d}\Pi_w}{\mathrm{d}\tau}\right) \tag{II.23}$$

h. Initial condition The initial condition is

$$\tau = 0: \quad \Pi_{net}(\xi, \tau) = \Pi_i, \quad \gamma = \gamma_0 \quad (\xi_0 < \xi < \xi_0 + \gamma_0) \tag{II.24}$$

where $\Pi_i = \frac{p_i}{p_*}$ is a small initial net pressure sufficient to slightly open the initial crack.

i. Global volume balance equation The scaled global volume balance is expressed as

$$2\int_{\xi_0}^{\xi_{tip}} (\pi\xi)^{d-1} \left(\Omega(\xi, \tau) - \Omega(\xi, 0)\right) d\xi = \tau - \left(\Pi_w(\tau) - \Pi_w(0)\right) \tag{II.25}$$

In summary, by applying the UK scaling, we are able to reduce the parametric space of this problem to a group of independent dimensionless parameters, which consists of the dimensionless viscosity $\mathcal{M}$, wellbore radius $\mathcal{A}$, minimum in-situ stress Φ_h (and deviatoric stress Φ_D for the plane strain case), initial crack length γ_0, subcritical index n, and the subcritical constant α. Thus, our solution $(\gamma, \Omega, \Pi, \Psi)$, considered as a function of spatial (ξ) and time (τ) variables, will depend on the values of these dimensionless parameters.

F. NUMERICAL ALGORITHM

1. Overview

The numerical solution for the problem described in Section II.E is obtained from an algorithm based on the DD method (Crouch and Starfield, 1983). The elastic equation (II.17) is discretized using a fixed grid of DD elements with a constant element size, $\triangle\xi$, and a 1D finite difference scheme is applied for discretizing the lubrication equation (II.20). Then the combined nonlinear system, resulting from the solid-fluid coupling, is solved by an iterative scheme following the spirit of Bunger (2005). For the initiation phase, we fix the initial crack length γ_0 and increase time by a fixed time increment $\Delta\tau_i$ for every time step, to find the time at which the fracture satisfies the initiation criterion ($K_{\mathrm{I}} = K_{\mathrm{I}}^* = K_{\mathrm{IC}}/10$) and starts to grow. As the fracture propagates, the fracture length is increased by a constant value, $\triangle\xi$, and the corresponding time step $\triangle\tau$, required to increase the crack length by this increment,

is found as a part of the numerical solution. Such a length-controlled algorithm is discussed in detail in Section II.F.4. At each time step, N denotes the number of the time step, m denotes the number of elements along the crack, k is the iteration counter in the solution of the coupled nonlinear system, and K is the iteration counter in the solution for the time step. This type of numerical algorithm, based on a fixed crack length increment at every time step, has been used in the past (Abbas and Lecampion, 2013; Bunger et al., 2010; Gordeliy and Detournay, 2011b; Lakirouhani et al., 2016). It is worthwhile to note that an alternative time-controlled algorithm has been developed in Peirce and Detournay (2008) and used, for example, in Gordeliy and Peirce (2013); Lecampion and Desroches (2015); Peirce and Detournay (2008) for modeling propagation of single and multiple hydraulic fractures, in which a given time increment is specified and the corresponding crack length is found using an implicit level-set algorithm. In our particular case, where there are neither stress jumps nor material interfaces, the length-controlled algorithm is favored because it can capture sudden changes in the crack length associated with release of compressed volume. A time-controlled algorithm can be inaccurate when the length suddenly changes in a very short time period.

2. Elasticity

We discretize the elasticity equation into a linear system using the DD method. The crack is discretized into a mesh of m piece-wise constant-strength DD elements, and additional elements are used to discretize the circular wellbore wall in the plane strain model. Each element i in the crack region with the midpoint coordinate $\xi_i = \xi_0 + (i - 1/2)\,\triangle\xi$ and $i = 1, ..., m$ is thus characterized by a constant width Ω_i. Assuming no leakoff and no fluid lag in the crack, the following correspondance between the vectors of the fluid pressure, $\mathbf{\Pi_f}$, and the fracture opening, $\mathbf{\Omega_f}$, corresponding to the midpoints of all crack elements, can be derived for both geometries

$$\mathbf{\Pi}_{\mathrm{f}} = \mathbf{C}\mathbf{\Omega_f} - \mathbf{S} \tag{II.26}$$

where $\mathbf{C}$ is the coefficient matrix with the values that depend on the problem geometry, and the vector $\mathbf{S}$ accounts for the normal stress acting on the fracture (see more details in Appendix A.B).

3. Lubrication

Reynolds' lubrication equation (II.20) is solved using a finite difference scheme. According to the Poiseuille law (II.18), the inlet boundary condition (II.23), and the zero-flux tip condition (II.22), the fluid flux $\bar{\Psi}_{i+1/2}$ at the boundary between the elements i and $i+1$ can be written as

$$\begin{aligned} \bar{\Psi}_{1/2} &= \tfrac{1}{2\pi^{d-1}}\left(1-\tfrac{\triangle\Pi_w}{\triangle\tau}\right), \\ \bar{\Psi}_{i+1/2} &= -K_i\left(\Pi_{i+1}-\Pi_i\right), \quad \text{for } i=1,\dots,m-1 \\ \bar{\Psi}_{m+1/2} &= 0 \end{aligned} \tag{II.27}$$

where $K_i = \xi_{i+1/2}^{d-1}\frac{1}{\mathcal{M}\triangle\xi}\left(\frac{\Omega_i+\Omega_{i+1}}{2}\right)^3$ and $\xi_{i+1/2} = \frac{\xi_i+\xi_{i+1}}{2}$. Using a backward difference approximation for the time derivatives and a central difference approximation for the spatial derivatives, the continuity equation (II.19) is discretized by

$$\frac{\Omega_i-\Omega_i^0}{\triangle\tau}+\frac{\bar{\Psi}_{i+1/2}-\bar{\Psi}_{i-1/2}}{\xi_i^{d-1}\triangle\xi}=0 \tag{II.28}$$

where Ω^0 denotes the known width at the previous time step τ^{N-1}. Hence the increment of the opening at ξ_i between the two consecutive time steps can be written as $\triangle\Omega_i = \Omega_i - \Omega_i^0$.

4. Coupled nonlinear system

Substitution of the discretized Poiseuille law (II.27) and the discretized elasticity equation (II.26) into the discretized continuity equation (II.28) yields the final form of the lubrication equation,

$$\boldsymbol{\Xi}\triangle\boldsymbol{\Omega}=\boldsymbol{\Gamma} \tag{II.29}$$

in which the matrix $\mathbf{\Xi}$ is given in the component form by $\Xi_{ij} = \delta_{ij} + \frac{\triangle\tau}{\Delta\xi}\frac{1}{\xi_i^{d-1}} Z_{ij}$, and

$$
\begin{aligned}
Z_{1j} &= K_1\left(-C_{2j} + C_{1j}\right) + \frac{1}{2\pi^{d-1}\triangle\tau} C_{1j}, \qquad \text{for } j = 1, \ldots, m && \text{(II.30)}\\
Z_{ij} &= K_i\left(-C_{i+1j} + C_{ij}\right) - K_{i-1}\left(-C_{ij} + C_{i-1j}\right), \\
&\quad \text{for } i = 2, \ldots, m-1; \;\; j = 1, \ldots, m && \text{(II.31)}\\
Z_{mj} &= -K_{m-1}\left(-C_{mj} + C_{m-1j}\right), \qquad \text{for } j = 1, \ldots, m && \text{(II.32)}
\end{aligned}
$$

and the vector Γ is expressed by

$$
\begin{aligned}
\Gamma_1 &= -\frac{\triangle\tau}{\xi_1^{d-1}\triangle\xi}\left[\sum_{j=1}^{m}\left(Z_{1j} - \frac{1}{2\pi^{d-1}\triangle\tau} C_{1j}\right)\Omega_j^0 - K_1\left(\varphi_1 - \varphi_2\right)\right] + \ldots \\
&\quad + \frac{\triangle\tau}{2\left(\xi_1\pi\right)^{d-1}\triangle\xi}, \; j = 1, \ldots, m && \text{(II.33)}\\
\Gamma_i &= -\frac{\triangle\tau}{\xi_i^{d-1}\triangle\xi}\left[\sum_{j=1}^{m} Z_{ij}\Omega_j^0 - K_i\left(\varphi_i - \varphi_{i+1}\right) - K_{i-1}\left(\varphi_i - \varphi_{i-1}\right)\right], \\
&\quad i = 2, \ldots, m-1; \;\; j = 1, \ldots, m && \text{(II.34)}\\
\Gamma_m &= -\frac{\triangle\tau}{\xi_m^{d-1}\triangle\xi}\left[\sum_{j=1}^{m} Z_{mj}\Omega_j^0 - K_{m-1}\left(\varphi_m - \varphi_{m-1}\right)\right], \; j = 1, \ldots, m && \text{(II.35)}
\end{aligned}
$$

where we recall that C_{ij} are the components of the matrix $\mathbf{C}$ from Eq. (II.26), and φ_i is given in Appendix A.B.

To simulate the whole process of initiation and propagation of a hydraulic fracture under subcritical conditions, the algorithm consists of two phases. At the initiation phase, for a given defect with fixed length and initial condition (II.24), we increase the time by $\Delta\tau_i$ at every step and solve the corresponding nonlinear system (II.29) using fixed-point iteration. In this approach, at iteration k, the increment of the opening is found from the solution of the following linear system,

$$
\mathbf{\Xi}\left(\triangle\mathbf{\Omega}^k\right)\triangle\mathbf{\Omega}^{k+1} = \mathbf{\Gamma}\left(\triangle\mathbf{\Omega}^k\right) \tag{II.36}
$$

Recall that, via the construction of the discretized Poiseuille law (II.27), the solution of Eq. (II.36) satisfies the inlet flux and tip boundary conditions (II.23) and (II.22).

Once the initiation criterion is satisfied (i.e., $K_{\mathrm{I}} = K_{\mathrm{I}}^{*} = K_{\mathrm{IC}}/10$), the algorithm switches to the propagation phase, in which we use a length control algorithm to solve the coupled problem. Based on the algorithm, a fixed length increment (chosen to be small enough that the solution is independent of its value) is applied in every step. Again, the increment of crack width can be obtained by the iterative scheme (II.36). However, the time increment $\Delta\tau$ remains unknown. Hence, the algorithm sets a value of $\Delta\tau$ in an outer iteration loop, uses that value in an inner loop to iteratively solve lubrication equation (II.36), and then adjusts the value of $\Delta\tau$ in the outer loop to satisfy the still-unused tip asymptotic condition (II.21). This outer-loop algorithm is different for the two models (subcritical growth model when $K_{\mathrm{I}} < K_{\mathrm{Ic}}$ and conventional model when $K_{\mathrm{I}} = K_{\mathrm{Ic}}$). For subcritical growth, upon the discretization $\frac{\mathrm{d}\gamma}{\mathrm{d}\tau} \approx \frac{\Delta\gamma}{\Delta\tau}$, the time step appears directly in the tip asymptotic condition and so, at current time step N, approximating $\frac{\Delta\gamma}{\Delta\tau^{N}} = \frac{\Delta\xi}{\Delta\tau^{N}} \approx \frac{1}{2}\left(v^{N-1} + v^{N}\right)$ and rearranging Eq. (II.21), the outer loop is aimed at finding $\Delta\tau$ that provides a zero to the function

$$f\left(\triangle\tau^{N}\right) = \triangle\tau^{N} - \frac{2\triangle\xi}{\alpha\left[\left(\kappa^{N-1}\right)^{n} + \left(\kappa\left(\triangle\tau^{N}\right)\right)^{n}\right]} \tag{II.37}$$

where $\kappa = K_{\mathrm{I}}/K_{\mathrm{IC}}$, and $\kappa\left(\triangle\tau^{N}\right)$ denotes the value of κ computed as a function of the time increment $\triangle\tau^{N}$ at step N. In this case, K_{I} is computed by Eq. (A.21) or (A.22) given in Appendix A.C.

For the case of $K_{\mathrm{I}} = K_{\mathrm{Ic}}$, the time increment $\Delta\tau$ does not appear explicitly in the tip asymptotic condition (II.21). Therefore, in this case, the outer loop involves checking whether this condition is satisfied, and if not, adjusting $\Delta\tau$ in accordance with global volume balance (II.25), which in discretized form is

$$\triangle\tau^{K} = \triangle\Pi_{w}^{K-1} + 2\Delta\xi\sum_{j=1}^{m}\left(\pi\xi_{j}\right)^{d-1}\Delta\Omega_{j}^{K-1} \tag{II.38}$$

recalling that K is the iteration counter for the outer loop. In Eq. (II.38), the values of $\Delta\Omega_{j}^{K-1}$ are adjusted so that $\Delta\Omega_{m}^{K-1}$ satisfies the tip asymptotic condition (II.21). In essence, then, adjusting $\Delta\tau$ adjusts the volume of the fracture until the propagation condition is satisfied.

The components of the algorithm are briefly summarized as follows:

Given initial condition at $\tau = 0$ $(\mathbf{\Omega}^0,\ \gamma^0,\ \kappa^0)$

Initiation loop $N = 1 : N_{max}$

Advance time step: $\tau^N \leftarrow \tau^{N-1} + \triangle\tau_i$

Inner loop $(k++)$ to solve (II.36) for $\triangle\mathbf{\Omega}^N$

Update $\mathbf{\Omega}^N,\ \kappa^N$

Check for initiation criterion: $\kappa \geq 0.1$, set $N_{ini} = N$, break

end initiation loop

Propagation loop $N = (N_{ini} + 1) : N_f$

Advance fracture front: $\gamma^N \leftarrow \gamma^{N-1} + \triangle\xi$

Outer loop $(K++)$ to find solution for time step $\triangle\tau^N$ based on the

propagation model (subcritical if $\kappa < 1$, or conventional when $\kappa = 1$)

Inner loop $(k++)$ to solve (II.36) for $\triangle\mathbf{\Omega}^K$

Update $\mathbf{\Omega}^N,\ \kappa^N,\ \tau^N$

end propagation loop

Details of the outer and inner iteration loops are presented in Appendix A.C.

G. NUMERICAL RESULTS

1. Validation

In our plane strain model, we discretize the wellbore wall using DD elements in a two-dimensional homogeneous elastic material such that the circular boundary is included in the integration contour in the elasticity equations (II.5). An alternative treatment of the plane strain problem of a circular wellbore with a symmetric bi-wing crack has been employed, for example, by Bunger et al. (2010); Lakirouhani et al. (2016); Lecampion (2012a,b), where the elastic integral equation for the crack involves the integral kernel corresponding to an edge dislocation interacting with a circular hole (Dundurs and Mura, 1964). The DD represen-

tation of the wellbore with a crack adopted in the present paper has been previously used by Zhang et al. (2011) for HF modeling, and it has its own advantages, such as allowing for modeling the deformation of the wellbore wall, and potentially extending the model to consider multiple fractures and fracture curving by introducing minor changes to the DD model. Validation of the DD representation of the wellbore against available reference solutions is provided in Appendix A.D.

Next, we verify our subcritical growth model by comparing the results with available analytical solutions for hydraulic fractures under toughness-dominated ($\mathcal{M} \ll 1$, Eq. II.15) and viscosity-dominated ($\mathcal{M} \geq 1$) conditions (Adachi, 2001; Savitski and Detournay, 2002). Although these analytical solutions do not consider wellbore compressibility, near-wellbore stresses, or subcritical growth, we know that the wellbore compressibility and near-wellbore stress effect will vanish as the fracture grows relative to both the wellbore radius and compressibility lengthscale. Hence, they comprise the large time solution provided the effect of subcritical growth vanishes. To this point, if the subcritical index, n, tends to infinity, then the term that involves crack tip velocity in Eq. (II.3), $(V/A)^{1/n}$, tends to 1. Consequently, the subcritical asymptote, Eq. (II.3), reduces to the classical k asymptote, and our model recovers the same results as given by the conventional model. In this spirit, we show the evolution of fracture length for both plane strain and axisymmetric hydraulic fractures, with a value of n that is large enough ($n = 1000$), in Fig. II.4. In the case of a hydraulic fracture induced by a fluid with very small viscosity, i.e., $\mathcal{M} = 0.001$, the fracture propagation is governed by the toughness-dominated (k) regime. Conversely, solutions for viscosity-dominated (m) regime can be obtained by imposing a large viscosity, i.e., $\mathcal{M} = 10$. As can be seen in Fig. II.4, our results are validated as they converge to k and m asymptotic solutions for long term propagation under the plane strain (Adachi, 2001) and axisymmetric conditions (Savitski and Detournay, 2002).

A study on the convergence of the numerical results with the mesh size of the DD elements along the crack, $\triangle\xi$, is then performed by conducting a series of simulations for an HF problem (take plane strain for example) using different element sizes $\triangle\xi$ along the initial crack of an intermediate length. Parameters are taken as typical for an HF treatment: $n = 40$, $A = 2175$ $^{m}/_{s}$, $E = 27.3$ GPa, $\nu = 0.3$, $K_{\mathrm{IC}} = 2$ MPa $\cdot$ m$^{1/2}$, $U = 5 \times 10^{-11}$ $^{\mathrm{m}^2}/_{\mathrm{Pa}}$,

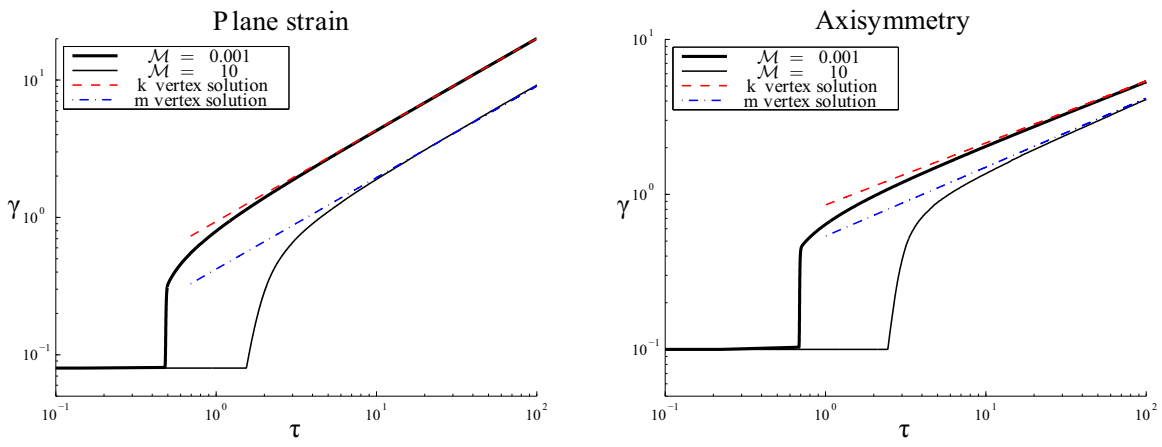

Figure II.4: Evolution of crack length for a plane strain (left) and radially symmetric (right) fracture. The confining stresses are set to be zero. Analytical solutions for toughness-(k), and viscosity-(m) dominated regimes are obtained from Adachi (2001) and Savitski and Detournay (2002).

$\mu = 0.001$ Pa $\cdot$ s, $Q_0 = 0.00512$ $^{m^2}/_{\text{s}}$, $\sigma_H = \sigma_h = 0$ MPa, and $a = 0.1$ m. The length of the initial crack is chosen to be the same as the wellbore radius ($l_0 = 0.1$ m). Therefore, the values of the dimensionless parameters are computed as follows: $\mathcal{M} = 1$, $\mathcal{A} = \gamma_0 = 0.08$, $\Phi_h = \Phi_D = 0$, $\alpha = 100$. Since $\triangle\xi = \gamma_0/m_0$, where m_0 is the number of elements along the initial crack, the numerical test is carried out by changing the number of elements along the starter crack: $m_0 = 10$ (very coarse mesh), $m_0 = 20$ (coarse mesh), $m_0 = 40$ (intermediate mesh), $m_0 = 80$ (fine mesh), and $m_0 = 160$ (very fine mesh). For each case, the element size along the wellbore and the crack is the same.

The evolution of the crack length and the wellbore pressure is shown in Fig. II.5 (a, b). Convergence in the solution is observed as the mesh size gets finer, and the difference between the solutions with mesh refinement finally becomes practically negligible when refining the mesh to 160 elements in the initial crack. Here the relative differences for crack length γ and pressure Π_w with respect to the reference solution (the solution obtained with the finest mesh size, $\triangle\xi = \gamma_0/160$) are defined as

$$D_r^{\gamma}(\tau) = \frac{|\,\gamma(\tau) - \gamma^{\text{ref}}(\tau)\,|}{\gamma^{\text{ref}}(\tau)}$$

$$D_r^{\Pi}(\tau) = \frac{|\,\Pi_w(\tau) - \Pi_w^{\text{ref}}(\tau)\,|}{\Pi_w^{\text{ref}}(\tau)}$$

where the superscript "ref" denotes the reference solution. Fig. II.5 (c, d) shows the evolution of the relative differences with time. It can be seen that the solution obtained using 80 initial elements has the relative difference less than 2% for the wellbore pressure and within 10% for the crack length, except for the time interval close to crack initiation. Past the fracture initiation, the relative difference for the crack length, for 80 initial elements is within a few percent. For this test, consistency in the numerical solution is observed once the element size is reduced to $\triangle\xi = \gamma_0/80$, indicating that the solution becomes sufficiently independent of the crack length increment (equal to the element size $\triangle\xi$ along the crack). Similarly, the values of $\triangle\xi$ for other initial crack lengths can be determined by conducting the same numerical experiment.

Another test has been carried out for the case with a decreased viscosity $\mathcal{M} = 0.001$ (while every other dimensionless parameter remains the same). The results obtained with different initial numbers of elements in starter crack ($m_0 = 10$, 20, 40, and 80) are shown in Fig. II.6. Taking the finest mesh size $\triangle\xi = \gamma_0/80$ (or equivalently, $m_0 = 80$) as the reference solution, the relative difference is computed for $m_0 = 10$, 20, and 40. This time, more rapid convergence is observed; consistent results are obtained as soon as the mesh size is refined to $\triangle\xi = \gamma_0/20$. These results indicate that the dimensionless viscosity $\mathcal{M}$ has a strong influence on the rate of convergence in the numerical solution when refining the mesh size. A bigger value of $\mathcal{M}$ requires a finer mesh size in order to get accurate results. This characteristic has been observed with other HF simulators (Lecampion et al., 2013) and can be explained by the nature of the tip asymptotic solution. In the numerical algorithm, we use the subcritical toughness k asymptote, and thus under the viscosity-dominated (m) regime (large $\mathcal{M}$) the accuracy of the subcritical toughness k asymptote is limited to a relatively small region near the tip.

Another notable observation is that the time of initiation also varies in different cases due to the change in mesh size. It is shown in Figs. II.5 and II.6 that a coarser mesh size

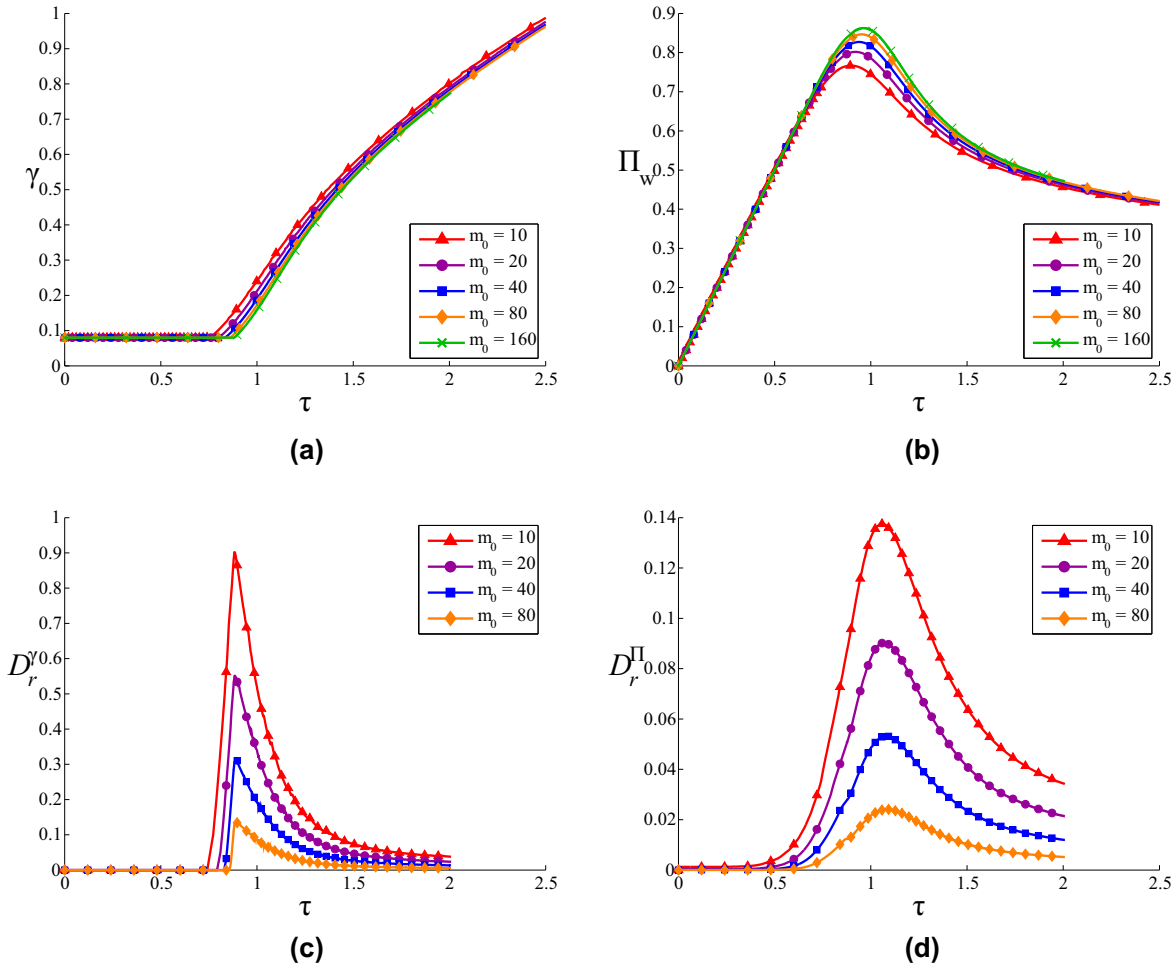

Figure II.5: Mesh convergence study for $\mathcal{M} = 1$. Evolution of crack length (a) and wellbore pressure (b) for all cases, together with relative difference (c, d) with respect to results from $m_0 = 160$.

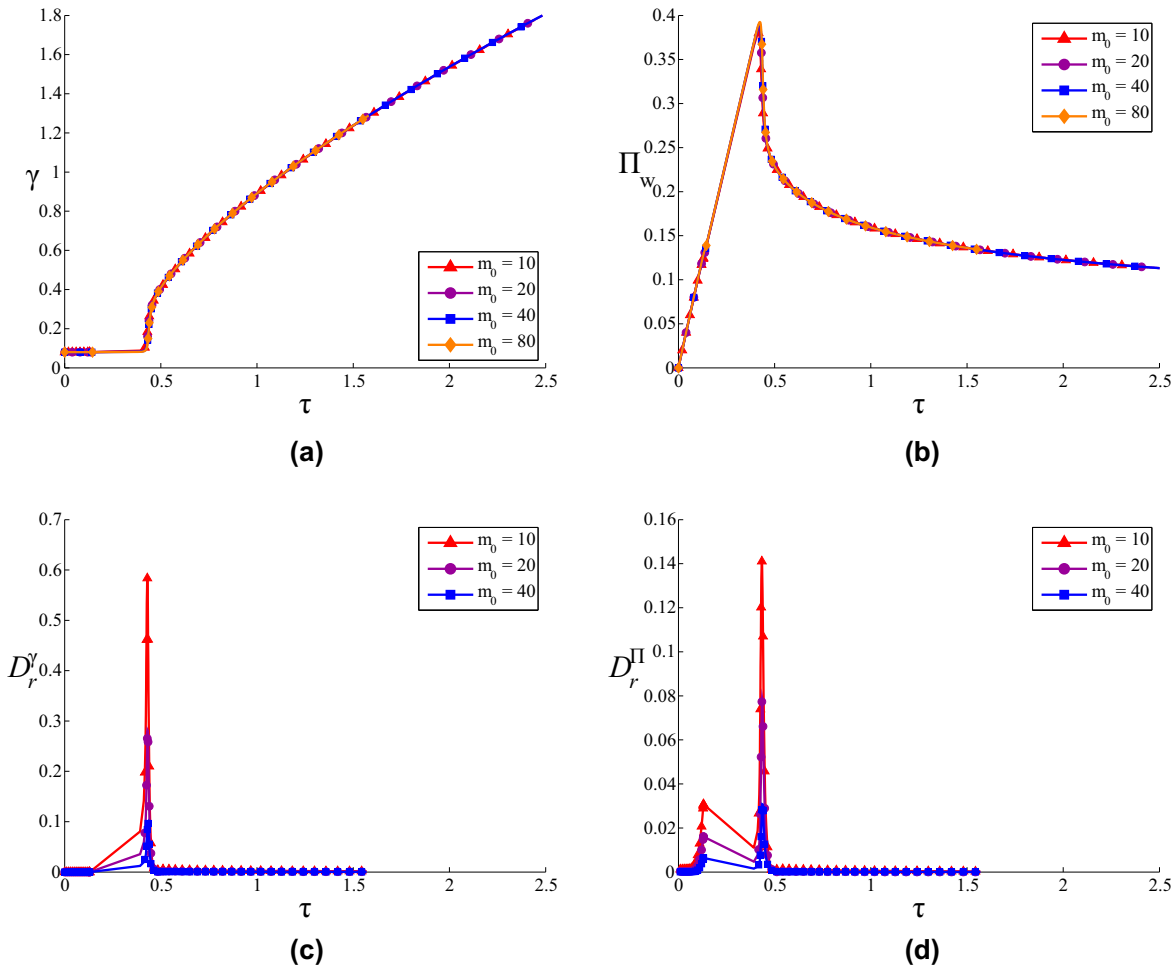

Figure II.6: Mesh convergence study for $\mathcal{M} = 0.001$. Evolution of crack length (a) and wellbore pressure (b) for all cases, together with relative difference (c, d) with respect to results from $m_0 = 80$.

will lead to an earlier initiation. As a result, when comparing solutions from various mesh sizes, the value of the relative difference is somewhat magnified. For example, during the time period close to fracture initiation, sudden changes in both crack length and wellbore pressure evolution have already taken place in a case with a coarser mesh size, whereas the initiation point has yet to be reached for the case using a finer mesh size. The relative difference, D_r, increases significantly at this moment (see relative difference at $\tau \approx 0.9$ in Fig. II.5 (c,d) and $\tau \approx 0.45$ in Fig. II.6 (c,d)).

2. Solution for subcritical fracture initiation and propagation

We first show a comparison between results from plane strain and axisymmetric fractures subjected to the same condition ($\alpha = 2000,\ \mathcal{A} = 0.08,\ \gamma_0 = \mathcal{A}/4,\ \mathcal{M} = 0.001$) in Fig. II.7. The LEFM curves are obtained from numerical simulations that impose the critical condition $K_{\mathrm{I}} = K_{\mathrm{IC}}$, which is equivalent to $n \to \infty$ in the subcritical growth model. The comparison between the two geometries shows some differences in the numerical values of the solutions, but there is a qualitative similarity between the two geometries in terms of the evolution of crack length and the wellbore pressure. To illustrate the overall behavior of the system without unnecessary repetition, our further discussion will be focused on the initiation and subsequent growth of plane strain hydraulic fractures.

Besides establishing the qualitative similarity between plane strain and radial cases, Fig. II.7 shows the overall variation of the solution with the subcritical index n. As expected, for large n, in this case $n = 200$, the solution tends towards the LEFM solution. However, for smaller values of n, with the practical range going down to $n = 10$, the HF initiates at a lower pressure. As a result, the peak (maximum) net wellbore pressure is reduced by a factor of 3 from the LEFM solution. This lower initiation pressure leads to an earlier initiation time because the pressure, prior to initiation, increases as fluid is injected into the compressible wellbore system. We also observe that the HF length for the LEFM (and $n = 200$) cases jumps very rapidly upon initiation, evidencing an instability associated with sudden release of compressed fluid volume in the injection system (Lhomme et al., 2005). For the $n = 10$ case the early time growth is more gradual.

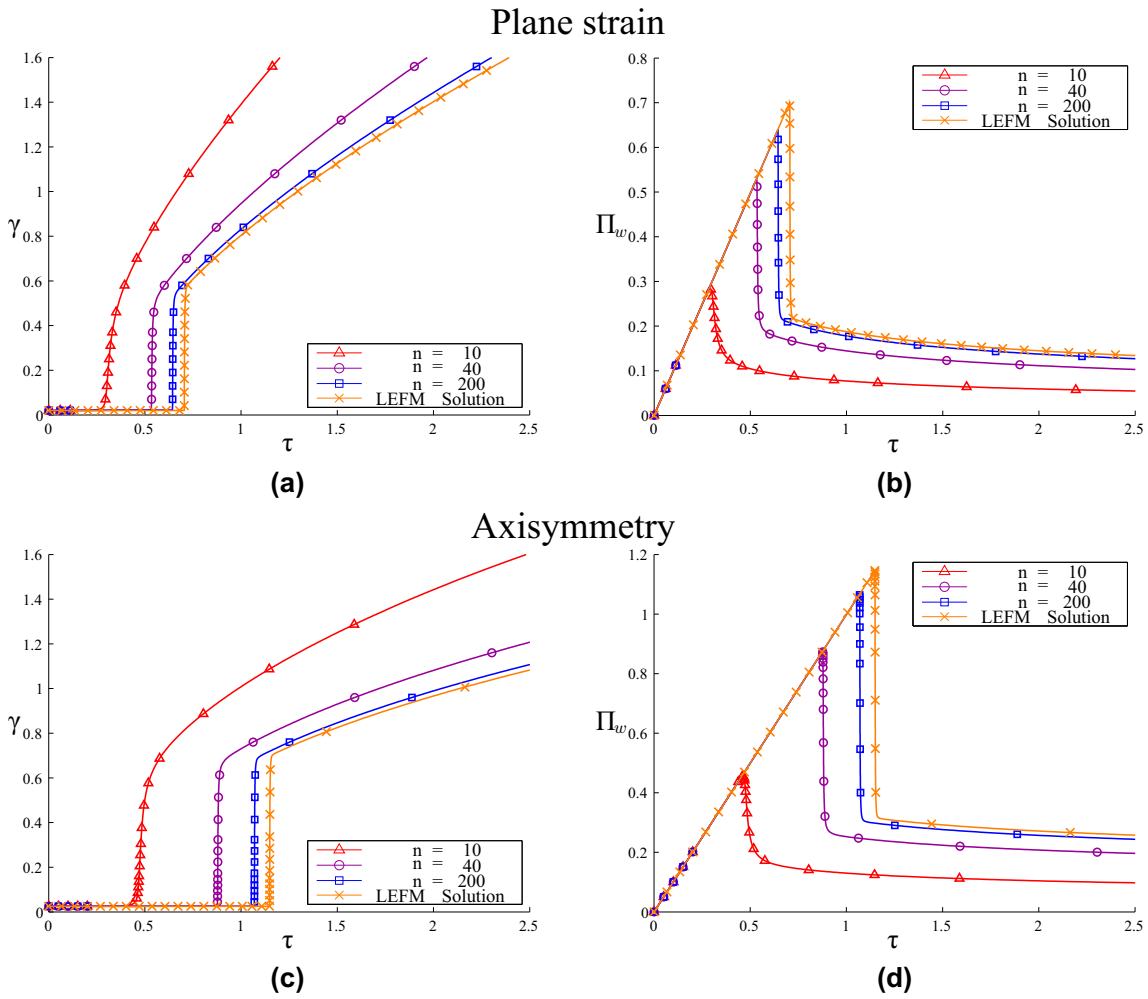

Figure II.7: Evolution of crack length and wellbore pressure for a plane strain (a, b) and an axisymmetric (c, d) fracture under the subcritical conditions with different values of n ($\alpha = 2000,\ \mathcal{A} = 0.08,\ \gamma_0 = \mathcal{A}/4,\ \mathcal{M} = 0.001$). Results are compared to the classical LEFM solutions.

Fig. II.7 shows that the impact of subcritical growth is substantial, especially for smaller values of n. The impact of subcritical growth, and its dependency on n, is also influenced by the initial crack length γ_0 and the dimensionless viscosity $\mathcal{M}$. To illustrate, Figs. II.8 and II.9 present results again with different values of the subcritical index, n, but this time for an initially shorter crack ($\gamma_0 = \mathcal{A}/4$, as in Fig. II.7), and a longer crack ($\gamma_0 = 4\mathcal{A}$). Physically, these correspond to the initial crack, which can be thought of as a material flaw, that is one-fourth of the wellbore radius compared with one that is four times the wellbore radius. Alternately, because $\gamma_0 = 0.02$ and $\gamma_0 = 0.32$ for these two cases, they correspond to the initial crack being 2% and 32% of the characteristic length associated with the injection system compressibility, respectively. (Recall in this scaling, compressibility effects vanish as γ_0 greatly exceeds 1.) For both the long and short initial crack length, we also compare two values of the dimensionless viscosity ($\mathcal{M} = 0.001$ and 0.1). To isolate the role of these three parameters, for now, no confinement is applied in our simulation ($\Phi_H = \Phi_h = 0$ in Eq. II.13). However, the impact of confinement will be explored later in this paper. Once again, notable changes in evolution of length and wellbore pressure are observed due to the influence of subcritical crack growth.

The effect of subcritical growth on the wellbore peak presure is further demonstrated in Fig. II.10 for both plane strain and axisymmetric fractures. As in Figs. II.8 and II.9, a total of four cases are simulated in each geometry. These correspond to the four combinations that represent high/low viscosity and long/short initial crack. The influence of subcritical growth is shown to be very strong, again, leading to reductions of the peak pressure by a factor of two to three in cases with short initial crack and low viscosity.

Hence, the importance of subcritical growth is demonstrated, on the one hand. However, the impact of subcritical growth on both crack length and the wellbore pressure is diminished for larger dimensionless viscosity $\mathcal{M}$ and for larger initial crack length γ_0.

Considering first the role of the flaw size, if we take the physical flaw size in most rocks to be $O(0.01)$ m, that is to say, larger than 1 mm and smaller than 100 mm, the major variation in γ_0 is expected to be attributable to the compressibility of the injection system owing to its impact on the characteristic length ℓ_* (Eq. II.13). For example, taking water with compressibility $c_f = O(10^{-4})$ MPa^{-1} and rock with $E' = O(10^4)$ MPa, the characteristic

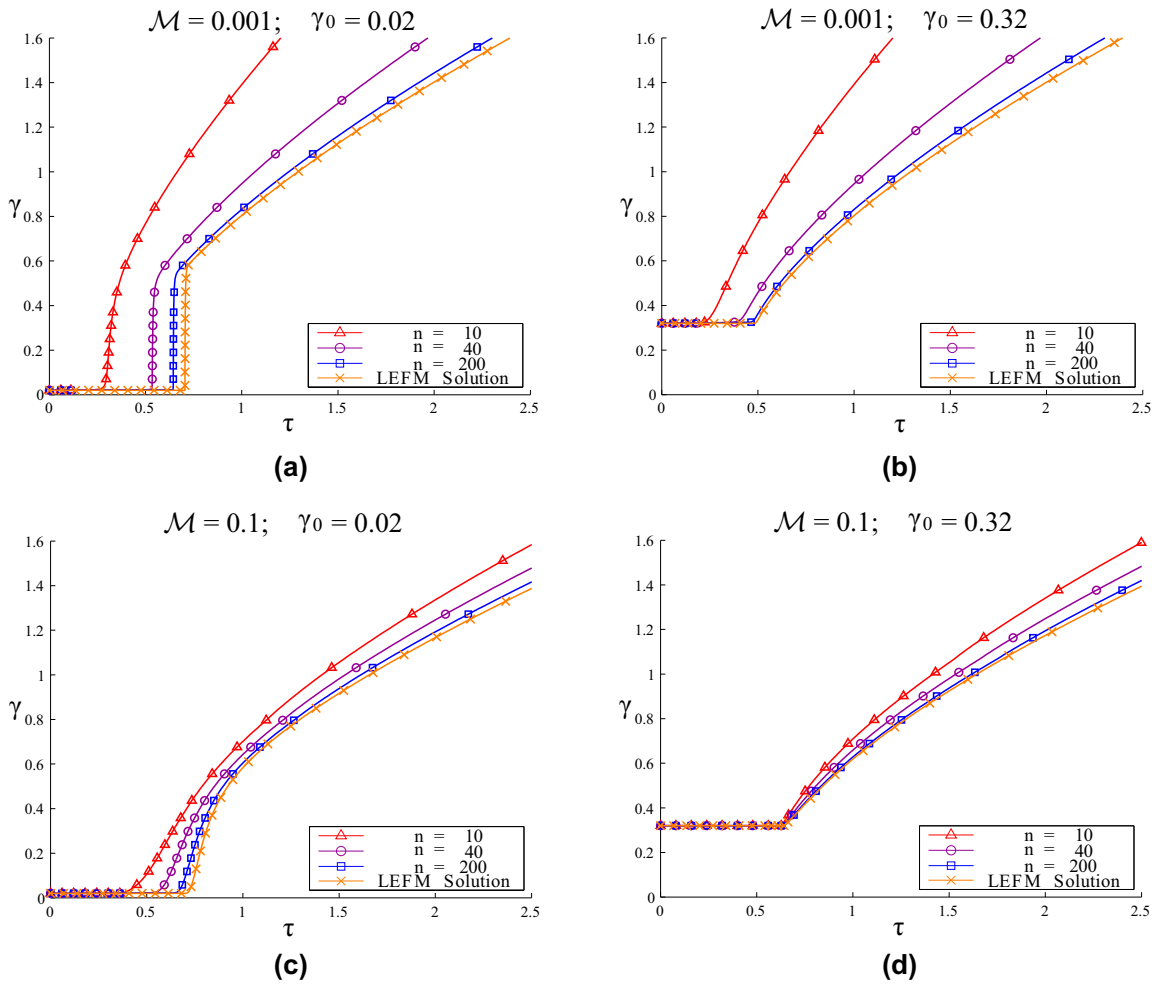

Figure II.8: Evolution of crack length for a plane strain fracture with (a) $\alpha = 2000,\ \mathcal{A} = 0.08,\ \gamma_0 = \frac{1}{4}\mathcal{A},\ \mathcal{M} = 0.001$; (b) $\alpha = 2000,\ \mathcal{A} = 0.08,\ \gamma_0 = 4\mathcal{A},\ \mathcal{M} = 0.001$; (c) $\alpha = 2000,\ \mathcal{A} = 0.08,\ \gamma_0 = \frac{1}{4}\mathcal{A},\ \mathcal{M} = 0.1$; (d) $\alpha = 2000,\ \mathcal{A} = 0.08,\ \gamma_0 = 4\mathcal{A},\ \mathcal{M} = 0.1$. Results are compared to the classical LEFM solutions.

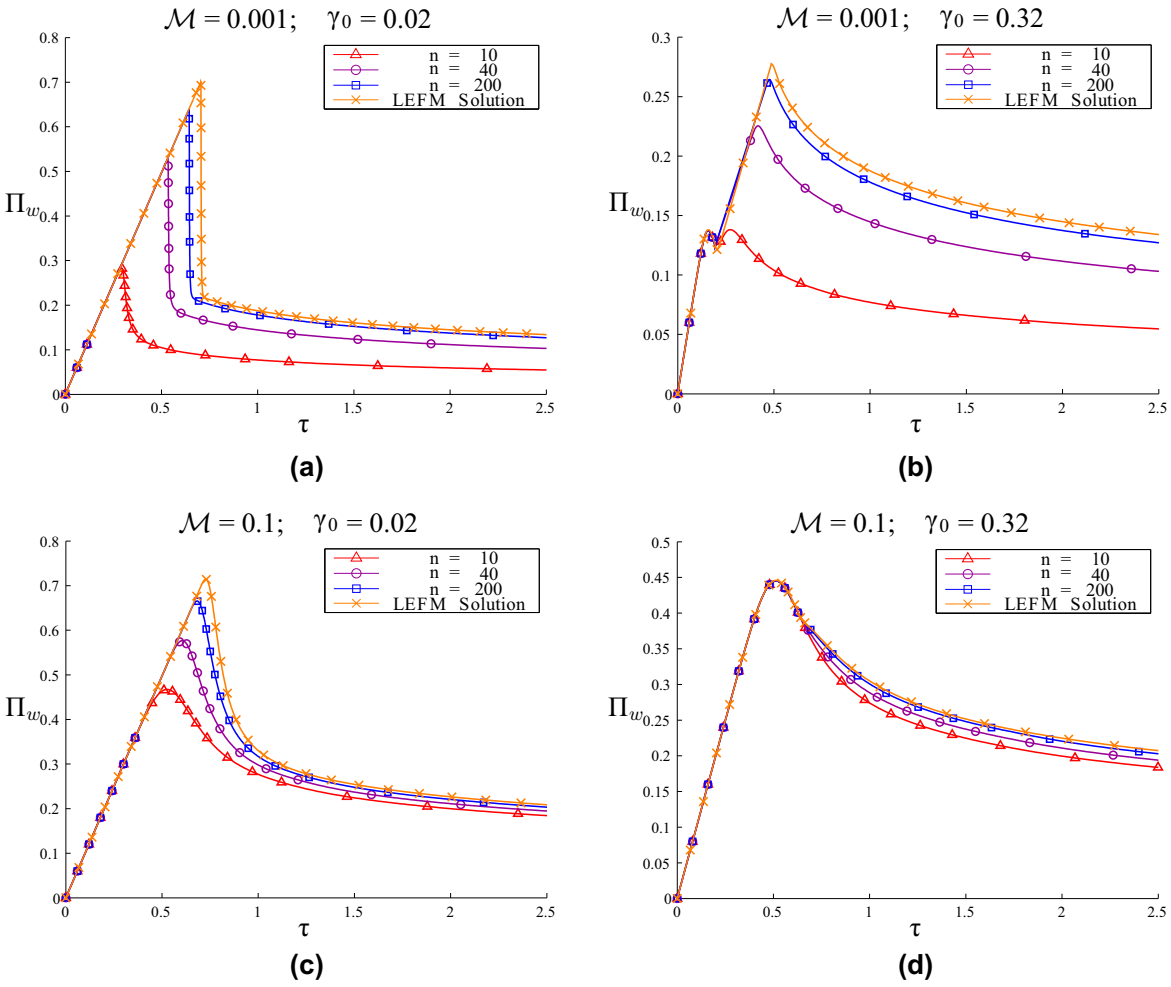

Figure II.9: Evolution of wellbore pressure for a plane strain fracture with (a) $\alpha = 2000,\ \mathcal{A} = 0.08,\ \gamma_0 = \frac{1}{4}\mathcal{A},\ \mathcal{M} = 0.001$; (b) $\alpha = 2000,\ \mathcal{A} = 0.08,\ \gamma_0 = 4\mathcal{A},\ \mathcal{M} = 0.001$; (c) $\alpha = 2000,\ \mathcal{A} = 0.08,\ \gamma_0 = \frac{1}{4}\mathcal{A},\ \mathcal{M} = 0.1$; (d) $\alpha = 2000,\ \mathcal{A} = 0.08,\ \gamma_0 = 4\mathcal{A},\ \mathcal{M} = 0.1$. Results are compared to the classical LEFM solutions.

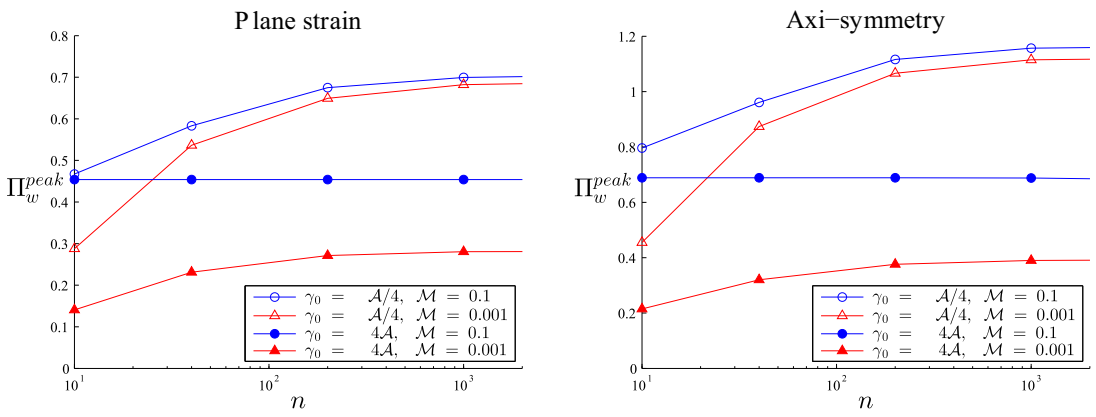

Figure II.10: Correlation between peak pressure, Π_w^{peak}, and subcritical index, n, for a plane strain (left) and an axisymmetric (right) fracture with various initial crack lengths ($\gamma_0 = \frac{1}{4}\mathcal{A}/4\mathcal{A}$), and fluid viscosities ($\mathcal{M} = 0.1/0.001$).

length $\ell_* = O(V_0^{1/3})$ (for axisymmetric cases), recalling that V_0 is the volume of the injection system. In the laboratory, $V_0 = O(10^{-3})$ m^3 and so $\ell_* = O(0.1)$ m. In constrast, in the field, $V_0 = O(10)$ m^3, and so $\ell_* = O(1)$ m. Hence, $\gamma_0 = O(0.1)$ is expected to correspond to laboratory cases, indicating a tendency for lesser importance of subcritical growth at laboratory scale compared to field scale, where we expect $\gamma_0 = O(0.01)$.

Now we turn the attention to the role of the viscosity. In the case $\gamma_0 = 0.32$ and $\mathcal{M} = 0.1$ (case d), the effect of subcritical growth is relatively insignificant, in stark contrast to the factor of two to three reduction in peak pressure obtained for $n = 10$, $\gamma_0 = 0.02$, and $\mathcal{M} = 0.001$ (case a). Furthermore, as the dimensionless viscosity $\mathcal{M}$ gets large enough, this effect becomes negligible even for small initial cracks. Fig. II.11 gives both the change of crack length and wellbore pressure with time for a short initial crack $\gamma_0 = 0.02$ injected by a fluid with $\mathcal{M} = 1$. As shown in both crack length and wellbore pressure evolution, the difference is almost indistinguishable between the solutions from various subcritical index values ($n = 10$, 40, 200) and the classical HF solution. Based on these results, it is implied that, in this particular situation, the energy dissipation associated with viscous flow along the crack is dominating the HF process.

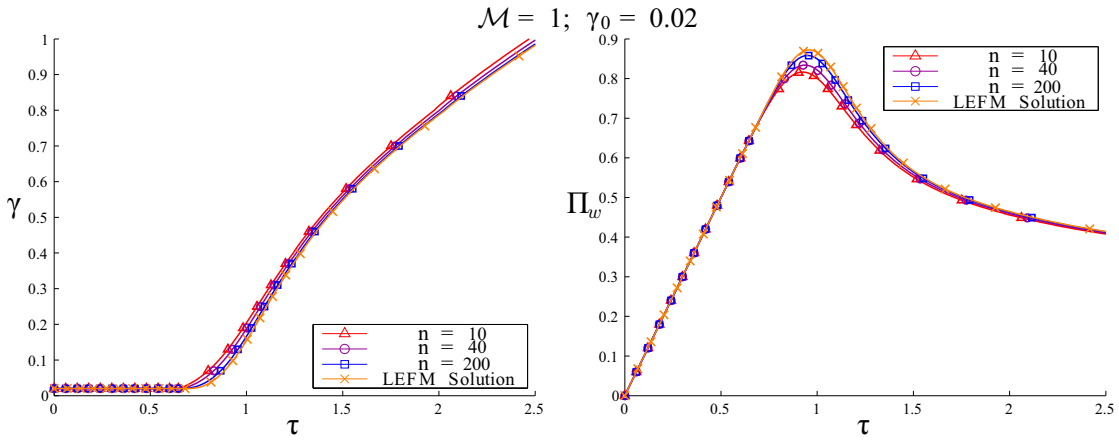

Figure II.11: Evolution of crack length (left) and wellbore pressure (right) for a plane strain fracture with $\gamma_0 = 0.02,\ \mathcal{M} = 1$.

Additionally, it is worth noting that in results from the small viscosity and large initial cracks (case b), the evolutions of wellbore pressure all experience a drop in the early stage (around $\tau = 0.13$). This corresponds to the time when the fluid firstly flows into the initial defect. In fact, before this point, the slope of the pressure curve is equal to 1, which implies that all the injected fluid has been accomodated by the compressibility of the injection system and there is no fluid influx to the initial crack during this period of time (set $\frac{\mathrm{d}\Pi_w}{\mathrm{d}\tau} = 1$ in Eq. II.23, then the fluid influx $\bar{\Psi}$ goes to zero). Once the fluid enters into the crack, an almost uniform pressure (since $\mathcal{M} = 0.001$) is generated and the whole crack is opened instantly. Consequently, a change of compliance is expected for the case of a long initial crack, associated with a release of certain amount of fluid volume from the compressible system into the crack, which causes the drop in wellbore pressure.

Further insight is gained by examining the evolution of the stress intensity factor, K_{I}. It is reasonable to expect that K_{I} will increase with time until $K_{\mathrm{I}} = K_{\mathrm{IC}}$, after which propagation continues according to LEFM. However, this is not what is observed in these simulations. An example of evolution of stress intensity factors for the case of a short initial crack ($\gamma_0 = 0.02$) is shown in Fig. II.12. Here we see that the stress intensity factor

converges to an apparant steady-state value after a transient period around the time of fracture initiation. This apparant steady-state value is strongly impacted by the subcritical index n, and the fluid viscosity also has an effect on it. Strikingly, these simulations predict that, for a rock with $n = 10$, a hydraulic fracture will propagate with a nearly steady-state value of the stress intensity factor that is roughly half of the fracture toughness of the rock.

To model the dependence of the stress intensity factor on the value of n, we reduce our problem to the propagation of a Griffith's crack (i.e., line crack with vanishing wellbore and compressibility effect) injected by an inviscid fluid. Accordingly, the governing equations for this problem are equivalent to the subcritical growth of a line crack under uniform fluid pressure, which are given explicitly by

$$\begin{aligned} w &= 4\tfrac{p}{E'}\sqrt{l^2 - x^2} \\ K_{\mathrm{I}} &= p\sqrt{\pi l} \\ Q_0 t &= 2\int_0^l w dx \end{aligned} \tag{II.39}$$

together with the subcritical crack growth law (II.1). By substitution of Eq. (II.39) into Eq. (II.1) and solving the ordinary differential equation, the dimensionless stress intensity factor, κ, can be expressed as

$$\kappa = \frac{K_{\mathrm{I}}}{K_{\mathrm{IC}}} = \left(16\sqrt{2\pi}\right)^{\frac{-1}{3n+2}} \left(\frac{2n+2}{3n+2}\right)^{\frac{3}{3n+2}} \left(\frac{Q_0^4 E'^3}{A^4 {K_{\mathrm{IC}}}^4 U}\right)^{\frac{3}{12n+8}} \tau^{\frac{-1}{3n+2}} \tag{II.40}$$

In Eq. (II.40), the term $\tau^{\frac{-1}{3n+2}}$ gets close to 1 as n goes to infinity. For a practical value of n ($n = O(10)$), it is implied that κ stays nearly constant for long-term propagation of a hydraulic fracture under subcritical conditions. The evolution of κ for the simplified problem, obtained from Eq. (II.40), are also shown in Fig. II.12 (dashed lines). As can be seen in the figure, the κ curves from our simulations quickly converge to the dashed lines for cases with large n and small viscosities, and the prediction given by Eq. (II.40) provides a good estimate of the value of K_{I} associated with propagation. However, as previously discussed, for $\mathcal{M} = 1$ the pressure associated with initiation and propagation is nearly independent of subcritical index n, indicating that the main mechanical factor controlling the fluid pressure required for crack growth is the dissipation of viscous energy, not rock fracturing (which would be dependent on subcritical index n).

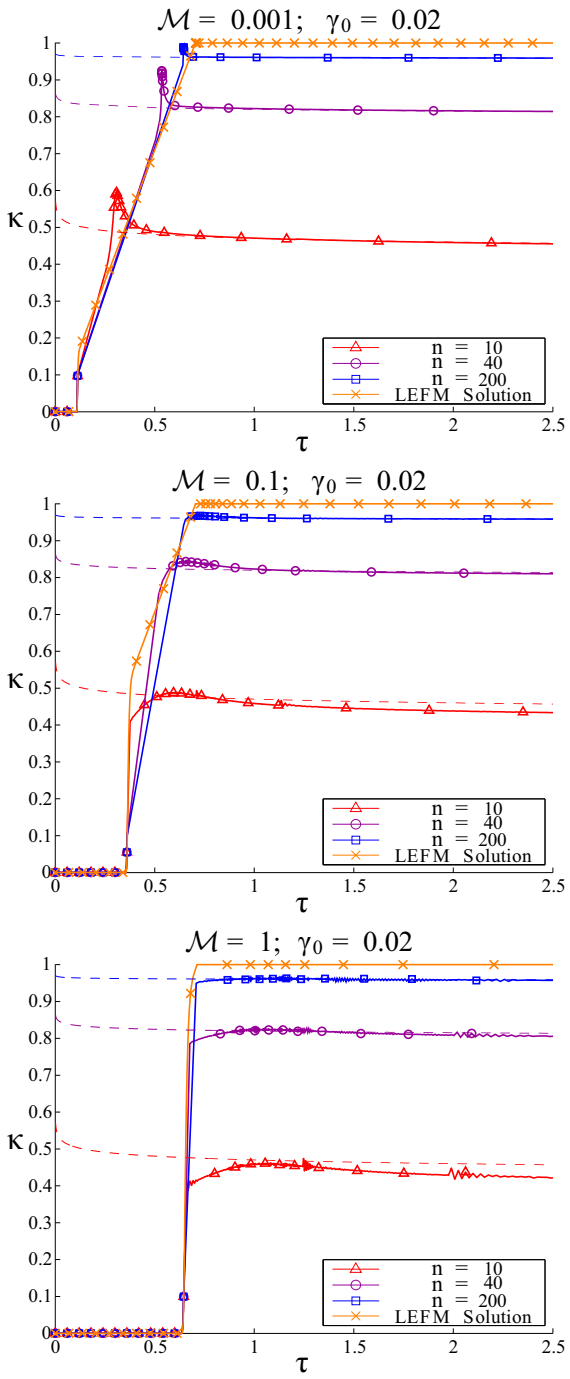

Figure II.12: Stress intensity factor for a plane strain fracture with initial length $\gamma_0 = 0.02$ using the injection fluid with $\mathcal{M} = 0.001$ (top), $\mathcal{M} = 0.1$ (middle), and $\mathcal{M} = 1$ (bottom). The dashed lines are obtained from Eq. (II.40).

Further expanding the exploration of the various parameters on the behavior of the system, the effect of wellbore radius is shown in Fig. II.13 for the case of an intermediate value of subcritical index $n = 40$. Notable differences can be observed in the evolution of wellbore pressures when comparing cases with different initial crack lengths and fluid viscosities. In particular, the results indicate that a larger wellbore radius can lead to an earlier initiation and reduced peak pressure. This well known size effect has also been shown by Lecampion (2012b) using the mixed strength and energy fracture initiation criteria.

Next, we examine the influence of the in-situ stresses. Comparisons are carried out for the four combinations of high/low viscosity, and long/short initial crack with different deviatoric stresses. The particular cases considered are the following:

I. $\sigma_H = \sigma_h = 30$ MPa; corresponding to the dimensionless in-situ stresses $\Phi_H = \Phi_h = 5.2$ and $\Phi_D = 0$;

II. $\sigma_H = 35.8$ MPa; $\sigma_h = 30$ MPa; corresponding to dimensionless in-situ stresses $\Phi_H = 6.2$, $\Phi_h = 5.2$, and $\Phi_D = 1$.

The evolution of wellbore pressure for each case is given in Fig. II.14. The results suggest a reduction in peak wellbore pressure by increasing the deviatoric stress, Φ_D. This correlation is also expected from the classical theory by Hubbert and Willis (1957), which is known as a strength criterion for hydraulic fracture breakdown derived from the Kirsch stress concentration at the borehole. We also observe that when the initial crack length, fluid viscosity, and deviatoric stress are large, no obvious sign of "peak" in wellbore pressure can be found. Instead, it increases smoothly from the beginning of injection and ultimately converges to a constant value (see the case of $\gamma_0 = 0.32$, $\mathcal{M} = 0.1$, $\Phi_D = 1$).

H. CONCLUSIONS

We have described a numerical model for predicting hydraulic fracture initiation and propagation from a circular wellbore for plane strain and axisymmetric geometries. The fracture behavior under the subcritical propagation condition was studied using this model and re-

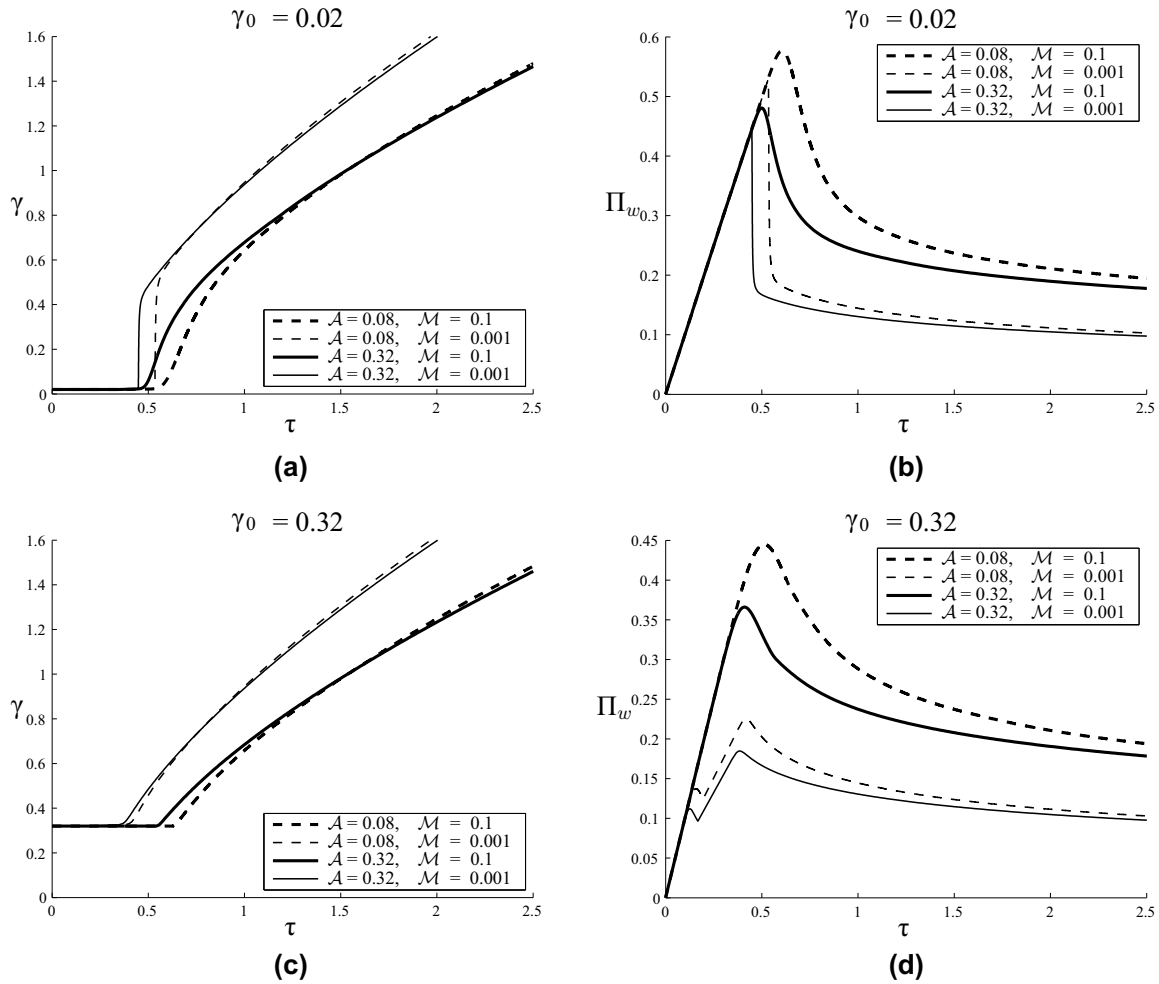

Figure II.13: Evolution of crack length and wellbore pressure of hydraulic fractures under subcritical conditions ($n = 40$, $\alpha = 2000$), using various wellbore radii $\mathcal{A} = 0.08$ or $\mathcal{A} = 0.32$, and fluid viscosities $\mathcal{M} = 0.1$ or $\mathcal{M} = 0.001$, for two initial crack lengths $\gamma_0 = 0.02$ (a, b) and $\gamma_0 = 0.32$ (c, d).

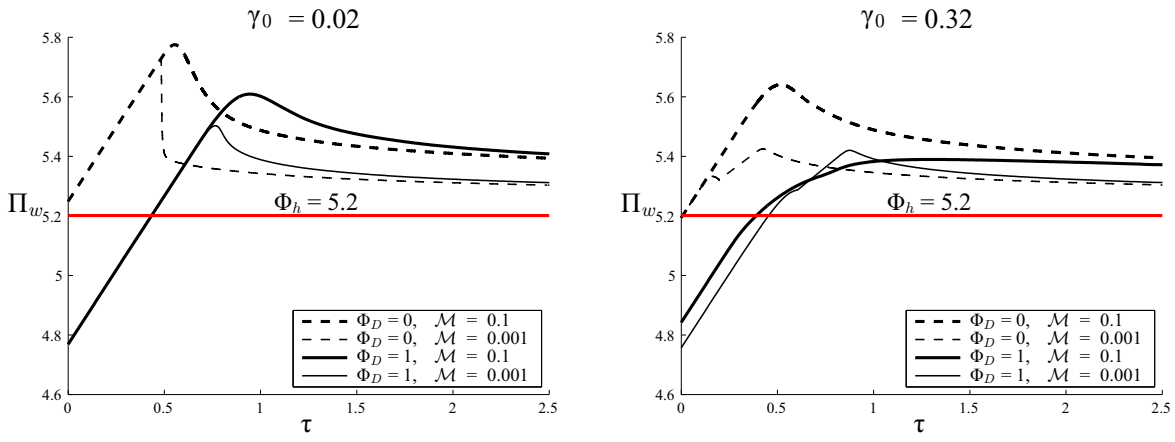

Figure II.14: Wellbore pressure for a short (left) and a long (right) initial crack with various deviatoric stresses and viscosities of injected fluid ($n = 40,\ \alpha = 2000,\ \gamma_0 = 0.02/0.32,\ \mathcal{M} = 0.1/0.001,\ \Phi_D = 1/0$). The scaled value of the minimum in-situ stress, Φ_h, is indicated by the red line as a reference.

sults were compared to those from a conventional model that uses the LEFM propagation criterion. The results have provided an alternative interpretation for the pre-peak pressure microseismic events observed in hydraulic fracture experiments, as well as for the delayed breakdown under subcritical wellbore conditions.

Several conclusions can be made from our study. First, our convergence test implies that the accuracy of the numerical solution is dependent on the element size. This mesh size dependence is less when dimensionless viscosity $\mathcal{M}$ is smaller.

Second, our simulation results indicate a significant impact from subcritical propagation on the hydraulic fracture initiation and growth process. Smaller values of n have larger effect on the evolution of both crack length and wellbore pressure, which leads to earlier initiation and reduced wellbore peak pressure. As n goes to infinity, the solutions converge to those obtained by the classical LEFM model. Therefore, knowing the correct values of subcritical parameters is crucial to better understand and simulate the behavior of hydraulic fracture, especially during the initial stage.

Moreover, the influence of subcritical crack growth vanishes with the increase of the initial crack length γ_0, and the viscosity $\mathcal{M}$.

In addition, earlier initiation and reduced peak wellbore pressure can be achieved by enlarging the wellbore radius.

Finally, deviatoric stress plays an important role in the subcritical crack growth model, as it is also expected in the classical breakdown theory by Hubbert and Willis (1957). A large deviatoric stress can lead to lower peak wellbore pressure.

III. MODELING SIMULTANEOUS INITIATION AND PROPAGATION OF MULTIPLE HYDRAULIC FRACTURES UNDER SUBCRITICAL CONDITIONS

A. PREAMBLE

This chapter comprises a preprint of Lu et al. (Submitted). In this chapter, the numerical model presented in Chapter II is extended to the case of simultaneous growth of multiple hydraulic fractures from horizontal wellbore. Therefore, the impact of subcritical crack growth is studied in the presence of stress interaction among different fractures. This subcritical growth model is validated against available LEFM solutions in limiting cases. Then, comparison is carried out between the solutions obtained from subcritical and LEFM models. It is shown that subcritical crack growth has a profound effect on the growth path of all cracks, with the potential to neutralize the stress shadowing effect. Strikingly, and in contrast to classical HF models, the subcritical HF model predicts initial suppression of and then eventual domination by the middle fracture(s), which is/are predicted to be suppressed due to interaction stress.

B. ABSTRACT

Understanding the mechanisms that govern the simultaneous propagation of multiple hydraulic fractures is challenging since it depends on a variety of factors, such as the stress shadowing effect and coupled elastic behavior of the rock with the fluid flow. In this paper, we develop a numerical model for the initiation and subsequent propagation of an array of

parallel, planar, axisymmetric hydraulic fractures. Unlike conventional numerical models for hydraulic fracture growth, which impose a propagation condition wherein growth occurs only if the stress intensity factor (K_{I}) achieves a value equal to the material fracture toughness (K_{IC}), we allow the fractures to propagate under subcritical conditions ($K_{\mathrm{I}} < K_{\mathrm{IC}}$). With this propagation condition, our numerical model can be used to study time-dependent hydraulic fracture initiation and its impact on the subsequent growth of multiple hydraulic fractures. Our results show that subcritical growth can drastically alter the behavior of the system, in many cases leading to growth of hydraulic fractures which otherwise would be suppressed due to stress shadowing effects.

C. INTRODUCTION

Multi-stage hydraulic fracturing (HF) is an essential technology for completion of horizontal wells in unconventional hydrocarbon reservoirs. In engineering design for multi-stage HF treatments of horizontal well stimulation, it is ideal to promote simultaneous growth of the fractures in all clusters per stage in order to reduce the number of non-producing perforation clusters (Lim et al., 2014; Slocombe et al., 2013). In contrast to the ideal outcome of uniform fracture growth, laboratory experiments with multiple hydraulic fractures indicate that interaction among the hydraulic fractures results in nonuniform growth with one fracture growing longer than the others and eventually dominating and taking all the fluid (El Rabaa, 1989). These so-called "stress shadow" effects have also been evidenced in field data (Bunger and Cardella, 2015) and predicted by numerical simulators (Desroches et al., 2014; Fisher et al., 2004; Germanovich et al., 1997; Meyer and Bazan, 2011).

Predicting the propagation of multiple fractures is a complex task since it hinges on the interplay among various factors, including the stress interaction among the fractures (the stress shadowing), the partitioning of the influx to each fracture, and the coupled fluid flow with elastic deformation in the cracks. Motivated by this challenging and important phenomenon, in recent years, efforts have been made to study the physical mechanisms governing the multiple HF growth, including the interaction among multiple fractures (Bunger

et al., 2012), the energetically advantageous partitioning of fluid among multiple hydraulic fractures (Bunger, 2013; Bunger et al., 2014), and the influence of the viscosity of the injection fluid and the pumping rate (Shin and Sharma, 2014). Furthermore, numerical models have been developed for solving the fully coupled problem of simultaneous growth of multiple fractures (Lecampion and Desroches, 2015; Peirce and Bunger, 2015; Wu and Olson, 2016). These invariably show a tendency for some hydraulic fractures to be suppressed due to stress interaction with other fractures. More insights regarding to the importance of perforation friction and separation between different fractures are given in these studies.

While increased attention has been given to studies of multiple HF growth, subcritical crack growth (Atkinson, 1984; Charles, 1958) is not typically considered as a factor affecting multiple HF growth. However, subcritical crack growth is shown to play a pivotal role in the initiation of hydraulic fracture(s) (Bunger and Lu, 2015; Lu et al., 2017a, 2015). Laboratory experiments on granite (Lu et al., 2015), sandstone and limestone (Lu et al., In review) show that by maintaining a constant subcritical fluid pressure, which is smaller than its critical value required to induce an instantaneous fracture initiation, HF growth can be achieved after a certain period of time. These experimental results indicate a correlation between this time to breakdown and the wellbore pressure. Furthermore, it is suggested that the underlying mechanism that governs the HF breakdown in such a delayed manner is due to the stable crack propagation under subcritical wellbore conditions, i.e., subcritical crack growth. The classical theory of Linear Elastic Fracture Mechanics (LEFM) does not allow fracture initiation when the mode I (opening) stress intensity factor, K_{I}, is less than the fracture toughness (or critical stress intensity factor), K_{IC}. However, according to Atkinson (1984, 1987), fractures can propagate stably under stresses that are insufficient to satisfy such a condition (i.e., when $K_{\mathrm{I}} < K_{\mathrm{IC}}$), with velocities several orders of magnitude smaller than the LEFM propagation velocity. Such crack growth is governed by an empirical power law, referred to as the subcritical crack growth law (Atkinson, 1984; Charles, 1958), for describing the relation between the fracture tip velocity, V, and the stress intensity factor, K_{I}, that is

$$V = A \left(\frac{K_{\mathrm{I}}}{K_{\mathrm{IC}}} \right)^{n} \tag{III.1}$$

where n is the subcritical crack growth index, and A is a constant characteristic velocity

typically taken as an upper bound on the crack propagation speed when $K_I \to K_{\mathrm{IC}}$. Using the subcritical crack growth law (Eq. III.1), numerical simulations have previously been carried out on the initiation and following propagation of a single hydraulic fracture by Lu et al. (2017a). The results show that subcritical growth can lead to a reduced wellbore pressure and increased fracture length compared with the classical model.

Although it is seen that subcritical crack growth can have substantial effect on the single HF growth, its influence on the case of multiple fractures remains unknown. Bunger and Lu (2015) proposed that the time-dependent HF initiation may be one of the fundamental phenomena for generating and growing multiple fractures simultaneously. Thus motivated, in this paper a fully coupled numerical model is presented for solving the initiation and subsequent propagation of an array of N axisymmetric hydraulic fractures that accounts for subcritical fracture growth. This model stems from the classical LEFM model and is integrated with the subcritical crack growth law (Eq. III.1). The problem formulation is given in Section III.D. Section III.E presents the scaling of the governing equations, and details of the numerical algorithm are described in Section III.F. Our numerical solution is validated in Section III.G, and this model is further utilized to study the impact of the key factors. Finally, we draw the conclusions from this work in Section III.H.

D. PROBLEM FORMULATION

1. Model description

We consider the problem of simultaneous initiation and propagation of N axisymmetric, transverse hydraulic fractures growing from a horizontal well with radius a (see Fig. III.1) in an impermeable linearly elastic rock characterized by Young's modulus E, Poisson's ratio ν, and fracture toughness K_{IC}. An incompressible Newtonian fluid with viscosity μ is injected at a constant volumetric rate Q_0 into the wellbore system with a finite compressibility U. For each fracture $I = 1, \ldots, N$, an initial defect of radius R_0^I is assigned for modeling the initiation of the fractures. The spacing, ΔZ, between the fractures in the array is held

constant, and we assume all fractures remain planar while they propagate from a horizontal well under the minimum in-situ stress, σ_n, acting orthogonal to the fracture plane. The interference between fractures can suppress propagation of some fractures, and also cause their propagation paths to curve, but prior studies (Bunger et al., 2012; Xu and Wong, 2013) indicate that the magnitude of curving decreases with increasing in-situ deviatoric stress (i.e., the difference between the maximum and minimum horizontal in-situ stresses). Under a large enough deviatoric stress, which applies to most unconventional hydrocarbon reservoirs, the out-of-plane deflection may be negligible (Xu and Wong, 2013). Of course curving may sometimes be important, but such complexity is beyond the scope of the present work. Furthermore, fluid leak-off to the rock, and the fluid lag (i.e., separation between the fracture tip and the fluid front) is assumed to be negligible.

As depicted in Fig. III.1 , the wellbore is drilled along the direction of minimum in-situ stress σ_n (z direction), and r is the radial coordinate along the direction of crack propagation, with $r = 0$ corresponding to the center of the wellbore. Consequently, we have $r \in \left(a, R^I\right)$ for the Ith crack. The fractures are placed uniformly along the wellbore such that $z^I = (I-1)\,\Delta Z$ for $I = 1, \ldots, N$. Finally, the solution for this problem consists of the fracture radius $R^I(t)$, the crack width $w^I(r,t)$, the wellbore pressure $p_w(t)$, and the fluid pressure $p_f^I(r,t)$ in each fracture I.

2. Governing equations

a. Elasticity Following Lecampion and Desroches (2015), the distributed dislocation theory (Hills et al., 1996) is used to describe the relation of the normal (D_{zz}) and shear (D_{rz}) ring dislocation dipoles with the net stress acting on each of the fractures. For the Ith fracture, the elasticity equation is given in the form of two boundary integral equations for normal and shear net loading along the crack, which are dependent on the fluid pressure p_f, the in-situ stress σ_n, the normal and shear interaction stresses between fractures σ_{int}^I and τ_{int}^I, as well as the near wellbore effect.

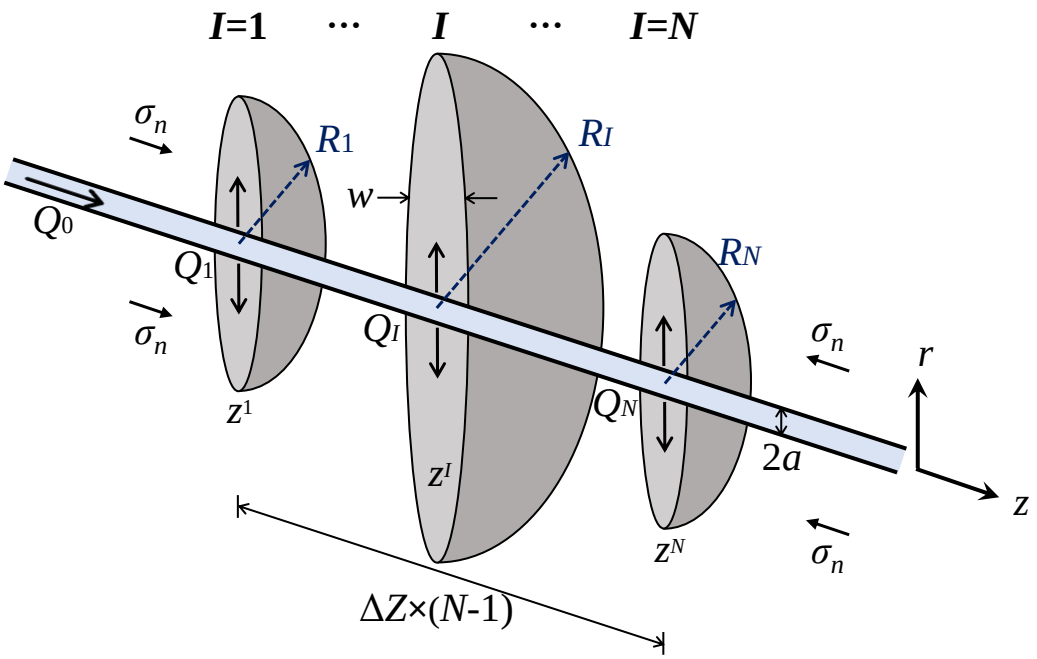

Figure III.1: Sketch of a single stage of multi-stage HF treatment for an array of N axisymmetric hydraulic fractures growing simultaneously from a horizontal wellbore injected by a constant rate Q_0. The fractures are placed along the direction of the well with a constant spacing, ΔZ.

The boundary integral equations are given by

$$\begin{aligned} &p_f\left(r,z^I\right)-\sigma_n\left(r,z^I\right)-\sigma_{int}^I\left(r,z^I\right)= \\ &\int_a^{R^I}\left[\sigma_{zzzz}\left(r,z^I;r',z^I\right)w\left(r',z^I\right)+\sigma_{zzrz}\left(r,z^I;r',z^I\right)v\left(r',z^I\right)\right]dr' \\ &\tau\left(r,z^I\right)=-\tau_{int}^I\left(r,z^I\right)= \\ &\int_a^{R^I}\left[\sigma_{rzzz}\left(r,z^I;r',z^I\right)w\left(r',z^I\right)+\sigma_{rzrz}\left(r,z^I;r',z^I\right)v\left(r',z^I\right)\right]dr' \end{aligned} \tag{III.2}$$

where $w=-D_{zz}$ is the fracture width, and v represents the shear displacement jump, $v=-D_{rz}$, defined by $v(r',z^I)=\lim_{\varepsilon\to 0}\left(u_r(r',z^I+\varepsilon)-u_r(r',z^I-\varepsilon)\right)$. The elastic kernels $\sigma_{ijkl}(r,z;r',z')$ denote the ij component of stress at (r,z) induced by a ring dislocation dipole at (r',z'). These elastic kernels are discussed below (see also Lecampion and Desroches, 2015). Note that for these kernels, in case of a planar fracture, the value of z^I remains constant along the whole crack and $\sigma_{zzrz}(r,z^I;r',z^I)=\sigma_{rzzz}(r,z^I;r',z^I)=0$, i.e. there is no coupling between normal and shear displacement jumps for a single fracture.

Initially, the radius of fracture I is short in comparison both to the wellbore radius and to the spacing between the fractures. In this case, the influence of the wellbore onto the fracture I is substantial, while the influence of the fracture I onto the other fractures is negligible. The elastic kernel for Eq. (III.2) in this case can be obtained from the integral kernel for a ring dislocation in an infinite domain with the cylindrical wellbore, found in Keer et al. (1977). As the fractures grow longer, the wellbore effect vanishes and the interaction stress among the fractures becomes important. According to Lecampion and Desroches (2015), for fractures larger than five to ten times the wellbore radius, the impact of the wellbore becomes negligible, and one can use the elastic kernels Gordeliy and Detournay (2011a) for ring dislocation dipoles in an infinite homogeneous medium (see a detailed discussion in Lecampion and Desroches, 2015).

Therefore in our model, when the crack radius is less than five times the wellbore radius ($R^I\leq 5a$), the elastic kernel for Eq. (III.2) is obtained from the integral kernel for a ring dislocation in an infinite domain with the cylindrical cavity of radius a, found in Eqs. (24) - (29) of Keer et al. (1977). Its mathematical expression is detailed in Abbas and Lecampion (2013) and in Lu et al. (2017a). By using this kernel, the shear displacement jump on the fracture I and the influence of the fracture I onto the other fractures are neglected. For

cracks that are long enough ($R^I > 5a$), the elastic kernels for ring dislocation dipoles in an infinite homogeneous medium Gordeliy and Detournay (2011a) are used, that make it possible to account for the normal and shear displacement jumps on fracture I and for their influence onto the other fractures.

With these considerations, in Eq. (III.2), the interaction stresses are given as

$$\begin{aligned}
&\sigma^I_{int}\left(r, z^I\right) = \\
&\sum_{\substack{J\neq I \\ R^J>5a}} \int_a^{R^J} \left[\sigma_{zzzz}\left(r, z^I; r', z^J\right) w\left(r', z^J\right) + \sigma_{zzrz}\left(r, z^I; r', z^J\right) v\left(r', z^J\right)\right] dr' \\
&\tau^I_{int}\left(r, z^I\right) = \\
&\sum_{\substack{J\neq I \\ R^J>5a}} \int_a^{R^J} \left[\sigma_{rzzz}\left(r, z^I; r', z^J\right) w\left(r', z^J\right) + \sigma_{rzrz}\left(r, z^I; r', z^J\right) v\left(r', z^J\right)\right] dr'
\end{aligned} \tag{III.3}$$

Further details of the integral kernels and the discretization of the boundary integral equations (III.2) are given in Appendix B.A.

b. Fracture initiation and propagation The conventional LEFM model assumes that the fracture propagates under quasi-static equilibrium, with $K_{\mathrm{I}} = K_{\mathrm{IC}}$ at any time for a growing hydraulic fracture. The asymptotic behavior of the opening at the fracture tip is given by the classical square-root asymptote (Rice, 1968)

$$w \sim \frac{K'}{E'}\hat{x}^{1/2}, \quad \hat{x} \to 0 \tag{III.4}$$

where $\hat{x} = R^I - r$ denotes the distance to the crack tip, $E' = E/\left(1-\nu^2\right)$ is the plane strain elastic modulus, and $K' = \sqrt{32/\pi}K_{\mathrm{IC}}$. We refer to this behavior as the toughness ("k") asymptote.

Since the subcritical propagation criterion (Eq. III.1) is introduced in our model, which allows crack growth when $K_{\mathrm{I}} < K_{\mathrm{IC}}$, the LEFM propagation condition needs an appropriate modification. By rewriting the k asymptote (Eq. III.4) as

$$w \sim \sqrt{\frac{32}{\pi}}\frac{K_{\mathrm{I}}}{E'}\hat{x}^{1/2}, \quad \hat{x} \to 0$$

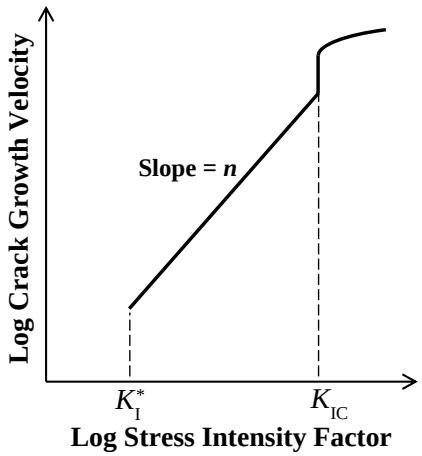

Figure III.2: Log-log plot of the crack tip velocity and the stress intensity factor (after Atkinson, 1987; Olson, 1993). Subcritical crack growth commences when K_I becomes larger than K_I^*.

and using Eq. (III.1), the modified k asymptote is expressed as

$$w \sim \frac{K'}{E'}\hat{x}^{1/2} \cdot \left(\frac{V}{A}\right)^{1/n}, \quad \hat{x} \to 0 \tag{III.5}$$

Such a subcritical tip asymptotic solution is also used in Lu et al. (2017a) for solving the problem of initiation and propagation for a single hydraulic fracture. It is worth noting that, although the fractures can grow subcriticallly ($K_I < K_{IC}$) following the subcritical propagation criterion (Eq. III.5), it is assumed that there is a lower limit for the stress intensity factor, K_I^*, under which value the subcritical growth stops. Fig. III.2 shows the crack tip velocity dependence upon the stress intensity factor (after Atkinson, 1987; Olson, 1993). Following Atkinson (1987) and Olson (1993), we assume that the crack is initiated when $K_I = K_I^* = K_{IC}/10$, and require that $K_I^* \leq K_I \leq K_{IC}$ for the subcritical fracture propagation.

c. Fluid flow The fluid flux $q(r,t)$ in the Ith fracture is governed by the Poiseuille law (Batchelor, 1967). For an incompressible Newtonian fluid with a dynamic viscosity of μ, we have

$$q = -\frac{w^3}{\mu'}\frac{\partial p_f}{\partial r} \quad \text{for} \quad r \in \left(a, R^I\right) \tag{III.6}$$

where $\mu' = 12\mu$. The local continuity equation is derived based on the fluid mass balance

$$\frac{\partial w}{\partial t} + \frac{1}{r}\frac{\partial}{\partial r}(rq) = 0 \tag{III.7}$$

The Reynolds' lubrication equation is then deduced by substituting Eq. (III.6) into Eq. (IV.6)

$$\frac{\partial w}{\partial t} = \frac{1}{\mu' r}\frac{\partial}{\partial r}\left(r w^3 \frac{\partial p_f}{\partial r}\right) \tag{III.8}$$

d. Boundary and initial conditions The pressure in the wellbore is set to be equal to the fluid pressure at the entry of all fractures by assuming no friction loss along the wellbore and at the entry points. Thus, we impose this pressure continuity along the wellbore as

$$p_w(t) = p_f^1(r,t) = p_f^2(r,t) = \cdots = p_f^N(r,t) \quad r \to a \tag{III.9}$$

Such pressure continuity condition is achieved by dynamically partitioning the total fluid volume into fluid volumes injected at the inlet point of each fracture per unit time, $Q_I(t)$. At the well head, the fluid is injected to the wellbore at constant rate, Q_0. Taking into account the compressibility of the injection system, the sum of the fluid influx rates is equal to the total injected volume minus the volume that has been stored due to compressibility effect, which is given by

$$\sum_{I=1}^{N} Q_I(t) = Q_0 - U\frac{dp_w}{dt} \tag{III.10}$$

where U is the system compressibility (volumetric compliance of the injection system). Therefore, $Q_I(t)$ is to be solved for as part of the solution to the problem. Since we make

use of the radially symmetric geometry imposed on all fractures, the inflow rate Q_I is related to the fluid flux inside the axisymmetric crack, $q^I(a,t)$, by

$$Q_I(t) = 2\pi a q^I(a,t) \tag{III.11}$$

Next, for each fracture $I = 1,\ldots,N$, the crack-tip boundary condition imposes vanishing fluid flux and fracture width at the fracture tip (Detournay and Peirce, 2014)

$$r = R^I: \quad w(r,t) = 0, \;\; q(r,t) = 0 \tag{III.12}$$

The initial condition at $t = 0$ is given by a uniform fluid pressure distribution p_f along all initial defects, which is slightly larger than the in-situ stress σ_n, such that very little opening in the cracks is generated, that is

$$t = 0: \quad p_f^I(r,t) = \sigma_n(r) + p_i, \;\; R^I = R_0^I \quad \left(a < r < R_0^I\right) \tag{III.13}$$

where p_i is a small initial net pressure assumed to exist in the crack, and R_0^I is the initial fracture radius.

E. SCALING

The system of governing equations and boundary/initial conditions given in Section 2. presents a complex problem which involves a cumbersome number of governing parameters. Here we use a scaling method (after Abbas and Lecampion, 2013; Lu et al., 2017a) to reduce the dimensionality of the parametric space by introducing the following dimensionless variables

$$\begin{gathered}\gamma^I = \tfrac{R^I}{R_*}, \;\; \mathcal{A} = \tfrac{a}{R_*}, \;\; \rho = \tfrac{r}{R_*}, \;\; \zeta = \tfrac{z}{R_*}, \;\; \Omega = \tfrac{w}{w_*}, \;\; \Psi = q\tfrac{R_*}{Q_*}; \\ \mathcal{T} = \tfrac{t}{t_*}, \;\; \hat{\sigma} = \tfrac{\sigma}{p_*}, \;\; \hat{\tau} = \tfrac{\tau}{p_*}, \;\; \Pi_w = \tfrac{p_w}{p_*}, \;\; \Pi_f = \tfrac{p_f}{p_*}.\end{gathered} \tag{III.14}$$

where t_*, R_*, w_*, p_*, and Q_* are the 5 characteristic scales for time, radius, crack width, pressure, and fluid flux. As in Lu et al. (2017a), we use a so-called "compressibility-toughness" (UK) scaling to compute the values of these characteristic scales as

$$R_* = (E'U)^{1/3}, \quad t_* = \frac{K'U^{5/6}}{Q_0 E'^{1/6}}, \quad p_* = \frac{K'}{(E'U)^{1/6}}, \\ w_* = \frac{K'U^{1/6}}{E'^{5/6}}, \quad Q_* = Q_0. \tag{III.15}$$

This scaling is based on the characteristic time and radius scales associated with the release of the volume compressed in the injection system prior to fracture initiation. Therefore, when the fracture attains a radius much greater than the characteristic radius, R_*, the impact of the compressed volume in the injection system vanishes. Similarly, when the injection time greatly exceeds the characteristic time, t_*, the impact of the compressed volume in the injection system vanishes. These characteristic quantities are found by rewriting the governing equations in terms of the dimensionless variables (Eq. III.14) and the dimensionless groups that are combinations of the parameters K', E', μ', Q_0 and U (Abbas and Lecampion, 2013). In doing so, the dimensionless groups associated with injection rate, compressibility, and fracture toughness are all set to be 1, and the characteristic scales (Eq. III.15) result. Consequently, the only characteristic parameters that appear in the scaled governing equations are the subcritical index, n, the dimensionless viscosity, given by

$$\mathcal{M} = \frac{\mu' Q_0 E'^{8/3}}{K'^4 U^{1/3}}, \tag{III.16}$$

and the scaled subcritical constant, wellbore radius, initial HF radii, and the scaled location of each fracture along the wellbore given, respectively, by

$$\alpha = \frac{K'U^{1/2}}{Q_0 E'^{1/2}} A; \quad \mathcal{A} = \frac{a}{R_*}; \quad \gamma_0^I = \frac{R_0^I}{R_*}; \quad \zeta^I = \frac{Z^I}{R_*}. \tag{III.17}$$

It is worthwhile to note that the scaling is derived based on the surface injection rate, Q_0, and the influx rate for each of the N fractures, Q_I, would certainly be smaller than the total rate. During the propagation of multiple fractures, it is possible that fractures are growing under different dominating regimes.

Based on the scaling method, we can rewrite the governing equations and boundary and initial conditions in the following dimensionless forms:

a. Elasticity For the axisymmetric DD formulation, we obtain

$$\begin{aligned}
&\Pi_f\left(\rho,\zeta^I\right)-\hat{\sigma}_n\left(\rho,\zeta^I\right)-\hat{\sigma}^I_{int}\left(\rho,\zeta^I\right)= \\
&\int_{\mathcal{A}}^{\gamma^I}\left[\bar{\sigma}_{zzzz}\left(\rho,\zeta^I;\rho',\zeta^I\right)\Omega\left(\rho',\zeta^I\right)+\bar{\sigma}_{zzrz}\left(\rho,\zeta^I;\rho',\zeta^I\right)\hat{v}\left(\rho',\zeta^I\right)\right]d\rho' \\
&\hat{\tau}\left(\rho,\zeta^I\right)=-\hat{\tau}^I_{int}\left(\rho,\zeta^I\right)= \\
&\int_{\mathcal{A}}^{\gamma^I}\left[\bar{\sigma}_{rzzz}\left(\rho,\zeta^I;\rho',\zeta^I\right)\Omega\left(\rho',\zeta^I\right)+\bar{\sigma}_{rzrz}\left(\rho,\zeta^I;\rho',\zeta^I\right)\hat{v}\left(\rho',\zeta^I\right)\right]d\rho'
\end{aligned} \tag{III.18}$$

where $\rho'=\frac{r'}{R_*}$, $\bar{\sigma}_{ijkl}$ denote the scaled elastic kernels, and $\hat{v}$ is the scaled shear displacement discontinuity written as $\hat{v}=v/w_*$. The interaction stresses are given by

$$\begin{aligned}
&\hat{\sigma}^I_{int}\left(\rho,\zeta^I\right)= \\
&\sum_{\substack{J\neq I\\ \gamma^J>5\mathcal{A}}}\int_{\mathcal{A}}^{\gamma^J}\left[\bar{\sigma}_{zzzz}\left(\rho,\zeta^I;\rho',\zeta^J\right)\Omega\left(\rho',\zeta^J\right)+\bar{\sigma}_{zzrz}\left(\rho,\zeta^I;\rho',\zeta^J\right)\hat{v}\left(\rho',\zeta^J\right)\right]d\rho' \\
&\hat{\tau}^I_{int}\left(\rho,\zeta^I\right)= \\
&\sum_{\substack{J\neq I\\ \gamma^J>5\mathcal{A}}}\int_{\mathcal{A}}^{\gamma^J}\left[\bar{\sigma}_{rzzz}\left(\rho,\zeta^I;\rho',\zeta^J\right)\Omega\left(\rho',\zeta^J\right)+\bar{\sigma}_{rzrz}\left(\rho,\zeta^I;\rho',\zeta^J\right)\hat{v}\left(\rho',\zeta^J\right)\right]d\rho'
\end{aligned} \tag{III.19}$$

b. Poiseuille law The scaled Poiseuille law for Ith crack is written as

$$\Psi=-\frac{1}{\mathcal{M}}\Omega^3\frac{\partial\Pi_f}{\partial\rho}\quad\text{for}\quad\rho\in\left(A,\gamma^I\right) \tag{III.20}$$

c. Continuity The fluid continuity equation is given by

$$\frac{\partial\Omega}{\partial\mathcal{T}}+\frac{1}{\rho}\frac{\partial\bar{\Psi}}{\partial\rho}=0 \tag{III.21}$$

in which the modified fluid flux inside every crack is $\bar{\Psi}=\rho\Psi$.

d. Lubrication Upon substitution of Eq. (III.20) into Eq. (III.21) the scaled lubrication equation is given by

$$\frac{\partial\Omega}{\partial\mathcal{T}}=\frac{1}{\mathcal{M}\rho}\frac{\partial}{\partial\rho}\left(\rho\Omega^3\frac{\partial\Pi_f}{\partial\rho}\right) \tag{III.22}$$

e. Propagation condition After scaling, the propagation condition is given by

$$\Omega \sim \hat{\xi}^{1/2} \left(\frac{\upsilon}{\alpha}\right)^{1/n}, \quad \hat{\xi} \to 0, \, \upsilon \leq \alpha \tag{III.23}$$

where $\upsilon = d\gamma/d\mathcal{T}$ is the dimensionless fracture tip velocity, and $\hat{\xi} = \gamma - \rho$.

f. Boundary conditions The pressure continuity is scaled as

$$\Pi_w \left(\mathcal{T}\right) = \Pi_f^1 \left(\rho, \mathcal{T}\right) = \Pi_f^2 \left(\rho, \mathcal{T}\right) = \cdots = \Pi_f^N \left(\rho, \mathcal{T}\right), \quad \rho = \mathcal{A} \tag{III.24}$$

The global volume balance is given by

$$\sum_{I=1}^{N} \psi_I \left(\mathcal{T}\right) = 1 - \frac{d\Pi_w}{d\mathcal{T}} \tag{III.25}$$

in which the inflow rate is non-dimensionalized by $\psi_I = Q_I/q_*$, and is related to the fluid flow rate inside the crack via the inlet boundary condition, which is expressed as

$$\psi_I \left(\mathcal{T}\right) = 2\pi \bar{\Psi}^I \left(\mathcal{A}, \mathcal{T}\right), \quad I = 1, \ldots, N \tag{III.26}$$

Then, the boundary condition at the tip is

$$\rho = \gamma^I : \quad \Omega \left(\rho, \mathcal{T}\right) = 0, \;\; \bar{\Psi} \left(\rho, \mathcal{T}\right) = 0 \tag{III.27}$$

g. Initial condition The initial condition is written as

$$\mathcal{T} = 0 : \quad \Pi_{net} \left(\rho, \mathcal{T}\right) = \Pi_i, \;\; \gamma^I = \gamma_0^I \quad \left(\mathcal{A} < \rho < \gamma_0^I\right) \tag{III.28}$$

where $\Pi_i = p_i/p_*$ is a small initial net pressure sufficient to slightly open the initial crack.

In summary, by solving the system of scaled governing equations and boundary/initial conditions, we seek the solution $\{\boldsymbol{\gamma}, \boldsymbol{\Omega}, \boldsymbol{\Pi}, \boldsymbol{\Psi}\}$ as a function of spatial $\left\{\rho, \zeta^I\right\}$ and time $(\mathcal{T})$ variables using the numerical method described in the following section.

F. NUMERICAL ALGORITHM

1. Overview

The numerical algorithm follows in the spirit of previous contributions for simulations of multiple hydraulic fractures (Lecampion and Desroches, 2015; Peirce and Bunger, 2015), and is based on a time-controlled, implicit level set algorithm (ILSA) developed by Peirce and Detournay (2008). We discretize every fracture with a fixed grid of elements with the element size $\triangle\rho^I$. The elastic equation (III.18) is discretized by assuming a piece-wise constant crack width, and a 1D finite difference scheme is used for discretization of the lubrication equation (III.22).

For every step with a fixed time increment of $\triangle\mathcal{T}$, the algorithm first checks for each crack whether the mobility condition is satisfied (i.e., $K_{\rm I} > K_{\rm I}^*$), and the crack radius γ^I is fixed if this condition is not met. Two loops are constructed to solve the coupled non-linear problem for every time step. The outer loop in the algorithm solves the new crack radius γ^I for all growing cracks. The inner loop uses Newton's method to iterate on the inflow rate ψ_I for all cracks (mobile or not) based on trial values of crack radii obtained in the outer loop. An additional iterative scheme is required in the inner loop to solve the non-linear system of the solid-fluid coupling, including the stress interference among the fractures. In the outer loop, the ILSA algorithm is used for computing the new fracture radius via inversion of the subcritical tip asymptote. According to ILSA, the position of fracture front is allowed to be located inside an element (i.e., the crack front does not have to lie at boundaries between two elements, and the element that contains the fracture tip is treated as partly opened), which makes it possible to advance multiple cracks with different propagation velocities simultaneously. At the current time step, each growing hydraulic fracture is divided into two regions (see Fig. III.3):

I. The "channel" region includes all elements that were completely open in the previous time step, and the last element of the channel is defined as the "ribbon element";

II. The "tip" region consists of the rest of the elements along the crack, from the previous tip element to the new fracture front estimated by ILSA.

Note that in our notation, we use the subscript t for "tip" and c represents "channel". Therefore, in the fracture front loop, m_t denotes the total number of elements along the crack (this value is updated in every ILSA iteration), and m_c gives the number of elements in the "channel" region (which remains constant during one time step). Such a time-stepping algorithm is described in detail in Section III.F.5.

2. Elasticity

The displacement discontinuity (DD) method (Crouch and Starfield, 1983) is used for discretizing the elasticity equation (III.2) into a linear system of equations. Each crack is discretized into a mesh of m^I DD elements with the element size $\triangle\rho^I$. The midpoint of each element i in the Ith crack is assigned the coordinate: $\rho_i^I = \mathcal{A} + (i - 1/2)\triangle\rho^I, i = 1, ..., m^I$, and this element i is characterized by a constant width Ω_i^I. By evaluating the integrals of the stress kernels over each element, and by eliminating the shear displacement jump via static condensation, the vectors of nodal fluid pressure, $\mathbf{\Pi}$, and the nodal fracture opening, $\mathbf{\Omega}$ can be related by

$$\mathbf{\Pi}_{\mathrm{f}} = \mathbf{C}\mathbf{\Omega} - \mathbf{S} \tag{III.29}$$

where $\mathbf{C}$ is the elasticity influence matrix, and the vector $\mathbf{S}$ accounts for the normal stress acting on the fracture induced by the in-situ stress and the interaction stress. Further details of the components of $\mathbf{C}$ and $\mathbf{S}$ are given in Appendix B.A.

3. Lubrication

We discretize the Reynolds' lubrication equation (III.22) using a finite difference scheme. Combining the Poiseuille law (III.20) and the continuity equation (III.21), together with the

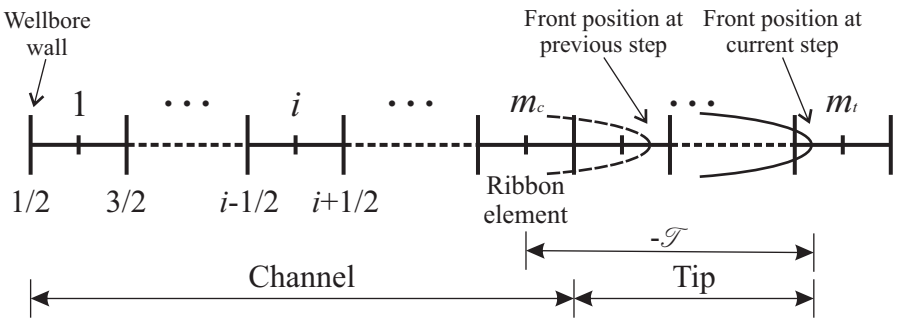

Figure III.3: Geometrical interpretation of the one-dimensional hydraulic fracturing propagation problem solved by a time-controlled algorithm (after Lecampion and Desroches, 2015; Peirce and Detournay, 2008). At the current time step, the fracture is discretized by a fixed grid, in which the channel region contains all completely opened elements from the previous step and the rest of the elements along the crack (including the partly opened element at current crack tip) belong to the tip region.

boundary conditions at inlet points, Eq. (III.26), and at the tips, Eq. (III.27), the discretized lubrication equation for fracture I is

$$\begin{aligned}
\triangle\Omega_1 &= \tfrac{\Delta\mathcal{T}}{\rho_1\Delta\rho}\left[K_1\left(\Pi_2-\Pi_1\right)+\tfrac{\psi_I}{2\pi}\right], \\
\triangle\Omega_i &= \tfrac{\Delta\mathcal{T}}{\rho_i\Delta\rho}\left[K_i\Pi_{i+1}+K_{i-1}\Pi_{i-1}-\left(K_i+K_{i-1}\right)\Pi_i\right], \quad i=1,\ldots,m-1 \\
\triangle\Omega_m &= \tfrac{\Delta\mathcal{T}}{\rho_m\Delta\rho}\left[-K_{m-1}\Pi_m+K_{m-1}\Pi_{m-1}\right]
\end{aligned} \tag{III.30}$$

where $K_i=\frac{\rho_{i+1/2}}{\mathcal{M}\triangle\rho}\left(\frac{\Omega_i+\Omega_{i+1}}{2}\right)^3$, $\rho_{i+1/2}=\frac{\rho_i+\rho_{i+1}}{2}$, $\triangle\Omega_i=\Omega_i\left(\mathcal{T}\right)-\Omega_i\left(\mathcal{T}_0\right)$, and $\Omega_i\left(\mathcal{T}_0\right)$ denotes the width from the previous time step $\mathcal{T}_0$. Note that in Eq. (III.30), $m=m_t=m^I$, and we drop the superscript âIâ from Π, Ω, ρ, and $\Delta\rho$ for brevity. Eq. (III.30) can also be expressed in matrix form as

$$\boldsymbol{\Delta\Omega}=\triangle\mathcal{T}\mathbf{D}\cdot\boldsymbol{\Pi}+\boldsymbol{\Lambda} \tag{III.31}$$

in which $\mathbf{D}$ is a tridiagonal matrix, and the vector $\boldsymbol{\Lambda}=\begin{bmatrix}\frac{\triangle\mathcal{T}\psi_I}{2\pi\rho_1\Delta\rho} & 0 & \cdots & 0\end{bmatrix}^{\mathrm{T}}$ accounts for the influx boundary condition for each hydraulic fracture.

4. Mixed-variable coupled system

We recall that every crack is divided into channel (c) and tip (t) regions. Hence, Eq. (III.31) can also be decomposed into two parts:

$$\begin{aligned}
\boldsymbol{\Delta\Omega}^c &= \triangle\mathcal{T}\left(\mathbf{D}^{cc}\cdot\boldsymbol{\Pi}^c+\mathbf{D}^{ct}\cdot\boldsymbol{\Pi}^t\right)+\boldsymbol{\Lambda}^c \\
\boldsymbol{\Delta\Omega}^t &= \triangle\mathcal{T}\left(\mathbf{D}^{tc}\cdot\boldsymbol{\Pi}^c+\mathbf{D}^{tt}\cdot\boldsymbol{\Pi}^t\right)
\end{aligned} \tag{III.32}$$

By substituting Eq. (III.32) into the elasticity equation (III.29), we obtain the non-linear equation

$$\begin{aligned}
&\begin{bmatrix}\mathbf{I}-\triangle\mathcal{T}\mathbf{D}^{cc}\mathbf{C}^{cc} & -\triangle\mathcal{T}\mathbf{D}^{ct}\\ -\triangle\mathcal{T}\mathbf{D}^{tc}\mathbf{C}^{cc} & -\triangle\mathcal{T}\mathbf{D}^{tt}\end{bmatrix}\begin{bmatrix}\boldsymbol{\Delta\Omega}^c\\ \boldsymbol{\Pi}^t\end{bmatrix} \\
&=\begin{bmatrix}\triangle\mathcal{T}\mathbf{D}^{cc}\left(\mathbf{C}^{cc}\boldsymbol{\Omega}^c\left(\mathcal{T}_0\right)+\mathbf{C}^{ct}\boldsymbol{\Omega}^t-\mathbf{S}^c\right)+\boldsymbol{\Lambda}^c\\ -\boldsymbol{\Delta\Omega}^t+\triangle\mathcal{T}\mathbf{D}^{tc}\left(\mathbf{C}^{cc}\boldsymbol{\Omega}^c\left(\mathcal{T}_0\right)+\mathbf{C}^{ct}\boldsymbol{\Omega}^t-\mathbf{S}^c\right)\end{bmatrix}
\end{aligned} \tag{III.33}$$

where $\mathbf{I}$ is the $m_c \times m_c$ identity matrix. For a given crack opening in the tip region $\mathbf{\Omega}^t$ (its value will be discussed in the following section), Eq. (III.33) is solved using a fixed-point iteration method. At iteration j, the solution for the unknown vector, $[\mathbf{\Delta\Omega}^c; \mathbf{\Pi}^t]$, is found from the following linear system

$$\mathbf{\Xi}\left(\mathbf{U}^j\right)\mathbf{U}^{j+1} = \mathbf{\Gamma}\left(\mathbf{U}^j\right) \tag{III.34}$$

in which $\mathbf{U} = [\mathbf{\Delta\Omega^c}; \mathbf{\Pi^t}]$, and the matrix $\mathbf{\Xi}$ and the vector $\mathbf{\Gamma}$ are found according to Eq. (III.33). Note that, for the case of multiple fractures, the vector $\mathbf{S}$ accounts for the interaction stress acting on the Ith fracture due to opening of other cracks, and its value depends on the width of all cracks that are longer than $5a$, i.e., $J = 1, \ldots, N;\ J \neq I;\ \gamma^J > 5a$ (see details in Appendix B.A). Therefore, an iterative method is necessary for computing the increment of opening, $\mathbf{\Delta\Omega}^c$, for all cracks which includes the coupling of the interference among the fractures. We construct a loop to update $\mathbf{S}$ after obtaining the values of $\mathbf{\Delta\Omega}^c$ (via Eq. III.34) for all cracks, until convergence in the solution is achieved.

5. The implicit level set algorithm

The ILSA developed by Peirce and Detournay (2008) is adopted here to update the position of the fracture front, given the estimate of fracture width at the ribbon element. This method hinges on the dominance of the tip region as well as the last element in channel region (ribbon element) by the asymptotic behavior. Therefore, the opening of the ribbon element, Ω_r, has the subcritical asymptotic correlation (Eq. III.23) with the distance to crack tip, $\hat{\xi}_r$. According to Peirce and Detournay (2008), the crossing-time map, $\mathscr{T}$, is defined as the inversion of the tip asymptote (Eq. III.23), which is given by

$$\mathscr{T} \equiv -\hat{\xi}_r \sim -\Omega_r^2 \left(\frac{\alpha}{\upsilon}\right)^{2/n} \tag{III.35}$$

By expressing the crack propagation velocity as

$$\upsilon = -\frac{\mathscr{T} - \mathscr{T}_0}{\triangle\mathcal{T}}$$

where $\mathscr{T}_0$ is the crossing-time map associated with previous time step $\mathcal{T}_0$, then we obtain the following equation for $\mathscr{T}$

$$\mathscr{T} + \Omega_r^2 \frac{(\triangle \mathcal{T} \alpha)^{2/n}}{(\mathscr{T}_0 - \mathscr{T})^{2/n}} = 0 \tag{III.36}$$

In this way, knowing the opening at the ribbon element, Ω_r, we compute the value of $\mathscr{T}$ by solving Eq. (III.36), and obtain the new estimated fracture radius

$$\gamma = \gamma(\mathcal{T}_0) + \mathscr{T}_0 - \mathscr{T} \tag{III.37}$$

Since the fracture width in the crack tip region follows the subcritical asymptotic behavior, the fluid volumes in all elements in the tip region can be expressed using the tip asymptote, i.e. $\Delta\rho \cdot \Omega_i = \int_{\gamma-\rho_{i+1/2}}^{\gamma-\rho_{i-1/2}} \hat{\xi}^{1/2} \kappa d\hat{\xi}$ for $i = m_c + 1, \ldots, m_t$, in which $\kappa = \left(\frac{v}{\alpha}\right)^{1/n}$ denotes the dimensionless stress intensity factor. Thus, by knowing the estimated fracture radius, the crack opening, Ω_i, in the tip region can be computed.

To set an initial value for Ω_r, we impose the crack to remain static in the first iteration of the fracture front loop (i.e., no fracture propagation from the previous time step at the first iteration on the fracture front) and Eq. (III.33) is solved to obtain the increment in crack width along the whole crack (including both channel and tip regions). For the following iterations, the ILSA algorithm updates the fracture radius, until convergence is reached. For each trial value of the fracture radius, Eq. (III.33) is solved, and the obtained opening in the ribbon element, Ω_r, is used to solve Eq. (III.36) and update the fracture radius via Eq. (III.35). Such a numerical scheme was first developed for solving the problem of a single hydraulic fracture Peirce and Detournay (2008), and was used for modeling multiple fractures in Peirce and Bunger (2015) as well as Lecampion and Desroches (2015). For multiple fractures, it can be conducted on each fracture: at each ILSA iteration, all fracture widths are updated simultaneously (taking into account the elastic interference between the fractures), and then the fracture radii are updated using the crack widths in ribbon element until achieving an overall convergence.

6. Solution for fluid partitioning

The fluid influx rate into different fractures $\boldsymbol{\psi} = (\psi_1, \ldots, \psi_N)$ is adjusted dynamically based on the effect of solid-fluid coupling in each fracture and elastic interference among different fractures. As a result of the fluid partitioning, pressure continuity condition (III.24) should be satisfied at any time step. In our model, we solve for the inlet flow rate $\boldsymbol{\psi}$ numerically using the Newton's method by finding the zeros of the residual vector $\mathbf{r} = (r_1, \ldots, r_N)$, with

$$r_I = \frac{\Pi_w(\boldsymbol{\psi}) - \Pi_f^{I1}(\boldsymbol{\psi})}{\Pi_w(\boldsymbol{\psi})} \quad I = 1, \ldots, N \tag{III.38}$$

where Π_f^{I1} denotes the fluid pressure at the midpoint of the first element (inlet point) in fracture I. In Eq. (III.38), $\Pi_w(\psi)$ is computed by the global volume balance, given by

$$\Pi_w(\boldsymbol{\psi}, \mathcal{T}) = \Pi_w(\boldsymbol{\psi}, \mathcal{T}_0) + \Delta\mathcal{T} - \sum_{I=1}^{N} \psi_I \cdot \Delta\mathcal{T} \tag{III.39}$$

7. Numerical scheme

The components of the algorithm in a single time step are briefly summarized as follows (K and k denote the iteration counters in the outer and the inner loop, respectively, and ε is the tolerance):

1. Given solution at $\mathcal{T} = \mathcal{T}_0$ $(\boldsymbol{\Omega}(\mathcal{T}_0), \gamma(\mathcal{T}_0), \kappa(\mathcal{T}_0))$;
2. Advance time step: $\mathcal{T} \leftarrow \mathcal{T}_0 + \Delta\mathcal{T}$;
3. Fracture front (outer) loop to find new front positions $\gamma(\mathcal{T})$;
   (1). Inner loop to find fluid partitioning $\boldsymbol{\psi}$;
   Solve unknown vector $\mathbf{U}$ in the mixed-variable coupled system described in Section III.F.4 for all cracks, including an extra loop that accounts for the interaction stress;
   Compute Π_w using Eq. (III.39), update $\boldsymbol{\psi}^{k+1}$ via Newton's method for solving residual function $\mathbf{r} = \mathbf{0}$ (Eq. III.38) until $\|\boldsymbol{\psi}^{k+1} - \boldsymbol{\psi}^k\| < \varepsilon\|\boldsymbol{\psi}^k\|$;
   (2). Update γ^{K+1}, $\boldsymbol{\Omega}^{K+1}$ for all cracks via ILSA (Section III.F.5);
   (3). Check for convergence $\|\gamma^{K+1} - \gamma^K\| < \varepsilon\|\gamma^K\|$;
4. Update $\boldsymbol{\Omega}(\mathcal{T})$, $\kappa(\mathcal{T})$, $\gamma(\mathcal{T})$, go to next time step.

G. NUMERICAL RESULTS

1. Validation

a. Initiation and subsequent growth of a single hydraulic fracture under subcritical conditions We first test our model on a single radially symmetric hydraulic fracture propagating from a horizontal wellbore driven by a constant injection rate. Our numerical results for an axisymmetric fracture's growth under the subcritical propagation condition (with an intermediate subcritical index $n = 40$) injected by a fluid with either small or large viscosity ($\mathcal{M} = 0.001$ and $\mathcal{M} = 1$) are compared with those from previously developed single subcritical HF model "SCRIF" (Lu et al., 2017a) (which implements a length-controlled algorithm in contrast to the time-controlled algorithm used here). The values of $\mathcal{M}$ are chosen such that each of the case represents a hydraulic fracture growth under a specific propagation regime (Savitski and Detournay, 2002), i.e., toughness-dominated regime when $\mathcal{M} = 0.001$, and viscosity-dominated regime when $\mathcal{M} = 1$. For both cases, the in-situ stress is set to be zero and except for the viscosity $\mathcal{M}$, the values for all other dimensionless parameters are taken to be the same. Fig. III.4 gives the relation of crack radius and wellbore pressure with time. An overall convergence between the two numerical solutions is observed for all cases. The largest difference occurs when the wellbore pressure reaches its peak value in the larger viscosity case ($\mathcal{M} = 1$), which has a relative difference of 7%.

b. Comparison with solution obtained from classical HF model for multiple hydraulic fractures Here we consider an array of three hydraulic fractures initiating and propagating from a horizontal wellbore in an infinite domain, following the example previously considered under the LEFM assumption by Lecampion and Desroches (2015). The numerical model developed by Lecampion and Desroches (2015) uses the classical tip asymptotics as the propagation criterion for fracture growth (i.e., $K_I = K_{\mathrm{IC}}$ is required for propagation). The code was made available to the authors and we were able to use the same values for all parameters and compare the numerical solution from both models. Initially, three fractures ($N = 3$) are placed along the wellbore with fractures 1 and 3 on the outside

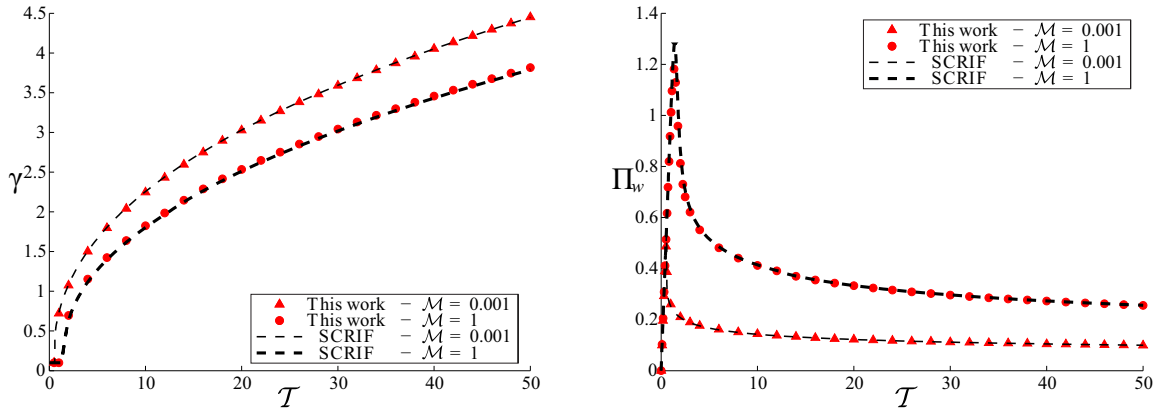

Figure III.4: Evolution of fracture radius (left) and wellbore pressure (right) for the propagation of a radially symmetric fracture under subcritical condition with the subcritical index $n = 40$ and varying fluid viscosity ($\mathcal{M} = 0.001$ or $\mathcal{M} = 1$). The confining stress $\hat{\sigma}_n$ is set to be zero for all cases.

and fracture 2 placed in the middle (spacing $\Delta Z = 25\,\mathrm{m}$). The initial radii for all cracks are set to be same as the wellbore radius. The values of the simulation parameters are given as: $\sigma_n = 37.2\,\mathrm{MPa}$; $E' = 26\,\mathrm{GPa}$; $K_{\mathrm{IC}} = 1.2\,\mathrm{MPa}\sqrt{\mathrm{m}}$; $\mu = 0.005\,\mathrm{Pa}\cdot\mathrm{s}$; $Q_0 = 0.159\,\mathrm{m}^3/\mathrm{s}$; $U = 1.84 \times 10^{-8}\,\mathrm{m}^3/\mathrm{Pa}$; $\Delta Z = 25\,\mathrm{m}$; $a = 6.9\,\mathrm{cm}$; $R_0^I/a = 1$. Note that in Lecampion and Desroches (2015) the volumetric compressibility U is taken into account by modeling the fluid flow in the wellbore (see detailed discussion in Lecampion and Desroches (2015)). Therefore the values of relevant parameters in the model of Lecampion and Desroches (2015) (the cross-sectional area of the flow A, fluid compressibility c, and total length of pressurized well L) are assigned such that the same effect of the injection system compressibility, equivalent to U ($Ac \times L = U$), is recovered in the simulation. Additionally, since we impose the pressure continuity condition throughout the entire wellbore, the perforation friction in Lecampion and Desroches (2015) is also set to be zero. Finally, it is shown in Lu et al. (2017a) that the subcritical tip asymptote reduces to the classical k asymptote when the subcritical index n is large enough. Therefore, for the purpose of verification, we set $n = 200$ and $A = 1000\,\mathrm{m/s}$

in our subcritical growth model, which has previously been shown to generate consistent results with those obtained from the classical LEFM model (Lu et al., 2017a).

Fig. III.5 shows the evolution of crack radius R and influx Q_I for all hydraulic fractures. By comparing the two solutions, consistent results are observed in the evolution of inflow rate of all cracks. As for the fracture radius, the trend of fracture #2 being squeezed by the two outer fractures 1 and 3 is seen in both results when the hydraulic fractures grow long enough and the stress interference among fractures becomes appreciable. An overall agreement of the two models can be seen, with slightly larger crack radius obtained from the subcritical crack growth model in long term propagation, compared to the classical HF solution. To this point, it is found by Lu et al. (2017a), in the case of single hydraulic fracture growth, that subcritical crack growth results in a greater crack length compared to the classical LEFM solution. Furthermore, as n increases, the effect of subcritical growth vanishes and an overall tendency of the prediction for crack growth converging to the classical solution can be found (see detailed numerical results for n=10, 40 and 200 in Lu et al., 2017a). An even larger value of n (n=1000) was used in Lu et al. (2017a) for simulating the case that n goes to infinity, and the numerical prediction for crack growth shows consistency with the LEFM solution in long term propagation. Therefore, it is reasonable to conclude that, by comparing the results with the numerical model of Lecampion and Desroches (2015), we have verified our model for the initiation and propagation of multiple fractures. The slight difference in the crack radius is due to the impact of the subcritical crack growth.

2. Solution for multiple HF initiation and propagation under subcritical conditions

As shown in detail by Lu et al. (2017a), for the case of a single hydraulic fracture, subcritical crack growth has a significant impact on both the initiation and the subsequent propagation. The change in subcritical index, n, also has a prominent effect on the evolution of crack radius and wellbore pressure, with smaller n resulting in earlier initiation, longer crack radius, and reduced wellbore peak pressure. We now investigate the influence of varying n for the case of more than one hydraulic fractures growing simultaneously. An array of three fractures

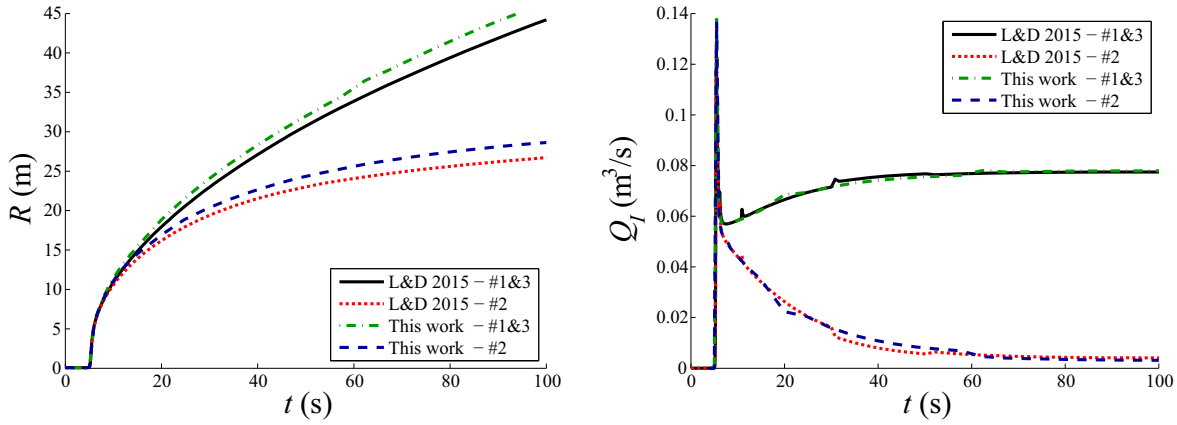

Figure III.5: Evolution of fracture radius (left) and influx (right) for an array of three evenly spaced fractures emanating from a horizontal wellbore with the subcritical index $n = 200$. Our solution is compared with those obtained from the numerical model developed by Lecampion and Desroches (2015), which imposes classical LEFM propagation criterion ($K_{\mathrm{I}} = K_{\mathrm{IC}}$).

is used for this illustration ($N = 3$). The values for the other parameters are given as: $\sigma_n = 30\,\text{MPa}$; $E' = 16.5\,\text{GPa}$; $K_{\text{IC}} = 1.8\,\text{MPa}\sqrt{\text{m}}$; $\mu = 0.001\,\text{Pa}\cdot\text{s}$; $Q_0 = 0.05\,\text{m}^3/\text{s}$; $U = 1.84\times10^{-8}\,\text{m}^3/\text{Pa}$; $\Delta Z = 15\,\text{m}$; $a = 6.9\,\text{cm}$; $R_0^I/a = 1/3$. The resulting global dimensionless viscosity is $\mathcal{M} = 0.368$, and the compressibility lengthscale R_* that is associated with the vanishing effect of the wellbore is given as $R_* = 6.7$ m. Two cases of large and small subcritical index $n = 200$ and $n = 20$ are used to explore the role of subcritical index on the overall behavior of every fracture. Fig. III.6a gives the relation of crack radius R_I versus injection time t for all three cracks. As expected, an earlier initiation is observed in the case of $n = 20$, compared to the case with a larger $n = 200$. Again, for both cases, we see that the growth of the middle fracture (#2) is suppressed by the two outer fractures (#1 and #3) as they start to interact with each other, and eventually it stops growing completely due to the strong elastic interference. It is also implied that as n decreases, all cracks (including the middle crack that is being squeezed by the other two cracks on the edges) tend to grow longer.

It is also of interest to explore the impact of fluid viscosity and injection rate. Assuming that the flow rate is evenly split into all three cracks, i.e., $Q_I = Q_0/3$ for $I = 1, \ldots, N$. Note that the fluid partitioning into each crack is dependent on various factors such as the solid-fluid coupling in every fracture and the elastic interaction among different fractures. Thus, the amount of fluid flows into all cracks is certainly not evenly split and it evolves with time. The exact values of the inflow rates are obtained by using the Newton's method detailed in Section III.F.6. Here we only use this rate for the sake of estimating a global propagation regime. With this value, the scaled viscosity $\mathcal{M} = 0.368$, suggesting the hydraulic fractures are likely to grow in an intermediate regime (compared to the limiting regimes of toughness-dominated or viscosity-dominated). To illustrate the effect of fluid viscosity, we also run another simulation with the fluid viscosity $\mu = 0.1\,\text{Pa}\cdot\text{s}$ while keeping the same values for all other parameters. Thus, in the second case, the scaled viscosity now becomes $\mathcal{M} = 36.8$, which is expected to lead to HF growth of all cracks in the viscosity-dominated regime. As in the previous case, two values for n are used in the simulation, and the evolution of crack radius is plotted in Fig. III.6b. It is shown that for both inner and outer fractures, the radius evolution almost overlaps each other between the two cases of different n, indicating that

effect of subcritical growth vanishes and our results merge to the classical HF solution. Note that a similar observation has been made for a single hydraulic fracture, specifically, that the subcritical crack growth becomes less important as the fluid viscosity increases Lu et al. (2017a).

Now we turn to the evolution of wellbore pressure with time (see Fig. III.7). Similar to what has been seen in the numerical simulation for a single hydraulic fracture, the peak (maximum) net wellbore pressure ($p_w - \sigma_n$) is reduced as n drops from 200 to 20, especially when the fluid viscosity is smaller. However, this effect is diminished with increasing fluid viscosity.

So far all results have been essentially as expected. However, the behavior becomes more surprising when we reduce the spacing between the initial cracks to $\Delta Z = 5\,\mathrm{m}$ and keep every other parameter to be the same: $\sigma_n = 30\,\mathrm{MPa}$; $E' = 16.5\,\mathrm{GPa}$; $K_{\mathrm{IC}} = 1.8\,\mathrm{MPa}\sqrt{\mathrm{m}}$; $\mu = 0.001\,\mathrm{Pa}\cdot\mathrm{s}$; $Q_0 = 0.05\,\mathrm{m}^3/\mathrm{s}$; $U = 1.84\times10^{-8}\,\mathrm{m}^3/\mathrm{Pa}$; $a = 6.9\,\mathrm{cm}$; $R_0^I/a = 1/3$. Fig. III.8 shows the evolution of crack radius and influx with time. Strikingly, the two values of subcritical index lead to prediction of totally different behaviors. First, the $n = 200$ case follows the conventional HF model in that the middle fracture (#2) is suppressed by outer fractures and ceases propagation as soon as the radii R of all fractures gain the same order of magnitude as the spacing ΔZ. In contrast, for the results for $n = 20$, although we see the squeezing effect on the growth of fracture 2 early on, after some time period it starts to take more fluid and catch up with the two outer cracks. Finally it takes all fluid injected into the system and outgrows fractures 1 and 3.

More insights can be drawn from Fig. III.9, which plots the ratio of stress intensity factor, $K_{\mathrm{I}}/K_{\mathrm{IC}}$, versus injection time t. It is shown that for the case of a large n, $K_{\mathrm{I}}/K_{\mathrm{IC}}$ converges to a constant value shortly after the fractures start to grow. Note that the same phenomenon was found in the solution for a single hydraulic fracture propagation under subcritical conditions (Lu et al., 2017a). What is striking is that for the three fractures case, a competition in the ratio $K_{\mathrm{I}}/K_{\mathrm{IC}}$ appears to take place between the outer and inner fractures as the fluid influx rate is dynamically partitioned among the hydraulic fractures. It finally leads to the domination of fracture propagation by fracture 2 as the value of $K_{\mathrm{I}}/K_{\mathrm{IC}}$ drops in fracture 1 and 3. Therefore, it is implied by the numerical results that reducing fracture

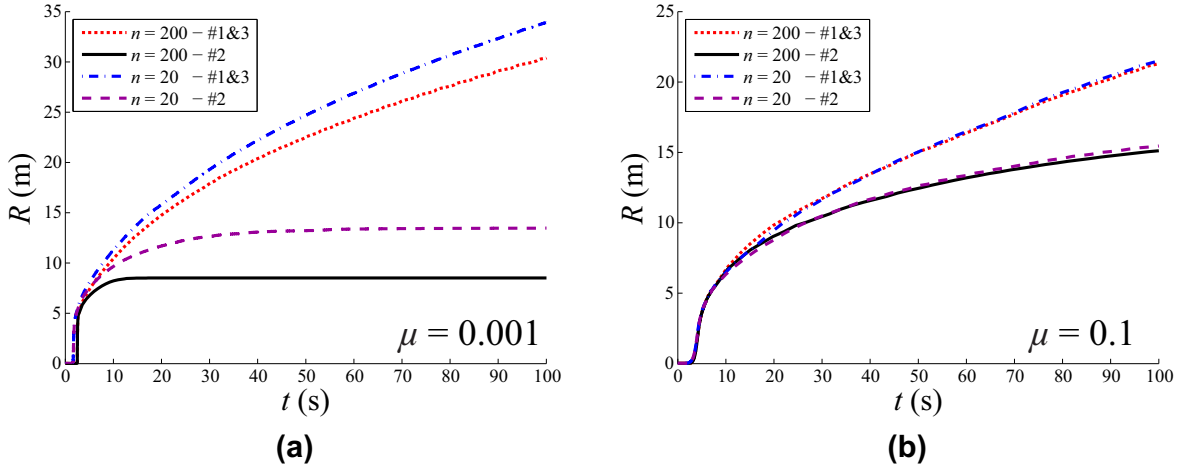

Figure III.6: Evolution of crack radius R_I with injection time t for three evenly placed hydraulic fractures emanating from a horizontal wellbore with $n = 200$ and $n = 20$ injected by fluid with the viscosity of (a) $\mu = 0.001\,\mathrm{Pa}\cdot\mathrm{s}$ ($\mathcal{M} = 0.368$) and (b) $\mu = 0.1\,\mathrm{Pa}\cdot\mathrm{s}$ ($\mathcal{M} = 36.8$).

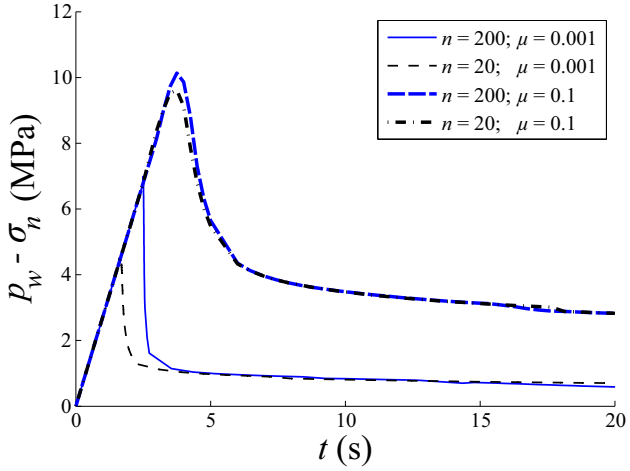

Figure III.7: Net wellbore pressure, $p_w - \sigma_n$, versus injection time t for all four cases of large/small subcritical index n and large/small fluid viscosity μ.

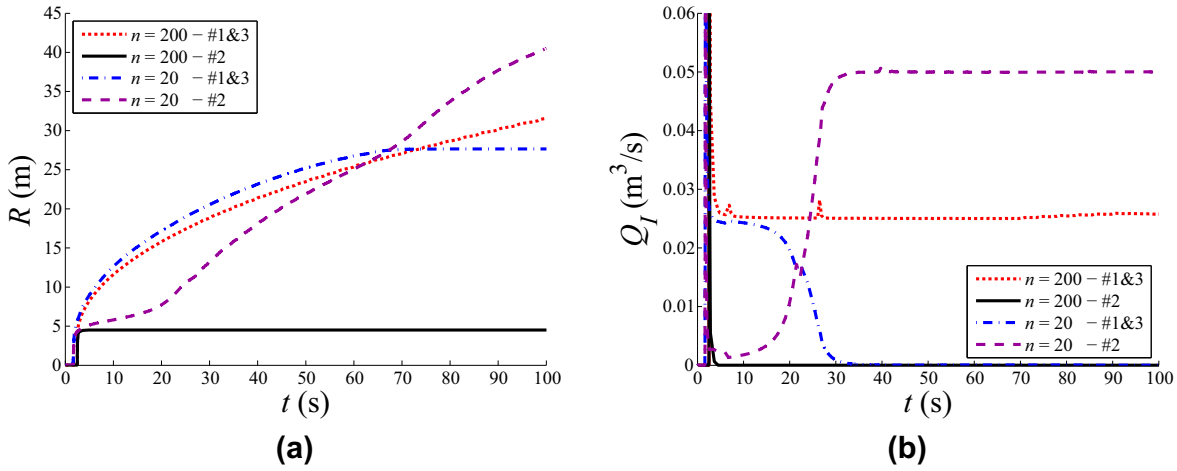

Figure III.8: Evolution of (a) crack radius R_I with injection time t, and (b) fluid influx rate Q_I with injection time t for three evenly placed hydraulic fractures emanating from a horizontal wellbore with $\Delta Z = 5\,\mathrm{m}$ ($n = 200/20$).

seperation, ΔZ, for the case of smaller n, a redistribution of the injected fluid volume into each fracture takes place over time which offsets the effect of stress shadowing.

H. CONCLUSIONS

In multi-stage HF stimulation of horizontal wells, promoting simultaneous growth of all fractures in each stage is important in order to reduce the number of non-producing perforation clusters. Understanding and modeling the basic physical processes of multiple hydraulic fractures is therefore vital to accurate predictions and development of new approaches. The main contribution of this paper is to show that subcritical crack growth plays an important role in the growth of multiple hydraulic fractures. This main conclusion is drawn based on results from a newly presented HF model accounting for simultaneous initiation and propagation of multiple hydraulic fractures from a horizontal wellbore with a subcritical growth prop-

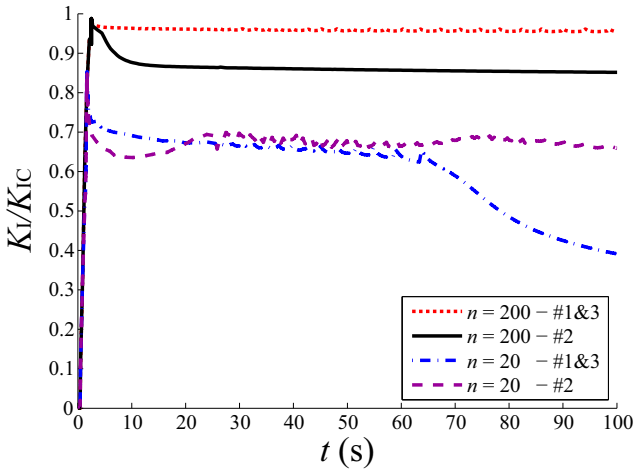

Figure III.9: Dimensionless stress intensity factor κ versus injection time t for the numerical simulation presented in Fig. III.8.

agation condition. Simulation results indicate a substantial influence from the subcritical propagation on both initiation and following growth of multiple hydraulic fractures. Consistent with previous observations, this impact is dependent on the value of the subcritical index n. Specifically, we find that smaller values of n have larger effects on the evolution of both crack radius and wellbore pressure, resulting in earlier initiation, longer fractures, and reduced wellbore peak pressure. As n increases, the results merge to those obtained by the classical LEFM model. Therefore, knowing the correct values of subcritical parameters is crucial to predicting the behavior of multiple hydraulic fractures. Furthermore, the influence of subcritical crack growth vanishes with the increase of the fluid viscosity.

While this previous result is useful for accurate simulation, the impact of subcritical crack growth is shown to be more than just to modify the details of the solution. Rather, in some cases, the behavior associated with multiple hydraulic fracture growth is completely changed. Most notably, for cases with smaller values of subcritical index n, we observe for the first time the existence of a regime in which the central fracture(s) in the array, while initially suppressed, eventually dominate(s) growth thus leading to more uniformity among the fracture sizes. This behavior is observed for smaller values of the subcritical index n

when the separation among the fractures is relatively small, but not in the LEFM cases regardless of separation among the fractures. Hence, our results suggest that reducing the subcritical index can promote multiple hydraulic fracture growth, so that future research aimed at choice of fluid that reduces the subcritical index through chemo-mechanical fluid-rock interaction could lead to more uniform initiation and growth of multiple hydraulic fractures in multi-stage hydraulic fracturing treatment.

IV. TIME-DEPENDENT HYDRAULIC FRACTURE INITIATION: LABORATORY EXPERIMENTS AND NUMERICAL MODELING

A. PREAMBLE

A preprint of Lu et al. (In review) is given in this chapter. Laboratory HF experiments are performed to explore the occurrence of time-dependent HF initiation in three types of rocks. The experimental data shows that delayed HF initiation can be achieved under sustained subcritical wellbore pressures. The results are compared with solutions obtained from the numerical model presented in Chapter II. The importance of the relevant parameters are also examined.

B. ABSTRACT

Time-dependent failure has been proven to occur in various brittle rocks and has a wide range of applications. However, this phenomenon has only recently been considered in studies on hydraulic fracture initiation. Laboratory delayed hydraulic fracturing breakdown experiments have been carried out on three rocks (granite, sandstone, and limestone) under sustained subcritical wellbore pressures to study the occurrence of time-dependent initiation. Test results were then used to benchmark a numerical model that takes into account a subcritical crack growth law to predict the time duration to breakdown. We show that this numerical model is useful in various aspects, such as estimating the value of the subcritical index n based on characterization experiments, and given characterization data, predicting the time duration to breakdown under certain pressurization and loading conditions.

The comparisons between predictions and experimental results highlight both the ability of the model to predict the delay time and also the difficulties associated with the apparent dependence of the subcritical index n on the fluid-rock system and the confining stress state.

C. INTRODUCTION

Multi-stage hydraulic fracturing (HF) is one of the most important techniques for stimulation of oil and gas production from unconventional hydrocarbon reservoirs. The goal is to maximize the oil/gas production and to reduce developing costs compared to other stimulation options. With this technology, as the name implies, the well is stimulated in stages. In each stage, multiple hydraulic fractures (typically 3 to 8) are initiated and propagated simultaneously by a continuous pumping operation into an isolated section of the well. Although it has been proven to be a successful technology that can boost the effectiveness of the well stimulation, production logs from more than 100 shale wells show that up to 30% of the perforation clusters - the entry points intended to be stimulated by each growing hydraulic fracture - do not contribute to production (Miller et al., 2011), and one of the main reasons for the non-productive clusters is that a certain portion of the clusters fail to be stimulated. Thus, models that enable prediction and lead to new approaches to increase the number of stimulated perforation clusters can play an important role in the design of multi-stage HF treatments.

To address the problem of multiple HF growth, it is crucial to accurately predict the initiation of each fracture because initiation is the pre-requisite of multiple fracture growth. Over the past few decades, efforts have been made to study the parameters that influence the initiation and early growth of single/multiple hydraulic fracture(s) (Abbas and Lecampion, 2013; Abbas et al., 2013; Bunger et al., 2010; Detournay and Carbonell, 1997; Haimson and Fairhurst, 1967; Hubbert and Willis, 1957; Lakirouhani et al., 2016; Lecampion and Desroches, 2015). While the effect of various factors (e.g., borehole radius, compressibility, in-situ stresses, and fluid viscosity) on HF initiation has been investigated in several prior studies, a long recognized but often ignored characteristic of rock, namely, time-dependent

breakage and/or subcritical crack growth, has only recently been considered. Conventional approaches to solve the HF problem assume no fracture initiation before some critical condition is met. Such critical conditions include a requirement that the maximum induced tensile stress meets or exceeds the tensile strength of the rock (Haimson and Fairhurst, 1967; Hubbert and Willis, 1957), that the Mode I stress intensity factor equals the fracture toughness of the rock (Abbas and Lecampion, 2013; Bunger et al., 2010; Detournay and Carbonell, 1997; Lakirouhani et al., 2016; Lecampion and Desroches, 2015), or the crack is able to propagate through satisfaction of a traction-separation failure condition applied to a cohesive zone at the leading edge (Lecampion, 2012b). However, numerous studies show that rocks can be caused to fail after a period of time when subjected to stresses that are insufficient to satisfy a critical instantaneous failure criterion (Atkinson, 1984; Fernau et al., 2016; Kear and Bunger, 2014; Lu et al., 2015; Scholz, 1972). Furthermore, laboratory HF experiments on granite (Lu et al., 2015) have shown that a wellbore pressure that is lower than the critical value required for instantaneous HF initiation can lead to breakdown in a delayed manner. This phenomenon, referred to as time-dependent HF initiation, is argued by Bunger and Lu (2015) as one of the fundamental mechanisms for simultaneous generation of multiple hydraulic fractures, with the potential to significantly impact the propagation of the fractures, especially in an early stage of the HF growth (Lu et al., 2017a).

Lu et al. (2017a) propose that time-dependent HF initiation can be attributed to growth of the fracture under subcritical hydraulic pressures that induce a smaller Mode I (opening mode) stress intensity factor, K_{I}, compared to the fracture toughness, K_{IC}. Under such subcritical conditions, the fracture tip velocity, V, is related to the ratio of $K_{\mathrm{I}}/K_{\mathrm{IC}}$ by a power law correlation called the subcritical crack growth law (Atkinson, 1984; Charles, 1958)

$$V = A\left(\frac{K_{\mathrm{I}}}{K_{\mathrm{IC}}}\right)^{n} \tag{IV.1}$$

where the empirical parameter n is the subcritical crack growth index and A is a constant characteristic velocity typically taken on the order of the Rayleigh wave speed, i.e., an upper bound on the growth velocity when $K_{\mathrm{I}} \to K_{\mathrm{IC}}$. Unlike the classical theory of Linear Elastic Fracture Mechanics (LEFM), which imposes that the fractures do not initiate before the

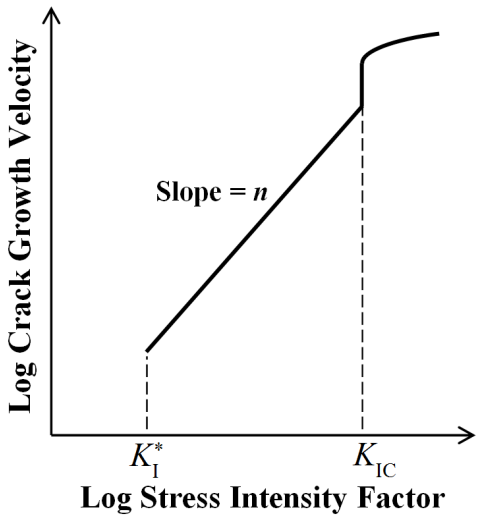

Figure IV.1: Log-log plot of the crack tip velocity and the stress intensity factor (after Atkinson, 1984; Olson, 1993).

propagation criterion is reached (i.e., K_I=K_{IC}), the subcritical crack growth law states that a crack in a stressed material under subcritical loading conditions can grow with a finite velocity that is strongly dependent on the subcritical index. This parameter, n, can be measured in a laboratory using the Double Torsion (DT) experiments (Evans, 1972; Holder et al., 2001; Williams and Evans, 1973). After the crack reaches a critical size such that the failure criterion is satisfied (K_I=K_{IC}), the growth rate of the crack tip attains the rupture velocity of the material, which leads to a rapid (essentially instantaneous) failure. Fig. IV.1 shows the typical evolution of the crack tip velocity with the stress intensity factor (after Atkinson, 1984; Olson, 1993). The subcritical crack growth law has been proven to be well defined for a wide range of natural rock formations and to have a profound effect on the development of natural fracture sets (Gale et al., 2007; Olson, 1993, 2004).

Our recent work demonstrated delayed initiation of HF in granite (Lu et al., 2015) and limestone (Lu et al., 2017b), as well as developed a new HF simulator accounting for subcritical growth (Lu et al., 2017a). This paper brings together new experimental results with

our prior data, and uses this data to benchmark and guide refinement of the simulator. Hence, this work explores the occurrence of time-dependent HF initiation under laboratory conditions and, via coupled simulations, ties this phenomenon to subcritical crack growth. We first present our experimental results from the laboratory time-dependent HF initiation experiments on granite, sandstone, and limestone specimens. Then, by comparing the experimental data with numerical predictions obtained from the subcritical crack growth model modified from Lu et al. (2017a), the underlying mechanisms of delayed initiation are investigated, including the influence of fluid viscosity and the confining stresses.

D. LABORATORY DELAYED HF BREAKDOWN EXPERIMENTS

Inspired by the evidence of the time-dependent failure exhibited by rocks, laboratory HF experiments were conducted under sustained subcritical wellbore pressures lower than the pre-determined instantaneous breakdown pressure. Three types of rocks were tested: Coldspring Charcoal Granite, Agra Red Sandstone, and Kasota Valley Limestone. For each rock, two sets of experiments were performed under different test conditions in order to explore the impact of fluid viscosity and the applied confining stresses on the relationship between the wellbore pressure and the time to breakdown. The testing program is summarized in Fig. IV.2, and the testing conditions are detailed in Section IV.D.2 (see also Table IV.2). The experimental data presented in this paper includes results from previous HF experiments on granite using glycerin (Lu et al., 2015), and on sandstone specimens using water and varying confining stresses (Uwaifo, 2016), as well as recent HF tests on granite and limestone under various fluid and stress conditions.

1. Sample preparation

The experiments are carried out by pressurizing a 50-mm-long open section in a 12.5-mm-diameter wellbore in the center of a 150-mm cubic specimen. Fig. IV.2 contains a sketch of the experimental setup and a photograph of a specimen after a hydraulic fracture has

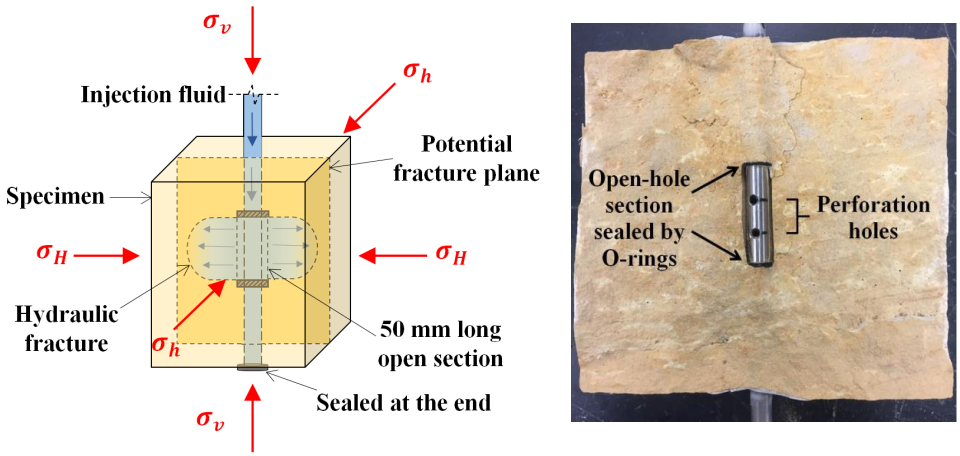

Figure IV.2: Sketch of the experimental setup (left) and a photograph showing the cross section of a limestone specimen after failure (right).

occurred. The rocks are supplied by the quarry and pre-cut into 150 × 150 × 150 mm blocks. A 12.5-mm-diameter hole was drilled throughout the center of each sample. Then the injection tube, a 150-mm stainless steel tube with two pairs of perforation holes was placed inside the borehole. Finally, a 50-mm-long open-hole region was made by sealing both sides of the central section in the borehole using O-rings and strong epoxy adhesive, as detailed in Fig. IV.2.

Mechanical properties for each type of rock were measured using standard laboratory methods. These are listed in Table IV.1. Besides these properties, the subcritical crack growth index, n, is also measured for granite in the double torsion experiments. These tests indicate a range: $9 \leqslant n \leqslant 27$.

2. Experimental method

In all experiments, the open-hole section was filled with fluid and subjected to a constant pressure using a syringe pump. The wellbore pressure was thus generated and maintained as a constant by adjusting the rate of injecting fluid into the sample with a feedback loop control. Of course this is not the typical boundary condition for HF in the field; typically

Table IV.1: Material properties of the rocks.

Material property	Granite	Sandstone	Limestone	Test Method
Young's Modulus (GPa)	37	22	45	Uniaxial compression on cylindrical specimens (ASTM, 2010a)
Poisson's Ratio	0.27	0.38	0.3	Uniaxial compression on cylindrical specimens (ASTM, 2010b)
Fracture toughness (MPa$\sqrt{\text{m}}$)	1.5	0.48	0.77	Three-point loading on semicircular bend (SCB) specimens (Kuruppu et al., 2014)

fluid is injected at a fixed rate, not pressure. However, for the purpose of investigating the relationship between subcritical wellbore pressure and time to failure, constant pressure is ideal. Additionally, confining stresses (σ_v, σ_H and σ_h, see Fig. IV.2) were applied using a custom-built ENERPAC true tri-axial load frame. Flat loading plates are placed on all surfaces of the specimen to ensure evenly distributed confining stresses in all three directions. The first tests in each rock type were carried out to determine the wellbore pressure that causes instantaneous breakdown. Then the delayed HF breakdown tests were run under sustained subcritical wellbore pressures, smaller than the instantaneous breakdown pressure. For each test, the specimen lifetime, defined as the duration from when the target pressure is achieved to the moment of failure, was recorded. Finally, the relation of lifetime (time of breakdown) versus wellbore pressure was determined by completing a series of experiments under different wellbore pressures. Table IV.2 summarizes the experimental conditions for all series of tests. To study the impact of the fluid viscosity, we selected water and glycerin as the two types of injection fluids to be used on granite under zero confining stresses. For

the sandstone and limestone experiments, our interests were to examine the influence of different stress conditions; hence, water was used as the fracturing fluid in all sandstone and limestone cases.

3. Experimental results

The experimental results are shown in Fig. IV.3. Two sets of data points are plotted in each figure, representing tests under different experimental (fluid or stress) conditions. The test data leads to several observations. Firstly, our results confirm the occurrence of delayed HF breakdown in granite, sandstone, and limestone. In all cases, we find consistent correlations between the time of breakdown and the wellbore pressure, indicating an underlying mechanism that governs the initiation and subsequent growth of hydraulic fractures under subcritical wellbore pressures. Secondly, the presence of time-dependent HF breakdown under various conditions, such as different fluid viscosities (see the two cases in granite tests) and confining stresses (sandstone and limestone experiments), is also confirmed by the experiments. Specifically, these results indicate that the time delay is increased for cases with higher viscosity. The effect is substantial. For example, in granite, 16 MPa wellbore pressure with water leads to nearly instantaneous breakdown, while the same pressurization with glycerin leads to a delay time of more than 1000 seconds.

The impact of the applied confining stresses is also strong, exhibiting an overall shift of the lifetime versus pressure relation in both the sandstone and limestone results. Here the shift in pressure associated with a given delay time is expected based on the impact of the applied stresses on the near wellbore stress concentration. That is to say, for a given delay time, the shift in wellbore pressure required for that delay time is predictable based on the contribution of the confining stresses on the near wellbore tangential stress. According to the well-known Kirsch solution (Kirsch, 1898), which is the basis of past breakdown models (Bunger and Lu, 2015; Haimson and Fairhurst, 1967; Hubbert and Willis, 1957), the shift in pressure associated with a given delay time, Δp, is predicted to be

$$\Delta p = 3\sigma_h - \sigma_H \tag{IV.2}$$

Table IV.2: Fluid and stress conditions for the experiments. The confining stresses in all three directions for cases of unconfined tests are taken as the value of the atmospheric pressure.

Experimental condition		Injection fluid	Confining stresses
Granite	Case I	Water ($\mu = 0.001$ Pa $\cdot$ s)	Atmospheric pressure: $\sigma_v = 0.1$ MPa $\sigma_H = 0.1$ MPa $\sigma_h = 0.1$ MPa
	Case II	Glycerin ($\mu = 1.08$ Pa $\cdot$ s)	Atmospheric pressure: $\sigma_v = 0.1$ MPa $\sigma_H = 0.1$ MPa $\sigma_h = 0.1$ MPa
Sandstone	Case I	Water ($\mu = 0.001$ Pa $\cdot$ s)	Atmospheric pressure: $\sigma_v = 0.1$ MPa $\sigma_H = 0.1$ MPa $\sigma_h = 0.1$ MPa
	Case II	Water ($\mu = 0.001$ Pa $\cdot$ s)	Tri-axial stresses: $\sigma_v = 3$ MPa $\sigma_H = 2$ MPa $\sigma_h = 1$ MPa
Limestone	Case I	Water ($\mu = 0.001$ Pa $\cdot$ s)	Atmospheric pressure: $\sigma_v = 0.1$ MPa $\sigma_H = 0.1$ MPa $\sigma_h = 0.1$ MPa
	Case II	Water ($\mu = 0.001$ Pa $\cdot$ s)	Tri-axial stresses: $\sigma_v = 6$ MPa $\sigma_H = 6$ MPa $\sigma_h = 4$ MPa

Hence, for the sandstone cases, the predicted $\Delta p = 1$ MPa, while we observe a shift that is somewhat larger (1.5 - 2 MPa). The predicted shift for the limestone cases is $\Delta p = 6$ MPa, which is reasonably consistent with the experimental data (5 - 5.5 MPa).

In spite of this consistency for the limestone case, it remains to determine the reason for the dependence on viscosity as well as the larger than expected shift in pressure with applied stresses for sandstone. Note that, we keep the same wellbore radius throughout all experiments to eliminate the size effect that can cause the discrepancy in the strength. It is possible to speculate that reasons could be tied to a transition from fully penetrating fluid for water to fully non-penetrating fluid for glycerin. As pointed out by Detournay and Carbonell (1997), this transition reconciles the models of Hubbert and Willis (1957) and Haimson and Fairhurst (1967), corresponding to limits wherein the fluid does not penetrate and fully penetrates the flaw(s) that comprise the initiation points for fracture growth, respectively. But to move beyond speculation requires a model. Similar to Detournay and Carbonell (1997), it is desirable to introduce a finite initial crack that will enable modeling of fluid penetration. However, the time-dependent behavior exhibited in the experiments can hardly be explained by the conventional LEFM theory, since the insufficient induced K_{I} (i.e., $K_{\mathrm{I}} < K_{\mathrm{IC}}$) would not lead to the HF initiation. We propose that, under these circumstances, the crack can still initiate and grow with a velocity following the subcritical crack growth theory expressed in Eq. (IV.1). A numerical model based on this proposition is developed in **?**, and the experimental results presented here will be used to examine the validity of this model and guide its further refinement.

E. MATHEMATICAL MODEL

1. Problem formulation

The numerical results presented in this paper are calculated using the subcritical crack growth HF model developed by Lu et al. (2017a), with a few alterations that are detailed here. We consider the problem of time-dependent initiation and propagation of a single hy-

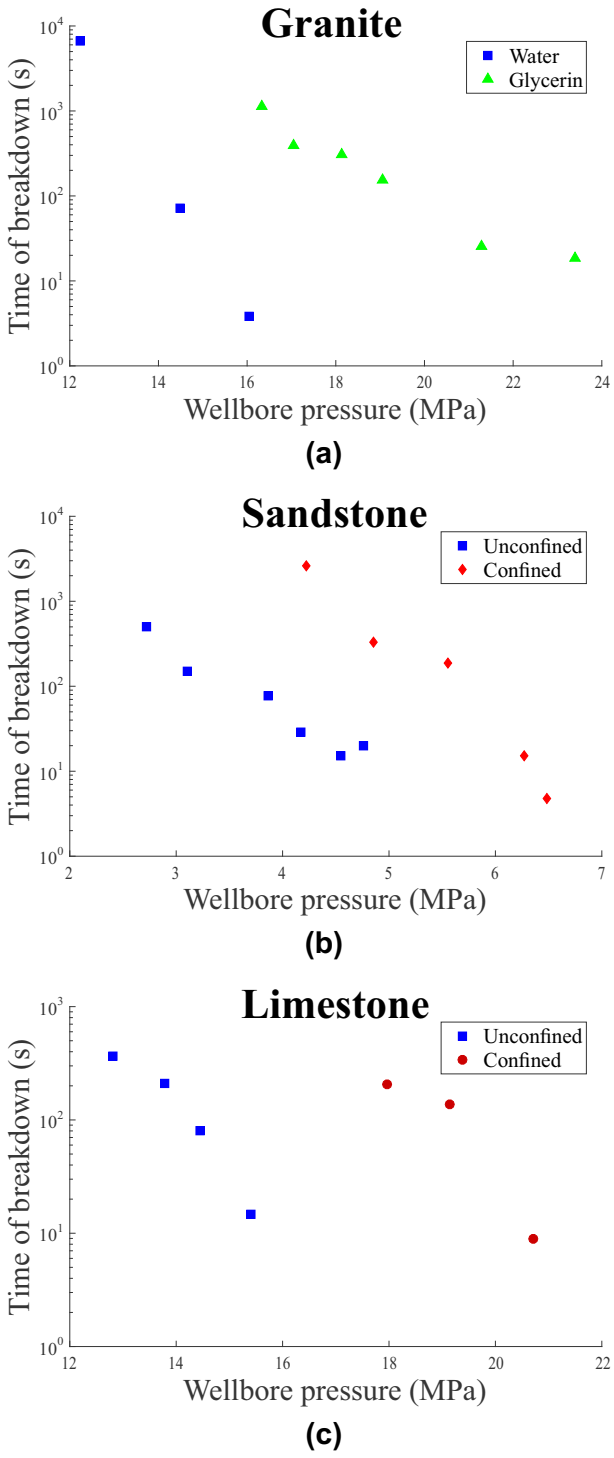

Figure IV.3: Experimental results for (a) granite, (b) sandstone, and (c) limestone.

draulic fracture in an impermeable, linearly elastic rock characterized by Young's modulus E, Poisson's ratio ν, and fracture toughness K_{IC}. A Newtonian fluid with viscosity μ is injected into the wellbore under a constant wellbore pressure p_w. This is the first variation from **?**, which imposes constant rate injection to a compressible wellbore system. The hydraulic fracture is assumed to be a longitudinal bi-wing planar fracture under plane strain conditions with an initial length l_0 emanating from a vertical wellbore with the radius a under the minimum and maximum (or intermediate) in-situ stresses (see Fig. IV.4). The fluid lag and the fluid leak-off are both assumed to be negligible. Although this numerical model is built on prior works related to the numerical simulations of single HF process (Bunger et al., 2010; Detournay and Carbonell, 1997; Lakirouhani et al., 2016), the main novelty in our model is that the propagation of the hydraulic fracture is now governed by the subcritical crack growth law, Eq. (IV.1). Thus, stable HF growth is allowed at wellbore pressures that are insufficient to satisfy $K_{\mathrm{I}} = K_{\mathrm{IC}}$, the critical LEFM criterion. Hence, HF growth is expected to proceed in a stable manner for a while but, after a certain time, the crack propagation will attain a critical condition leading to overall failure of the specimen. It is worthwhile to note that, the initially subcritical stress intensity factor K_{I} increases as the crack grows, and it is physically reasonable to consider HF breakdown as the time it takes to attain $K_{\mathrm{I}} = K_{\mathrm{IC}}$. However, due to the limitation of the specimen size, we impose a second criterion for breakdown of the laboratory specimens. This criterion is that as soon as the crack grows to the boundary of the block, the specimen is assumed to lose its integrity and fail. Hence, HF breakdown is alternatively defined as the moment when the fracture length $l(t)$ gains the value of half of the specimen size (i.e., the distance to the edge of the specimen from the central wellbore). In summary, for the specimen pressurized at a constant wellbore pressure, p_w, we seek the solution for the time of breakdown, t_f, which is the smaller of the two values of time required to achieve: a) $K_{\mathrm{I}} = K_{\mathrm{IC}}$, or b) a hydraulic fracture length corresponding to half of the specimen size.

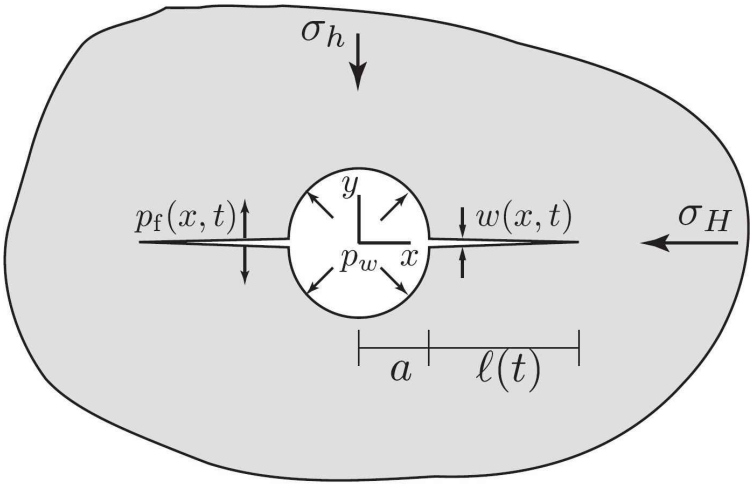

Figure IV.4: Plane strain model of a longitudinal hydraulic fracture from a wellbore drilled in the direction of intermediate (or maximum) in-situ stress (after Bunger et al., 2010; Lakirouhani et al., 2016).

2. Governing equations

For the bi-wing fracture emanating from a circular wellbore under plane strain conditions, the displacement discontinuity (DD) formulation, given by Crouch (1976) and Crouch and Starfield (1983), is used. The wellbore contour and the fracture are discretized into a total of N straight line segments (elements) with mid-points denoted $s_i,\ i = 1, ..., N$. The relationships between the fluid pressure, the displacement jump in the fracture and the (fictitious) displacement jump on the wellbore are given by

$$\begin{aligned} \sigma_n(s_i) - p_f(s_i) &= \sum_{j=1}^{N} (A_{ns})_{ij} [u_s^j] + \sum_{j=1}^{N} (A_{nn})_{ij} [u_n^j] \\ 0 &= \sum_{j=1}^{N} (A_{ss})_{ij} [u_s^j] + \sum_{j=1}^{N} (A_{sn})_{ij} [u_n^j] \end{aligned} \tag{IV.3}$$

where the influence coefficients $(A)_{ij}$ represent the stresses (normal or tangential) at s_i caused by a unit uniform displacement jump (normal or tangential) across the element j, and their expressions can be found from Eqs. (28) - (30) of Crouch (1976). Here $[u_n^j]$ is defined as the normal displacement jump across the element j (equal to the crack width w along the crack),

and $[u_s^j]$ denotes the tangential displacement jump across the element j. In Eq. (IV.3), for points s_i on the fracture, σ_n is the normal compressive stress along the direction of fracture propagation, the x-axis, due to the in-situ stresses, given by (Kirsch, 1898)

$$\sigma_n(x) = \sigma_h \left(1 + \frac{a^2}{x^2}\right) + \frac{\sigma_H - \sigma_h}{2} \left(\frac{a^2}{x^2} - 3\frac{a^4}{x^4}\right) \tag{IV.4}$$

For points s_i on the wellbore, $\sigma_n(s_i) = 0$, and the fluid pressure $p_f(s_i)$ is equal to the wellbore pressure ($p_f(s_i) = p_w$). Moving on to the fluid flow model, the Poiseuille law governs the fluid flux $q(x,t)$ in the fracture, defined as $q = w < v >$, where $< v >$ is the mean fluid velocity across the fracture opening, as

$$q = -\frac{w^3}{\mu'} \frac{\partial p_f}{\partial x} \quad \text{for} \quad x \in (x_0, x_{tip}) \tag{IV.5}$$

Here $\mu' = 12\mu$ for the dynamic viscosity μ, and $x_0 = a$ and $x_{tip} = a + l$ denote the locations of the wellbore wall and the fracture tip, respectively. This flow law combines with the local continuity equation which is derived based on mass balance for an incompressible fluid, given by

$$\frac{\partial w}{\partial t} + \frac{\partial q}{\partial x} = 0 \tag{IV.6}$$

To solve the solid-fluid coupled problem, additional boundary and initial conditions are needed. The initial condition is chosen as the pressure distribution p_f generating a small, uniform, positive net pressure acting along the interior faces of the initial crack, that is

$$t = 0: \quad p_f(x,t) = \sigma_n(x) + p_i, \;\; l = l_0 \quad (x_0 < x < x_0 + l_0) \tag{IV.7}$$

where p_i is a small initial net pressure assumed to exist in the crack, and l_0 is the initial fracture length. In the experiment, a sustained wellbore pressure, P, is distributed uniformly on the wellbore wall, which gives the inlet boundary condition

$$p_w = P \cdot H(t) \tag{IV.8}$$

where $H(t)$ is the Heaviside unit step function. The crack-tip boundary condition imposes vanishing fluid flux and fracture width at the fracture tip

$$x = x_{tip}: \quad w(x,t) = 0, \quad q(x,t) = 0 \tag{IV.9}$$

Finally, the subcritical tip asymptote, derived from the LEFM tip asymptote (Irwin, 1957) and the subcritical crack growth law Eq. (IV.1), defines the growth rate for $K_{\mathrm{I}} < K_{\mathrm{IC}}$ (Lu et al., 2017a)

$$w \sim \sqrt{\frac{32}{\pi}} \frac{K_{\mathrm{IC}}}{E'} (x_{tip} - x)^{1/2} \cdot \left(\frac{V}{A}\right)^{1/n}, \quad x \to x_{tip} \tag{IV.10}$$

where $E' = E/(1-\nu^2)$ is the plane strain elastic modulus. Consequently, the propagation condition gains dependence on a laboratory-determined parameter n, as well as an additional coupling with the global solution for the HF growth via the propagation velocity V.

3. Numerical algorithm

The numerical solution for the problem is obtained based on the DD method for solving the elasticity eqyatuibs coupled with a finite volume solution for fluid flow, and an implicit length stepping algorithm. The discretized elasticity equation (IV.3) is formulated for a fixed grid of DD elements with a constant element size, and a 1D finite volume scheme is applied for discretizing Eq. (IV.6). Then the combined nonlinear system, resulting from the solid-fluid coupling, is solved by an iterative scheme. As the fracture propagates, the fracture length is increased by a constant value and the corresponding time step required to increase the crack length by this increment is found as a part of the numerical solution. This length-controlled implicit algorithm is discussed in detail in Lu et al. (2017a).

4. Roughness correction for the fracture toughness

The model presented up to this point is complete and able to provide prediction of time to breakdown as a function of wellbore pressure, far-field stress, fluid viscosity, injection rate, and rock properties. However, as is shown in Appendix C.B, the model is insufficient

to explain the impact of the viscosity on the time to breakdown, underestimating time to breakdown for higher viscosity fluid by several orders of magnitude. Also, the predicted impact of the stresses will be shown to be weaker than observed in the experiments. We find, through the comparisons detailed in Appendix C.B, that matching the large viscosity and large pressure cases entails essentially using a larger value of the rock fracture toughness.

Driven by these observations, we introduce another refinement to the model. According to Garagash (2015), in the vicinity of the fracture tip, the aperture roughness may have a significant influence on the energy dissipation during fluid-driven fracturing in comparison to that predicted by the conventional LEFM-based model. To take into account the effect of viscous fluid flow in the rough fracture tip, the additional energy dissipation will be included in the context of the classical LEFM as an âeffective fracture toughnessâ. Here we make use of the energy release rate associated with viscous flow in a rough process zone ahead of the crack tip ("roughness correction"), that is (Garagash, 2015)

$$G_{rough} = 0.778 \left(|\sigma_0| E' \mu' V w_c^2\right)^{1/3} \tag{IV.11}$$

Here $\sigma_0 = \sigma_n(x_{tip})$ denotes the net stress induced by the surrounding rock formation (i.e., in-situ stresses) at the crack tip and w_c denotes the characteristic scale of the rough aperture, which is taken with an order of magnitude of 10^{-3} m. Note that for the case of zero confining stress in the laboratory, σ_0 is taken to be the atmospheric pressure due to the existence of vacuum at the region very close to the crack tip. Next, the total energy release rate is given by

$$G_{total} = G_{classical} + G_{rough} \tag{IV.12}$$

where $G_{classical} = K_{\mathrm{IC}}^2/E'$ represents the energy release rate in the classical LEFM (Irwin, 1957). Finally, the effective fracture toughness can be written as

$$K_{\mathrm{IC}}^{eff} = \sqrt{G_{total} \cdot E'} \tag{IV.13}$$

Following the spirit of Garagash (2015), the fracture toughness acquired in laboratory experiments, K_{IC}, is now replaced by the effective fracture toughness, K_{IC}^{eff}, to account for the

roughness effect on the HF growth. Substituting Eqs. (IV.11) – (IV.13) into Eq. (IV.10), the subcritical tip asymptotic solution is rewritten as

$$w \sim \sqrt{\frac{32}{\pi}} \frac{1}{E'} \sqrt{\left[K_{\mathrm{IC}}^2 + 0.778 \left(|\sigma_0| E'^4 \mu' V w_c^2\right)^{1/3}\right] (x_{tip} - x)} \cdot \left(\frac{V}{A}\right)^{1/n}, \quad x \to x_{tip} \tag{IV.14}$$

F. NUMERICAL RESULTS

To run the numerical simulation, the first step is to determine the values of all relevant parameters in the model. The material properties of the rocks, i.e., the fracture toughness, Young's modulus, and Poisson's ratio are provided in Table IV.1. Table IV.2 gives the applied horizontal in-situ stresses (σ_H and σ_h) and the fluid viscosities, and the wellbore radius is taken to be the same as in the experiments ($a = 6.25$ mm). These are all independently measured. The roughness aperture, w_c, cannot be definitively measured in laboratory tests. We set it to be 1 mm according to observation of the order of magnitude of the largest scale of roughness in the fractures created in these rocks. Moreover, it is implied by Eq. (IV.1) that as the value of K_{I} approaches K_{IC}, the crack tip velocity should in principal recover the rupture velocity of the material. Therefore, A is set to be 1000 m/s as the constant in Eq. (IV.1), thus capturing the order of the expected rupture velocity in rocks (Rosakis et al., 1999). Then, the remaining unknowns include the subcritical growth parameter n and the initial crack length l_0. In these experiments, no artificial flaw/notch was created on the wellbore to serve as an initial crack. Hence, without knowing the exact value of l_0, it is reasonable to assume that the initial crack is on the order of the pore size of the rocks, which is around 0.1 mm. In what follows, we will show how we determine the value of the subcritical index n using the experimental results for tests using water injection under zero confinement. With this in mind, the values of l_0 and subcritical index n are chosen to match the slope of the time delay versus wellbore pressure for the unconfined, water injection cases for each rock type.

After these characterization experiments, we employ the model to predict the delay time with larger values of viscosity and/or confining stresses, showing both the ability of the model

to predict the delay time and also the difficulties associated with apparent dependence of the subcritical index n on the fluid-rock system and the confining stress state.

1. Determination of the subcritical crack growth index

The tests with water injection and zero confining stresses are carried out as characterization experiments to obtain the value of subcritical index n and initial flaw length l_0 for all three rocks. Taking granite as an example, by implementing a few simulations with different n and l_0 values, we found that the case of $l_0 = 110\,\mu$m, and $n = 25$ generates a pressure versus lifetime correlation that is most consistent with the experimental data (Fig. IV.5a, blue dashed curve). By comparing the solution with those from $n = 23$ and $n = 27$, we also show that the numerical solution strongly depends on the value of n that a small change in n would lead to a totally different pressure-lifetime relation. Thus, it is concluded that a suitable value of the subcritical index can be determined by comparing the results from our numerical model with the experimental data. As another verification, this value of subcritical index, $n = 25$, falls into the range of the laboratory measurement for n in granite by DT experiments ($9 \leqslant n \leqslant 27$, see Appendix C.A).

Similarly, the values of n for sandstone and limestone are obtained from unconfined water injection experiments. In this way, we find $n = 16$ for sandstone and $n = 45$ for limestone, with $l_0 = 80\,\mu$m for both rocks. It is worth noting that, although l_0 is used as a fitting parameter in the simulation, its value varies little from one rock to another (from 110 μm for granite to 80 μm for sandstone and limestone).

2. Predicting the time-dependent behavior under various test conditions

Subcritical index is challenging to characterize, and so one useful outcome of the experiment-model comparisons is a new approach to estimate its value. Besides estimation of the subcritical index n and flaw size l_0, we will further show that given these values, the numerical model is able to predict time to breakdown versus pressure including its dependence upon the fluid viscosity and the applied stresses.

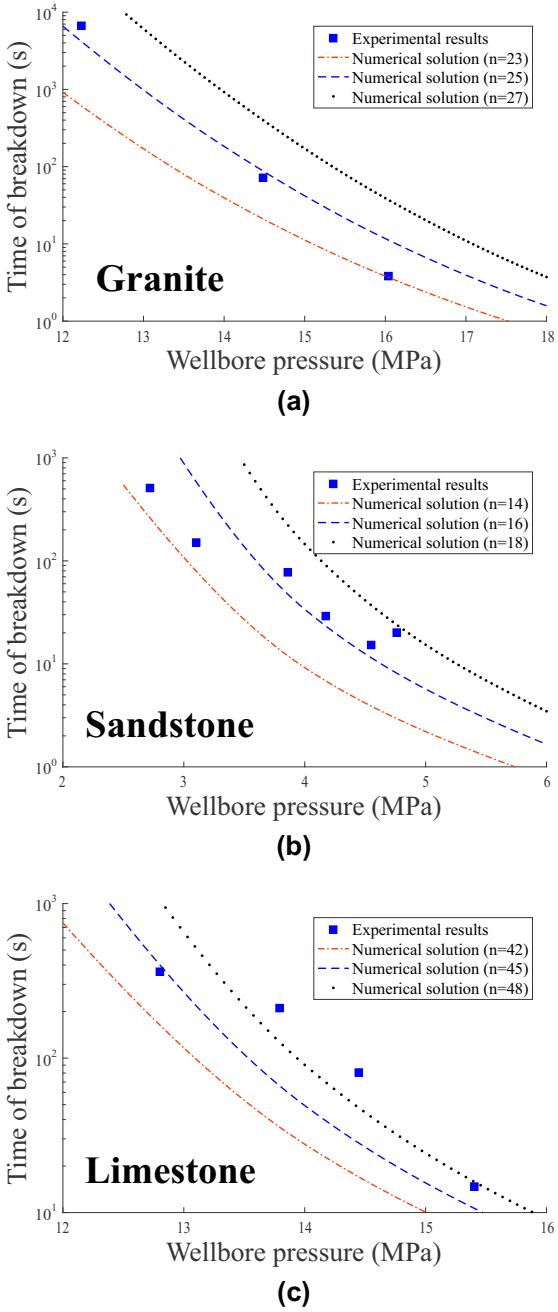

Figure IV.5: Comparison of the experimental data from (a) granite, (b) sandstone, and (c) limestone (under the water injection and zero confinement condition) with the numerical solution calculated for cases with different values of n. In the simulations, l_0 is 110 μm for granite, and 80 μm for sandstone and limestone.

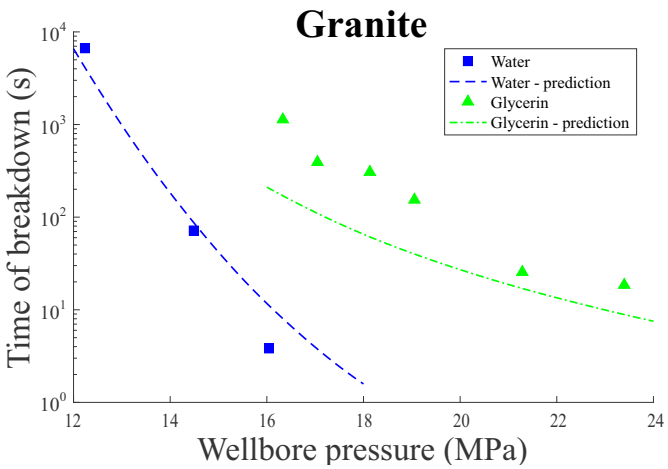

Figure IV.6: Numerical prediction of time-dependent breakdown for granite injected by glycerin ($n = 25$, $l_0 = 110\,\mu$m). Results are compared with the test data, together with experimental and numerical results of the water injection case.

Using the values of n and l_0 acquired in Section IV.F.1 for granite, we now simulate the tests using glycerin as the fluid by changing the fluid viscosity to $\mu = 1.08$ Pa $\cdot$ s. The numerical prediction is plotted with the test results in Fig. IV.6. As shown in the figure, an overall delayed effect of HF breakdown is captured by the model (green curve). The prediction is particularly good for smaller delay times (<100 s), while the prediction underestimates the time of breakdown for larger delay times. We note that the slope is not matched, and simulations show that the slope is almost exclusively controlled by subcritical index n. Hence, the mismatch could indicate that penetration of water in the tip region impacts the value of n. This brings us to a caveat that characterization experiments are likely specific to certain rock-fluid combinations. As such, application of the model to field cases should rely on laboratory characterization of n carried out at comparable confining stress and fluid injection conditions. That said, even in the absence of such ideal characterization, the prediction are suitable for shorter delay times and within a factor of 2 or so for larger delay times. Considering the variation of delay times that spans orders of magnitude, this factor of 2 accuracy may be sufficient for some practical purposes.

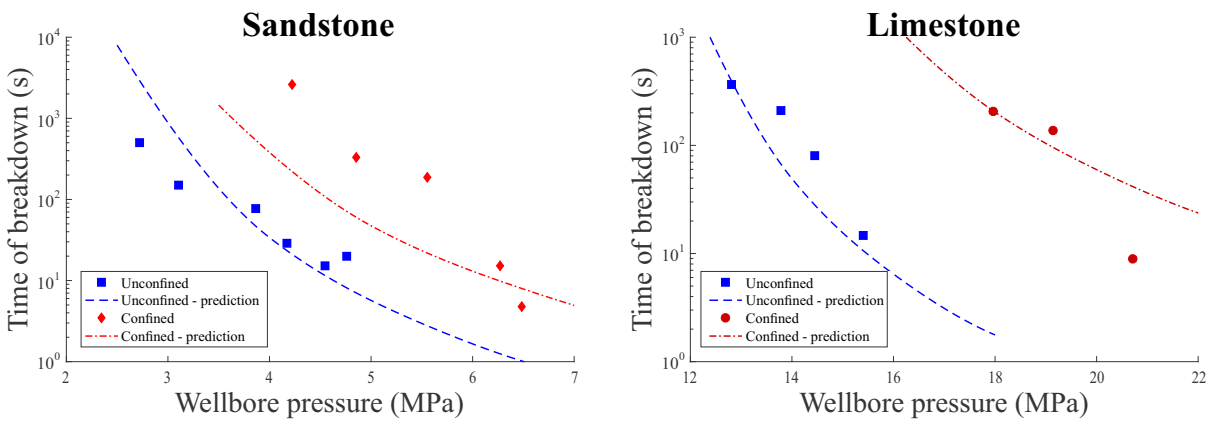

Figure IV.7: Numerical prediction for time of breakdown for sandstone (left) and limestone (right) subjected to confining stresses given in Table IV.2 ($n = 16$, $l_0 = 80\,\mu$m for sandstone and $n = 45$, $l_0 = 80\,\mu$m for limestone). Results are plotted with the test data, and the experimental and numerical results under zero confinement.

We now turn our attention to the effect of confining stresses. Fig. IV.7 presents numerical predictions based on values of n and l_0 determined for sandstone and limestone in Section IV.F.1. The numerical solution is again compared with the experimental data and yields estimated lifetime for the specimen under certain wellbore pressures in the presence of horizontal confining stresses σ_H and σ_h.

The comparison shows that the shift in pressure associated with a given lifetime is reasonably captured, although again the slopes are somewhat different between the numerical and experimental results. These observations, taken together with those for the fluid viscosity effects, point to the possibility that n is impacted not only by the presence of fluid, but also by the ambient stress.

To explore the magnitude of variation of n, we let n to be a fitting parameter. By doing this, we find very good agreement in all cases for granite and sandstone, as shown in Fig. IV.8. For limestone tests, good matches between the experimental data and numerical predictions for the confined tests are found with the same value of n obtained from the unconfined cases ($n = 45$, see Fig. IV.7). Notably, the value of subcritical index n determined using our

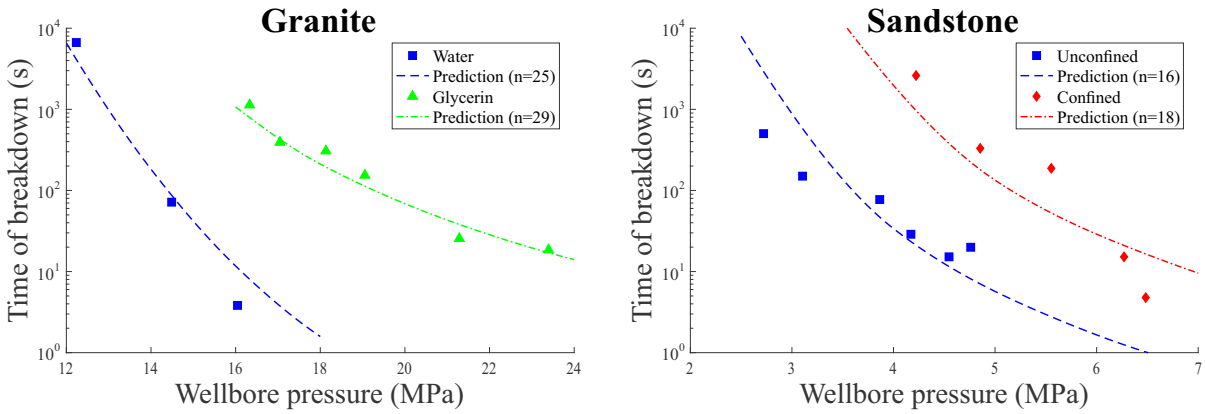

Figure IV.8: Fitting values of subcritical index n to match the numerical solution to test data. For granite experiments (left), best match between the numerical and experiment results for the glycerin case is found using $n = 29$. For sandstone tests (right), solutions of $n = 18$ show good agreement with the data from confined tests.

model for limestone is much larger compared to the other two rocks ($n = 45$ for limestone, compared to $n = 16$ for sandstone and $n = 25$ for granite). Thus, it is implied that the effect of ambient stresses on the subcritical index n is reduced for rocks that have relatively large n.

G. CONCLUSIONS

In this paper, we have shown both the existence and simulation of time-dependent HF breakdown in granite, sandstone and limestone. Our test results and numerical predictions show the wellbore pressure, fluid viscosity, and confining stress substantially affect the time delay associated with subcritical HF initiation. Classical HF models are fundamentally incapable of predicting this delay time. The model presented here brings delay time into the solution by including a subcritical crack growth law enabling HF extension at finite velocities even when the stress intensity factor is much smaller than the fracture toughness of the rock.

While making the model capable of predicting delay time, we observe that this modification is insufficient to explain the magnitude of the impact of changing fluid viscosity. Indeed, through these fully-coupled simulations we find that both our large and small viscosity cases in the laboratory are characterized by the fluid fully penetrating near wellbore flaws. This observation drove a need to consider the role of viscous fluid on resistance to crack growth via its penetration into the tip region. By introducing a previously-proposed roughness-viscosity correction into our model we are able to predict the impact of the viscosity accurately for smaller delay times and within a factor of $2-3$ for larger delay times. The roughness-viscosity correction also provides more accurate prediction of the shift in delay time due to increasing confining stress, which is larger than predicted solely based on the subcritical HF simulator (or on Kirsch's solution).

While the accuracy of the predictions may be sufficient for some cases, the comparisons also point to a potentially important property of the rocks, namely, that the subcritical index apparently depends upon both the fluid being injected and the confining stress state. Hence, if the model is to be used for predictions associated with HF design or interpretation in the field, ideally the subcritical index ought to be characterized through experiments such as the ones presented in this paper using the same rock, fluid, and confining stresses as are expected in the targeted application.

V. CONCLUDING REMARKS

In engineering design for multi-stage HF treatments of horizontal well stimulation, it is ideal to promote simultaneous growth of all fractures in each stage in order to reduce the number of non-producing perforation clusters. Understanding and modeling the basic physical processes governing initiation and growth of multiple hydraulic fractures is therefore vital to effective stimulation of horizontal wells. The main contribution of this thesis is to show that subcritical crack growth plays an important role in hydraulic fracture initiation, growth of single hydraulic fractures, and the complex interaction among multiple hydraulic fractures. This role of subcritical crack growth is firstly demonstrated by developing a numerical model for predicting the initiation and propagation of a single hydraulic fracture from a circular wellbore under the subcritical conditions. The comparison between the results and those obtained from classical LEFM models indicates a significant difference due to the subcritical growth of the hydraulic fracture. In particular, the subcritical index, n has a strong impact on the behavior of the fracture, especially for early time. More specifically, it is shown that smaller values of subcritical index n has larger effect on the evolution of both crack length and wellbore pressure, resulting in an earlier initiation and dropped wellbore peak pressure compared to the LEFM prediction.

Inspired by the striking fact that the growth of a single hydraulic fracture would be totally different once the subcritical crack growth is introduced into the conventional HF model, the numerical model is further extended to the more complicated case of simultaneous initiation and growth of N hydraulic fractures. To achieve this, the numerical algorithm is constructed to account for the stress interference coupled with fluid partitioning into different fractures. Again, substantial difference is found between the subcritical and LEFM solutions in the case of a smaller n, most notably the existence of a regime in which the central fracture(s)

in the array, while initially suppressed, eventually dominates growth thus leading to more uniformity among the fracture sizes. This behavior is observed for smaller values of the subcritical index n when the separation among the fractures is relatively small, but not in the LEFM cases regardless of separation among the fractures.

Finally, the existence of time-dependent HF breakdown in various rocks is shown by laboratory experiments. The delay time of breakdown due to subcritical crack growth is significantly affected by the wellbore pressure, fluid viscosity, and confining stresses. By introducing a roughness-viscosity correction into the numerical model, accurate predictions for lifetime versus wellbore pressure correlation are provided for all cases. Interestingly, a dependence of the subcritical index n on the injected fluid viscosity, as well as the applied confining stresses is implied by the discrepancy between the numerical solutions and the experimental results.

In summary, laboratory experiments show that it is possible to initiate hydraulic fractures with certain time delay by maintaining the subcritical wellbore pressures that are insufficient to induce the instantaneous breakdown. By comparing the experimental results with the numerical predictions, this phenomenon is shown to be tied to the theory of subcritical crack growth. Therefore, this research highlights the importance of the subcritical crack growth in the HF process. It is also implied that the subcritical index n plays an important role, with the potential to significantly influence the growth of one or more hydraulic fracture(s). Hence, by showing the existence of time-dependent HF initiation and explaining that its underlying mechanism is due to the stable growth of the hydraulic fracture under subcritical conditions, this research leads to new insights for promoting more evenly growth of multiple hydraulic fractures in multi-stage HF treatments. Most importantly, this work shows that reducing the subcritical index shortens the time delay associated with hydraulic fracture initiation at wellbore pressures that are insufficient to induce instantaneous initiation. Reducing the subcritical index also promotes multiple hydraulic fracture growth, in some cases leading to growth of fractures that would be completely suppressed under classical conditions governed by Linear Elastic Fracture Mechanics. In turn, the experiments show that choice of fluid can impact the effective subcritical index, thereby leading to the practically-relevant outcome that fluid(s) can be chosen in order to promote initiation and growth of multiple hydraulic

fractures and/or single hydraulic fractures under conditions where the required wellbore pressure for instantaneous initiation cannot be reached.

A APPENDICES FOR "MODELING INITIATION AND PROPAGATION OF A HYDRAULIC FRACTURE UNDER SUBCRITICAL CONDITIONS"

A. FLUID LOSS AT EARLY TIME OF HF TREATMENT

During the HF process, it is common that a fraction of the fracturing fluid is lost by infiltrating into the rock formation. Since our research focuses on the early time of the HF initiation and subsequent growth, an estimation of the rate of the fluid loss is necessary for determining the importance of fluid leak-off within this particular time duration. Here we consider the plane strain case as an example.

Before the fracture is initiated, the loss of the fluid stored in the system is mainly attributed to fluid infiltration to the surrounding rock from the wellbore. This process is approximated below by a one-dimensional (1D) fluid flow through a porous medium in a half-plane. This 1D assumption is valid at very early time, when the infiltrated zone is much smaller than the wellbore radius. At large time, the infiltration follows radial flow. Here we consider the early time, 1D solution because early time behavior of the system is our main interest for hydraulic fracture initiation. Thus the reservoir pore pressure distribution is governed by the diffusion equation,

$$\frac{dp_r}{dt} = D\frac{d^2p_r}{dx^2} \tag{A.1}$$

where x is the distance from the center of the wellbore, D is the hydraulic diffusivity defined as $D = \frac{k}{\phi c_f \mu}$, and k, ϕ, and c_f are, correspondingly, the rock's permeability, porosity, and the fluid compressibility. The initial and boundary conditions for Eq. (A.1) are

$$\begin{aligned} p_r(x,t) &= p_w \quad x = a \\ p_r(x,0) &= p_0 \quad x > a \\ p_r(x,t) &= p_0 \quad x \to \infty \end{aligned} \tag{A.2}$$

where p_0 is the initial reservoir pore pressure in the rock. The solution of Eq. (A.1) can be readily found as

$$p_r(x,t) = p_0 + (p_w - p_0)\,\mathrm{erfc}\left(\frac{x-a}{2\sqrt{Dt}}\right) \tag{A.3}$$

in which $\mathrm{erfc}(\cdot)$ is the complementary error function. Eq. (A.3) shows that the induced reservoir pore pressure in the rock dissipates rapidly with the distance from the wellbore. (For example, for an HF treatment with $a = 0.1$ m, $k = 10^{-15}$ m^2, $\mu = 0.001$ Pa $\cdot$ s, $\phi = 0.1$, and $c_f = 2 \times 10^{-10}$ Pa^{-1}, within a practical time duration for initiating the HF, $t = O(10)$ second, the change in the reservoir pore pressure, $\triangle p = p_r - p_0$, is computed: $\triangle p = 0.37\,(p_w - p_0)$ at $x = 1$ m, and $\triangle p = 0.06\,(p_w - p_0)$ at $x = 2$ m). Once the pressure gradient is obtained, the rate of fluid loss into the rock can be determined using Darcy's law for the radial flow:

$$q = 2\pi \frac{k}{\mu} \frac{p_w - p_r(x)}{\ln(x/a)} \tag{A.4}$$

Taking $x = 2$ m, and $p_w - p_0 = O(10^7)$ Pa, the estimated leak-off rate before fracture initiation is obtained from Eq. (A.4) as $q = O(10^{-5})$ m^2/s. Hence, we obtain $q \ll Q_0$ ($Q_0 = O(10^{-3})$ m^2/s).

Once the crack starts to propagate, the fluid loss is assumed to be governed by the Carter's leak-off model (Carter, 1957), which comes into play through the continuity equation,

$$\frac{\partial w}{\partial t} + \frac{\partial q}{\partial x} + g(x,t) = 0 \tag{A.5}$$

In Eq. (A.5), the sink term g denotes the velocity of the fluid infiltration into the surrounding medium at point x, which, according to Carter's model, can be expressed as

$$g\left(x,t\right)=\frac{2C_L}{\sqrt{t-t_0\left(x\right)}}\quad t>t_0\left(x\right) \tag{A.6}$$

in which $C_L=\sqrt{\frac{kc_f\phi}{\pi\mu}}\triangle p_c$, and $\triangle p_c$ is defined as the difference between the fluid pressure in the fracture and the reservoir pressure, and $t_0(x)$ represents the time when the fracture arrives at point x. Assuming $\triangle p_c=O(10^6)$ Pa, then for a fracture that propagates within 100 seconds, $g=O(10^{-6})$ $^m/_\mathrm{s}$. For a certain point, x, if we take $\frac{dw}{dt}=O(10^{-4})$ $^m/_\mathrm{s}$ (it is physical to assume that a crack opens at a velocity of 10 mm per 100 seconds), then we obtain $g\ll\frac{dw}{dt}$. Thus, the rate of fluid loss, g, in Eq. (A.5) is negligible, and the continuity equation is reduced to

$$\frac{\partial w}{\partial t}+\frac{\partial q}{\partial x}=0 \tag{A.7}$$

From the above analysis, it follows that the fluid loss during early time of an HF treatment is often negligible, and hence we have verified the assumption that the rock can be treated as an impermeable medium in this particular problem.

B. DISCRETIZATION OF ELASTICITY EQUATIONS

1. Plane strain

For plane strain, the bi-wing fracture originating from a circular wellbore is modeled using the displacement discontinuity method (Crouch and Starfield, 1983). Only one half of the circular wellbore boundary and one wing of the bi-wing fracture, defined by $x>0$, are discretized due to the symmetry of the problem. The crack wing and the half-circular boundary of the wellbore wall are discretized by using the constant-strength DD elements of a uniform size. A total of m elements along the fracture and h elements along the wellbore wall are obtained from the discretization of the boundary. The influence of a DD element onto the stress at the midpoint of another element is given in Crouch and Starfield (1983).

Thus, the elastic boundary integral equation (II.5) can be written in the matrix form (after scaling) as

$$\begin{aligned} \mathbf{A_{nn}\Omega_n} + \mathbf{A_{ns}\Omega_s} &= \mathbf{\Phi_n} \\ \mathbf{A_{sn}\Omega_n} + \mathbf{A_{ss}\Omega_s} &= \mathbf{0} \end{aligned} \tag{A.8}$$

where $\mathbf{\Omega_n}$ and $\mathbf{\Omega_s}$ are the vectors of scaled normal and shear displacement jumps along both the wellbore and the fracture, $\mathbf{\Phi_n}$ denotes the vector of normal stress acting at the midpoints of the DD elements, and the expressions for the components of the influence coefficient matrix $\mathbf{A}$ can be found in Crouch and Starfield (1983). By rearranging the system, we obtain

$$\mathbf{B\Omega_n} = \mathbf{\Phi_n} \tag{A.9}$$

where $\mathbf{B} = \mathbf{A_{nn}} - \mathbf{A_{ns}A_{ss}^{-1}A_{sn}}$. The system of equations can be partitioned to account for the fracture and the wellbore elements. Therefore, we have

$$\begin{pmatrix} \mathbf{B_{ff}} & \mathbf{B_{fw}} \\ \mathbf{B_{wf}} & \mathbf{B_{ww}} \end{pmatrix} \begin{pmatrix} \mathbf{\Omega_f} \\ \mathbf{\Omega_w} \end{pmatrix} = \begin{pmatrix} \mathbf{\Phi_f} \\ \mathbf{\Pi_w} \end{pmatrix} \tag{A.10}$$

where the subscripts "f" and "w" correspond, respectively, to the fracture and the wellbore. In Eq. (A.10), $\mathbf{\Phi_f}$ includes the fluid pressure and the normal stress induced by the in-situ stresses, computed at the midpoints of the DD elements, i.e., $\mathbf{\Phi_f} = \mathbf{\Pi_f} + \mathbf{\Phi_{\theta\theta}}$, where the components of the vector $\Phi_{\theta\theta}$ are $\Phi_{\theta\theta j} = -\Phi_{hj}\left(1 + \frac{\mathcal{A}^2}{\xi_j^2}\right) - \frac{\Phi_{Dj}}{2}\left(\frac{\mathcal{A}^2}{\xi_j^2} - 3\frac{\mathcal{A}^4}{\xi_j^4}\right)$. $\mathbf{\Pi_w}$ denotes the vector of the scaled wellbore pressure applied at the midpoints of the DD elements along the wellbore. After some algebra, the following relationship is derived

$$\mathbf{\Phi_f} = \mathbf{M_1\Omega_f} + \mathbf{M_2\Pi_w} \tag{A.11}$$

in which $\mathbf{M_1} = \mathbf{B_{ff}} - \mathbf{B_{fw}B_{ww}^{-1}B_{wf}}$ and $\mathbf{M_2} = \mathbf{B_{fw}B_{ww}^{-1}}$. Because of the continuity of the fluid pressure between the wellbore and the fracture, we impose $\Pi_w = \Pi_{f_1}$. Therefore, Eq. (A.11) can be written as

$$\mathbf{\Pi_f} = \mathbf{C\Omega_f} - \mathbf{S} \tag{A.12}$$

where $\mathbf{C} = \mathbf{M_1} + diag(\mathbf{V_1}) \cdot \mathbf{M_3}$, $(V_1)_i = \frac{\sum_{j=1}^{h}(M_2)_{ij}}{1-\sum_{j=1}^{h}(M_2)_{1j}}$, $(M_3)_{ij} = (M_1)_{1j}$, and $diag(\mathbf{V_1})$ gives a square diagonal matrix with the elements in vector $\mathbf{V_1}$ on the main diagonal. In Eq. (A.12), $\mathbf{S}$ accounts for the normal stresses acting on the fracture due to both the in-situ stresses and wellbore pressure. It is given by $\mathbf{S} = (\varphi_1, \ldots, \varphi_m)^{\mathrm{T}}$, and $\varphi_i = \frac{\sum_{j=1}^{h}(M_2)_{ij}}{1-\sum_{j=1}^{h}(M_2)_{1j}}\Phi_{\theta\theta 1} + \Phi_{\theta\theta i}$. Note that, m and h are the numbers of elements along the fracture and the wellbore wall.

2. Axisymmetry

For a transverse axisymmetric fracture propagating from a wellbore, the elasticity equation is formulated using the dislocation kernel as follows (Abbas and Lecampion, 2013; Keer et al., 1977; Lecampion and Desroches, 2015)

$$p(\rho, t) = \frac{E'}{a}\int_1^{1+l/a} g^{wb}(\rho, s)\frac{\partial w(s,t)}{\partial s}ds \tag{A.13}$$

Integrating by parts and accounting for the tip boundary condition, we have

$$p(\rho, t) = \frac{E'}{a}\left(-\int_1^{1+l/a}\frac{\partial g^{wb}(\rho, s)}{\partial s}w(s,t)\,ds - g^{wb}(\rho, 1)\,w(1,t)\right) \tag{A.14}$$

which has the scaled form

$$-\Pi\mathcal{A} = \int_1^{1+\gamma/\mathcal{A}}\frac{\partial g^{wb}(\rho, s)}{\partial s}\Omega(s,\tau)\,ds + g^{wb}(\rho, 1)\,\Omega(1,\tau) \tag{A.15}$$

The axisymmetric dislocation kernel g^{wb} is defined as

$$g^{wb}(\rho, s) = \frac{1}{2\pi}s\left[R(\rho, s) + S(\rho, s)\right] \tag{A.16}$$

where

$$R(\rho, s) = \begin{cases} \frac{1}{\rho^2 - s^2}\mathbf{E}\left(\frac{\rho}{s}\right), & \rho < s \\ \frac{\rho}{s}\frac{1}{\rho^2 - s^2}\mathbf{E}\left(\frac{s}{\rho}\right) - \frac{1}{\rho s}\mathbf{K}\left(\frac{s}{\rho}\right), & \rho > s \end{cases} \tag{A.17}$$

in which $\mathbf{K}$ and $\mathbf{E}$ denote the complete elliptic integrals of the first and second kind, defined by $\mathbf{K}(k) = F\left(\frac{\pi}{2}, k\right)$ and $\mathbf{E}(k) = E\left(\frac{\pi}{2}, k\right)$ (Gradshteyn and Ryzhik, 2007), and

$$F(\varphi, k) = \int_0^{\varphi} \frac{d\alpha}{\sqrt{1 - k^2 \sin^2 \alpha}} = \int_0^{\sin\varphi} \frac{dx}{\sqrt{(1-x^2)(1-k^2x^2)}} \tag{A.18}$$

$$E(\varphi, k) = \int_0^{\varphi} \sqrt{1 - k^2 \sin^2 \alpha} d\alpha = \int_0^{\sin\varphi} \frac{\sqrt{1-k^2x^2}}{\sqrt{1-x^2}} dx \tag{A.19}$$

and S is given by Abbas and Lecampion (2013); Keer et al. (1977); Lecampion and Desroches (2015). Again, by applying the DD method, the integral is approximated as a linear system

$$\mathbf{M_1\Omega}+\mathbf{M_2\Omega} = -\mathcal{A}\mathbf{\Pi} \tag{A.20}$$

where

$$M_{1ij} = g^{wb}(\rho_i, \rho_j + \triangle\rho/2) - g^{wb}(\rho_i, \rho_j - \triangle\rho/2)$$

$$M_{2ij} = \begin{cases} g^{wb}(\rho_i, \rho_1 - \triangle\rho/2) & j = 1 \\ 0 & j \neq 1 \end{cases}$$

The same elasticity matrix as (A.12) is then deduced from (A.20) with $\mathbf{C} = -(\mathbf{M_1} + \mathbf{M_2})/\mathcal{A}$, and $\varphi_i = -\sigma_h$, for $i = 1, \ldots, m$.

C. SOLUTION FOR THE TIME STEP (FRACTURE PROPAGATION PHASE)

For the given crack length γ^N at step N, the algorithm finds the corresponding time step $\triangle\tau$. For both the conventional HF and the subcritical propagation models, we construct two loops in our algorithm, which are referred to as the outer and the inner loop, respectively. In the inner loop, we obtain $\triangle\mathbf{\Omega}$ for a given $\triangle\tau$. The outer loop finds the solution for the time step $\triangle\tau$. The algorithm for the subcritical growth problem is based on the bisection method for the outer loop, and the fixed-point iteration for the inner loop:

I. Start the outer loop. Obtain the values of Ω^{N-1} , γ^{N-1} and κ^{N-1} from the previous step, where $\kappa = K_{\mathrm{I}}/K_{\mathrm{IC}}$, and for plane strain (Thomas and Pollard, 1993)

$$K_{\mathrm{I}} = 0.806\frac{E'w^{tip}}{4\sqrt{\Delta/\pi}} \tag{A.21}$$

where w^{tip} and Δ are the opening and the length of DD element at crack tip, and for axisymmetry (Gordeliy and Detournay, 2011a)

$$K_{\mathrm{I}} = \frac{3}{8}\frac{E'w^{tip}}{\sqrt{2\Delta/\pi}} \tag{A.22}$$

Then choose two initial guesses for the time step, $\triangle\tau^0$ and $\triangle\tau^1$, for the lower and the upper bounds for the root of the function (II.37) (i.e., such that $f\left(\triangle\tau^0\right)\cdot f\left(\triangle\tau^1\right) < 0$). Set $K = 1$.

II. While $K \leq$ max iteration number, set the time step to the midpoint value $\triangle\tau^{K+1} = \frac{\triangle\tau^K + \triangle\tau^{K-1}}{2}$.

III. Start the inner loop. Set $k = 0$. Impose initial values of $\triangle\mathbf{\Omega}^0$ to be zero.

   A. Solve the system (Eq. II.36) for given values of $\triangle\tau^{K+1}$, Ω^{N-1}, and γ^{N-1}.

   B. Compare $\triangle\Omega^{k+1}$ and $\triangle\Omega^k$. If the solution converges within a given tolerance, continue. Else, let $k = k+1$, go to (a).

IV. If $|\triangle\tau^{K+1} - \triangle\tau^K|$ is less than a given tolerance, write results and go to 1. Else if $\mathrm{sign}\left(f\left(\triangle\tau^{K+1}\right)\right) = \mathrm{sign}\left(f\left(\triangle\tau^K\right)\right)$, then replace $\triangle\tau^K$ by $\triangle\tau^{K-1}$. Set $K = K+1$, go to step 2.

Once the critical condition is reached (i.e., $K_{\mathrm{I}} = K_{\mathrm{IC}}$), the simulation switches to the algorithm for the classical HF model:

I. Start the outer loop. Obtain the values of $\mathbf{\Omega}^{N-1}$ and γ^{N-1} from the previous step. Choose an initial guess $\triangle\tau^0$, let $K = 0$.

II. While $K \leq$ max iteration number, set the time step to $\triangle\tau^K$.

III. Start the inner loop. Set $k = 0$. Impose initial values of $\triangle\mathbf{\Omega^0}$ to be zero.

   A. Solve the system of Eq. (II.36) for $\triangle\mathbf{\Omega}^{k+1}$ using given values of $\triangle\tau^K$, Ω^{N-1}, and γ^{N-1}.

B. Compare $\triangle\Omega^{k+1}$ and $\triangle\Omega^{k}$. If the solution converges within a given tolerance, continue to 4. Else, let $k = k + 1$, go to (a).

IV. Check if the new crack tip opening, obtained from the inner loop, Ω_m, satisfies the tip asymptote (Eq. II.21 with $v/\alpha = 1$). If the relative error is within a given tolerance, write results and go to 1. Else, $K = K + 1$, adjust the solution for the crack opening so that Ω_m satisfies the tip asymptote (II.21), update $\triangle\tau^{K}$ from the global volume balance (Eq. II.38) and go to 2.

D. VALIDATION OF THE DISCRETIZED ELASTIC EQUATION (PLANE STRAIN)

Verification for the discretization of elastic equation (II.5) in the plane strain case is carried out by comparing our results for the crack width and the stress intensity factor with available numerical solutions (Lecampion, 2012a; Nilson and Proffer, 1984; Tada et al., 2000) for the following problem: a bi-wing crack emanating from a circular borehole with evenly distributed fluid pressure $p_w = p_f = 31$ MPa along the wellbore and the crack, in the presence of far-field stresses $\sigma_h = 30$ MPa, $\sigma_H = 35.77$ MPa (see problem geometry in Fig. II.1). In these simulations, the plane strain Young's modulus and the Poisson's ratio of the rock are set to $E' = 30$ GPa and $\nu = 0.3$; and the wellbore radius is $a = 0.1$ m. Three values of the crack length are considered: $l = 0.005$ m (short), $l = 0.105$ m (intermediate), and $l = 10$ m (long). First, fine mesh sizes are used in Subsection A.D.1 for all three cases, to confirm the validity of the DD discretization of the wellbore and the fracture employed in Eq. (II.5) by comparing our results to available numerical solutions. Next, a study on accuracy of the results with different mesh sizes is carried out in Subsection A.D.2 to verify the accuracy of this DD discretization for a practical mesh size.

1. Comparison with reference solutions

In this section, the three cases with short, intermediate and long cracks are modeled with fine mesh sizes in order to obtain the solutions independent of the element size. We used 6000 elements along the wellbore for the cases of the short and the intermediate cracks, and 60 elements along the wellbore for the case of the long crack. For each case, the element size along the wellbore and the crack was the same. Our simulation results for the normal displacement jump $[u_n]$ along the crack (i.e., the crack opening w) are compared to the following reference numerical solutions: (i) solutions from the model 1DPlanarHF (Lecampion, 2012a,b; Lecampion et al., 2013), based on the DD discretization of the fracture and an integral formulation with the elastic kernel that accounts for the interaction of an edge dislocation on the crack with the circular borehole (Dundurs and Mura, 1964); and (ii) solutions computed using the approximate generalized integral formulas of Nilson and Proffer (1984) based on the weight-function technique. In all three cases, the results from 1DPlanarHF were computed using a very fine mesh (2000 elements along the crack) in order to obtain the solution independent of the element size. It should be noted that the approximate formula of Nilson and Proffer (1984) is accurate for short and long cracks, while its error for the intermediate crack length can be in the order of 5%, as follows from Fig. 1 in Nilson and Proffer (1984). (A similar range of accuracy from using a modification of formulas of Nilson and Proffer (1984) has been reported by Garagash and Sarvaramini (2012) as ˜0.5% for a short crack, ˜1-10% for an intermediate crack, and 0% for a long crack.) Hence, it is important for this interpretation to realize that Nilson and Proffer's solution (Nilson and Proffer, 1984) captures the short and long crack limits accurately, but relies on an approximate interpolation between these limits, and the numerical solutions from 1DPlanarHF are more reliable in the transition. The results are shown in Fig. A1.

The comparison shows that the crack width is in good agreement with the numerical results from 1DPlanarHF (Lecampion, 2012a) for all three cases. Furthermore, our results match well to the solution of Nilson and Proffer (1984) for the two limiting cases (short and long cracks), and exhibit a 0˜10% difference for the intermediate crack length.

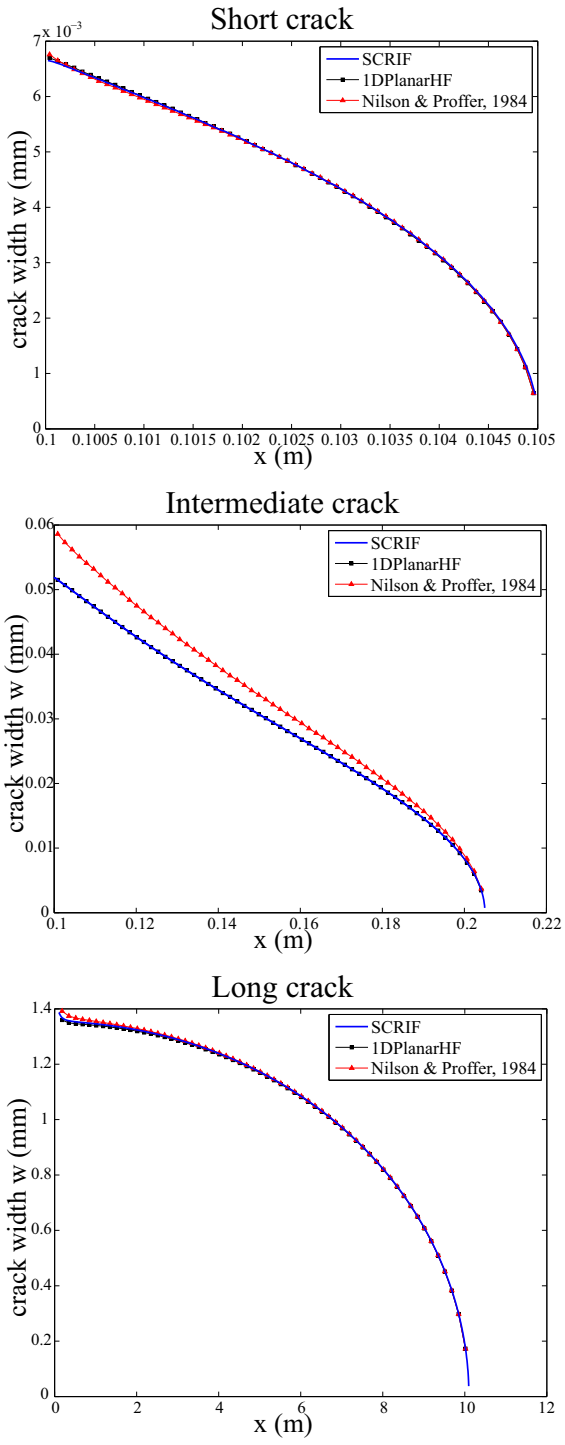

Figure A1: Comparison of crack opening of a plane strain bi-wing fracture from wellbore with $a = 0.1\ m,\ l = 0.005$ m (top), $a = 0.1\ m,\ l = 0.105$ m (middle), and $a = 0.1\ m,\ l = 10$ m (bottom).

The stress intensity factor K_I for all simulations is compared with the reference solutions from 1DPlanarHF and from the approximate formula of Nilson and Proffer (1984) in Table A1. Additionally, in Table A1, the stress intensity factor from our model was compared with the results obtained using formulas given by Tada et al. (2000) with the expected accuracy of 1%. For each reference solution, we define the relative difference in the stress intensity factor as follows

$$D_r = \frac{\mid K_{\mathrm{I}} - K_{\mathrm{I}}^{\mathrm{ref}} \mid}{K_{\mathrm{I}}}$$

where K_I and $K_{\mathrm{I}}^{\mathrm{ref}}$ refer, correspondingly, to the values obtained from our model and from the reference solution.

As shown in Table A1, the relative difference with respect to the solution from 1DPlanarHF is within 1.5% for all three cases, and around 1% when comparing with the solutions from Tada et al. (2000) and Nilson and Proffer (1984) for the two limiting geometries (short and long cracks). The largest difference is observed in the case of an intermediate crack: 3.33% difference with the solution from Tada et al. (2000) and 5.97% difference with the solution from Nilson and Proffer (1984), which are both within the acceptable range given the expected accuracy of each of this reference solutions described above.

The above comparison confirms the validity of the DD discretization of the wellbore and the fracture employed in the present model in Eq. (II.5).

2. Accuracy for a practical mesh size

In the above comparisons, very fine mesh sizes are used in all three cases, which all require a large number of elements along the circular hole as well as the crack. Hence, it is necessary to investigate the accuracy of this wellbore elasticity representation when a reasonable number of elements is used to discretize the wellbore. As an illustration, we take the intermediate crack with three different mesh sizes, containing 24, 60, and 240 elements along the half-circular boundary of the wellbore. (Only one half of the circular wellbore boundary is discretized due to the symmetry of the problem.) For each case, the element size along the wellbore and the crack was the same. In each case, the crack width and the stress

Table A1: Stress intensity factor K_{I} for different crack lengths, compared with reference solutions.

Crack length		Short	Intermediate	Long
SCRIF	K_{I} $(\mathrm{MPa}\cdot\sqrt{\mathrm{m}})$	0.9475	1.1098	5.6973
1DPlanarHF	$K_{\mathrm{I}}^{\mathrm{ref}}$ $(\mathrm{MPa}\cdot\sqrt{\mathrm{m}})$	0.9365	1.0948	5.6152
	D_r	1.17%	1.35%	1.44%
Nilson and Proffer (1984)	$K_{\mathrm{I}}^{\mathrm{ref}}$ $(\mathrm{MPa}\cdot\sqrt{\mathrm{m}})$	0.9433	1.1760	5.6407
	D_r	0.45%	5.97%	0.99%
Tada et al. (2000)	$K_{\mathrm{I}}^{\mathrm{ref}}$ $(\mathrm{MPa}\cdot\sqrt{\mathrm{m}})$	0.9472	1.0727	5.6328
	D_r	0.04%	3.33%	1.13%

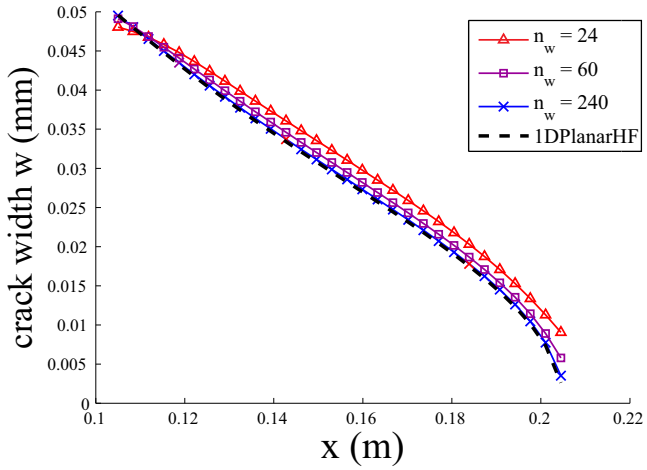

Figure A2: Crack opening for the intermediate crack using different numbers of elements along the wellbore: $n_w = 24$, 60, and 240. Results are compared with the numerical solutions from 1DPlanarHF (Lecampion, 2012a,b; Lecampion et al., 2013).

intensity factor are compared with the numerical solution from 1DPlanarHF (Lecampion, 2012a,b; Lecampion et al., 2013), obtained using a very fine mesh size (2000 elements along the crack). The comparison is presented in Fig. A2 and Table A2.

From Fig. A2 and Table A2, we see rapid convergence to the numerical solution from 1DPlanarHF (Lecampion, 2012a,b; Lecampion et al., 2013) in both crack width and stress intensity factor as the number of elements along the wellbore increases. Discretizing the wellbore with 240 elements gives accurate crack width, and 2.3% error in the stress intensity factor. In all simulations in Section II.G.2 in this paper we used 200 elements to discretize the wellbore.

Table A2: Stress intensity factor K_{I} for an intermediate crack using different numbers of elements along the wellbore: $n_w = 24$, 60, and 240, compared to numerical solutions by Lecampion (2012a,b).

	1DPlanarHF	SCRIF ($n_w = 24$)	SCRIF ($n_w = 60$)	SCRIF ($n_w = 240$)
K_{I} (MPa $\cdot \sqrt{\mathrm{m}}$)	1.0948	1.2056	1.1520	1.1205
D_r	-	9.19%	4.97%	2.30%

B APPENDICES FOR "MODELING SIMULTANEOUS INITIATION AND PROPAGATION OF MULTIPLE HYDRAULIC FRACTURES UNDER SUBCRITICAL CONDITIONS"

A. DISCRETIZATION OF ELASTICITY EQUATIONS

For the Ith fracture, using a piece-wise constant approximation for the crack width (i.e. w is constant in each DD element) and a piece-wise linear approximation for the shear displacement jump (i.e. $v = r'\hat{v}$, where $\hat{v}$ is constant in each DD element) the elasticity equations (III.2) and (III.3) can be written in the matrix form as

$$\begin{aligned}
\mathbf{A}^{II}_{\mathbf{nn}}\mathbf{w}^I + \mathbf{A}^{II}_{\mathbf{ns}}\hat{\hat{\mathbf{v}}}^I &= \mathbf{P}^I_{\mathbf{f}} - \boldsymbol{\sigma}^I_{\mathbf{n}} - \sum_{\substack{J\neq I \\ \gamma^J > 5\mathcal{A}}} \left(\mathbf{A}^{IJ}_{\mathbf{nn}}\mathbf{w}^J + \mathbf{A}^{IJ}_{\mathbf{ns}}\hat{\hat{\mathbf{v}}}^J\right) \\
\mathbf{A}^{II}_{\mathbf{sn}}\mathbf{w}^I + \mathbf{A}^{II}_{\mathbf{ss}}\hat{\hat{\mathbf{v}}}^I &= - \sum_{\substack{J\neq I \\ \gamma^J > \mathbf{5}\mathcal{A}}} \left(\mathbf{A}^{IJ}_{\mathbf{sn}}\mathbf{w}^J + \mathbf{A}^{IJ}_{\mathbf{ss}}\hat{\hat{\mathbf{v}}}^J\right)
\end{aligned} \tag{B.1}$$

in which $\mathbf{w}^I = \begin{bmatrix} w^I_1 & \cdots & w^I_m \end{bmatrix}^{\mathrm{T}}$, $\hat{\hat{\mathbf{v}}}^I = \begin{bmatrix} \hat{v}^I_1 & \cdots & \hat{v}^I_m \end{bmatrix}^{\mathrm{T}}$, $\mathbf{P}_f{}^I = \begin{bmatrix} p^I_{f1} & \cdots & p^I_{fm} \end{bmatrix}^{\mathrm{T}}$, and the components of the influence coefficient matrix $\mathbf{A}$ are given by

$$\begin{aligned}
\left[\mathbf{A}^{IJ}_{\mathbf{nn}}\right]_{ij} &= \int_{r^J_j - \triangle r^J/2}^{r^J_j + \triangle r^J/2} \sigma_{zzzz}\left(r^I_i, z^I; r', z^J\right) dr' \\
\left[\mathbf{A}^{IJ}_{\mathbf{ns}}\right]_{ij} &= \int_{r^J_j - \triangle r^J/2}^{r^J_j + \triangle r^J/2} \sigma_{zzrz}\left(r^I_i, z^I; r', z^J\right) r' dr' \\
\left[\mathbf{A}^{IJ}_{\mathbf{sn}}\right]_{ij} &= \int_{r^J_j - \triangle r^J/2}^{r^J_j + \triangle r^J/2} \sigma_{rzzz}\left(r^I_i, z^I; r', z^J\right) dr' \\
\left[\mathbf{A}^{IJ}_{\mathbf{ss}}\right]_{ij} &= \int_{r^J_j - \triangle r^J/2}^{r^J_j + \triangle r^J/2} \sigma_{rzrz}\left(r^I_i, z^I; r', z^J\right) r' dr'
\end{aligned} \tag{B.2}$$

The integrals in Eq. (B.2) are evaluated analytically by expressing the kernels for the ring dislocation dipoles (σ_{ijkl}) via derivatives of the ring dislocation kernels, given in Appendix B of Gordeliy and Detournay (2011a). Eq. (B.1) can be rewritten as the following linear system

$$\begin{aligned} \mathbf{A_{nn}w} + \mathbf{A_{ns}}\hat{\hat{\mathbf{v}}} &= \mathbf{P_{net}} \\ \mathbf{A_{sn}w} + \mathbf{A_{ss}}\hat{\hat{\mathbf{v}}} &= \mathbf{0} \end{aligned} \tag{B.3}$$

where $\mathbf{P_{net}}$ is defined as $\mathbf{P_{net}} = \mathbf{P_f} - \boldsymbol{\sigma}_\mathbf{n}$, and $\mathbf{w}$, $\hat{\hat{\mathbf{v}}}$, $\mathbf{P_f}$, and $\boldsymbol{\sigma}_\mathbf{n}$ are taken as the union of all cracks. By rearranging Eq. (B.3), we get

$$\mathbf{Hw} = \mathbf{P_{net}} \tag{B.4}$$

in which $\mathbf{H}$ is given by $\mathbf{H}= \mathbf{A_{nn}} - \mathbf{A_{ns}}\mathbf{A_{ss}^{-1}}\mathbf{A_{sn}}$. Eq. (B.4) is scaled as

$$\bar{\mathbf{H}}\boldsymbol{\Omega} = \boldsymbol{\Pi}_\mathbf{net} \tag{B.5}$$

where $\bar{\mathbf{H}} = \mathbf{H}\frac{w_*}{p_*}$. Finally, the elastic matrix for each crack $I = 1, \ldots, N$ is given by

$$\boldsymbol{\Pi}^I = \mathbf{C}\boldsymbol{\Omega}^I - \mathbf{S} \tag{B.6}$$

In Eq. (B.6), $\mathbf{C} = \bar{\mathbf{H}}^{II}$ and $\mathbf{S} = -\hat{\boldsymbol{\sigma}}^I_\mathbf{n} - \sum_{\substack{I \neq J \\ \gamma^J > 5\mathcal{A}}} \left(\mathbf{H}^{IJ} \cdot \boldsymbol{\Omega}^J\right)$. Note that, if the crack radius is less than five times the wellbore radius, then the elastic kernel given in Eqs. (24) - (29) of Keer et al. (1977) is used to compute matrix $\mathbf{C}$ for including the effect of the wellbore.

C APPENDICES FOR "TIME-DEPENDENT HYDRAULIC FRACTURE INITIATION: LABORATORY EXPERIMENTS AND NUMERICAL MODELING"

A. DOUBLE TORSION (DT) EXPERIMENTS ON GRANITE

Double Torsion (DT) experiments have been used in past studies to measure parameters associated with subcritical crack growth for various materials. In this experiment, our goal is to obtain the subcritical crack growth index n for Coldspring Charcoal Granite. Specimens have dimensions of 60 mm $\times$ 150 mm $\times$ 6 mm, and are notched and grooved along the central line (see Fig. C1). Four experiments have been performed using the following procedures (adopted from the original method for DT experiments developed by Evans (1972), and revised by Holder et al. (2001)):

I. Pre-load the specimen by constant displacement steps with certain time interval until the sign of initial crack (see typical evolution of the induced stress intensity factor with time for a tested specimen in Fig. C2);

II. Measure the crack length a_i and load P_i induced by the displacement as soon as the last displacement is applied;

III. Arrest by keeping the constant displacement, and record load relaxation P during the period of stable crack growth;

IV. Examine the test data and compute the subcritical index n.

Hence, in each test, the specimen is loaded by incremental constant displacement steps until an initial crack is generated. Then the loading relaxation takes place in the following

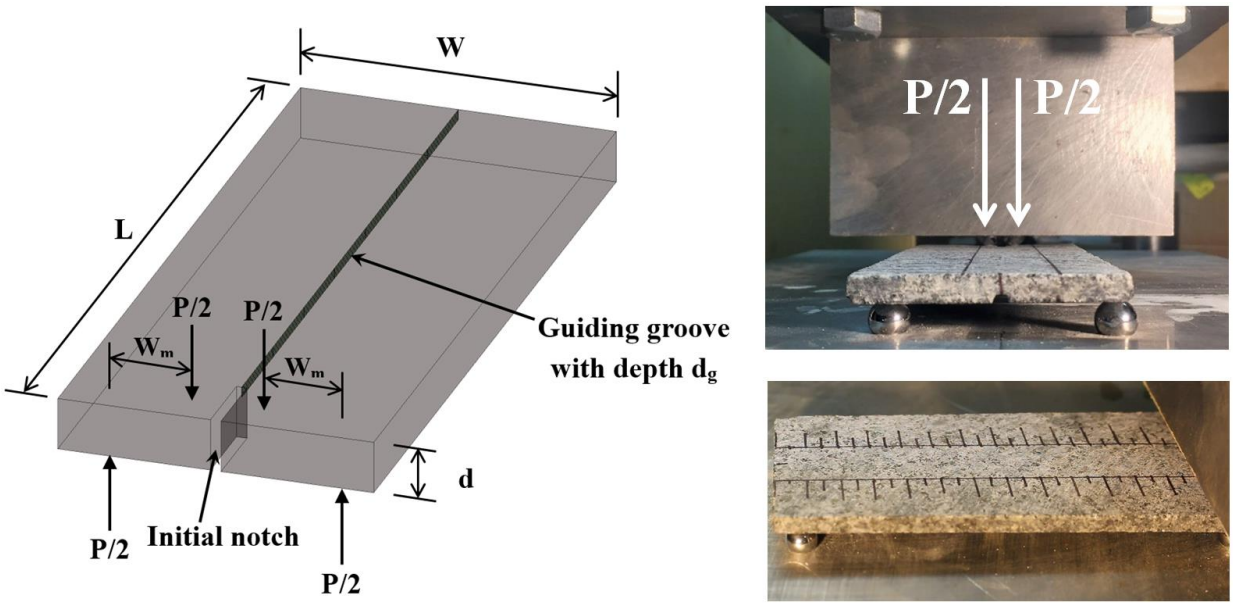

Figure C1: Experimental setup for DT tests (left) and photographs showing the specimen under loading (right).

step due to stable growth of the crack. During loading relaxation, the crack velocity is given by Evans (1972)

$$V = -\frac{a_i P_i}{P^2}\left(\frac{dP}{dt}\right) \tag{C.1}$$

and the stress intensity factor is calculated by

$$K_{\mathrm{I}} = P \cdot W_m \sqrt{\frac{1+\nu}{W d^3 d_n}} \tag{C.2}$$

where W_m is the moment arm for the applied load, W is the width, ν is Poisson's ratio, d is the thickness, and d_n is the thickness along the central groove ($d_n = d - d_g$). Rewriting Eq. (IV.1) and substituting it into Eq. (C.1), we have

$$\frac{V}{a_i} = -\frac{P_i}{P^2}\left(\frac{dP}{dt}\right) = C \cdot K_{\mathrm{I}}^n \tag{C.3}$$

where C is a constant. Fig. C2 plots the correlation of V/a_i and K_{I} for the four tests. According to Eq. (C.3), we use a power law correlation to fit the data sets, then the value of the subcritical index, n, is obtained as the power for each fitting curve. Although the value of n varies among the experiments (n = 15, 27, 8.6, 15.5), the range of subcritical index is narrowed down to an average value of 16.5 with a standard deviation of 7.7, compared to 10∼200 for its typical range in rocks.

B. ROLE OF ROUGHNESS CORRECTION

Here we show that the numerical model without the roughness correction is not capable of capturing the impact of the viscosity or confining stresses on the time to breakdown. Assuming there is no tip-roughness/viscosity effect in the tip region, then the tip asymptotic solution, Eq. (IV.10) is used in the model, together with all other components introduced in Sections IV.E.1 and IV.E.2. Using the same approach as in Section IV.F.1 to determine the value for n and l_0, we found that the case of $n = 25$, and $l_0 = 110\,\mu$m leads to a pressure versus lifetime correlation that matches the experimental data (see Case I in Fig. C3.a).

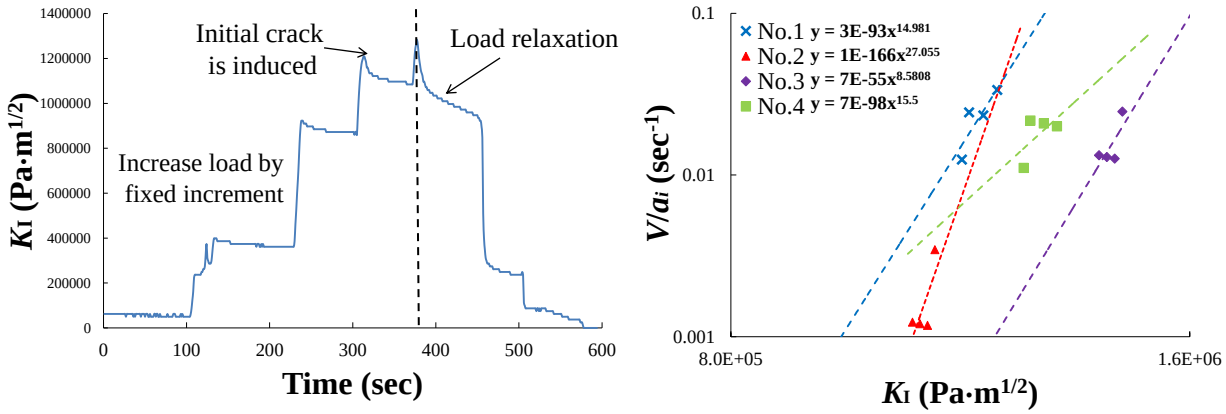

Figure C2: Evolution of the induced stress intensity factor K_{I} with time for a specimen (left), and correlation between V/a_i and K_{I} for all experiments (right). Power law curve fitting is used to derive the value of subcritical index n

These values are then used in simulations for the case of glycerin tests. In the absence of a tip-roughness/viscosity correction, the time to breakdown predicted by the numerical model is smaller by several orders of magnitude compared to the test results. Thus it is observed that the impact of fluid viscosity is vastly underestimated by the model without taking into account the roughness correction. In fact, these simulations show that the small and large viscosity cases in the laboratory are both associated with the fluid fully penetrating into the flaw and attaining a uniform pressure within the flaw because the propagation velocity of the crack is much smaller compared to the rupture velocity, which causes the fluid flow to slow down and tends to maintain a uniform fluid pressure along the whole crack regardless of the fluid viscosity. Hence, there is essentially no mechanism for generating appreciable difference between the cases.

If, on the other hand, we use l_0 and n as fitting parameters to match the glycerin tests ($l_0 = 30\,\mu$m, and $n = 18$, see Case II in Fig. C3.a), the value of l_0 is much smaller than our expectation (note that the scale of l_0 is interpreted as having the same order of magnitude as the pore size of the rock, which should be in the order of 100 μm), and this combination of the two parameters again causes inconsistency when substituted back into the simulations

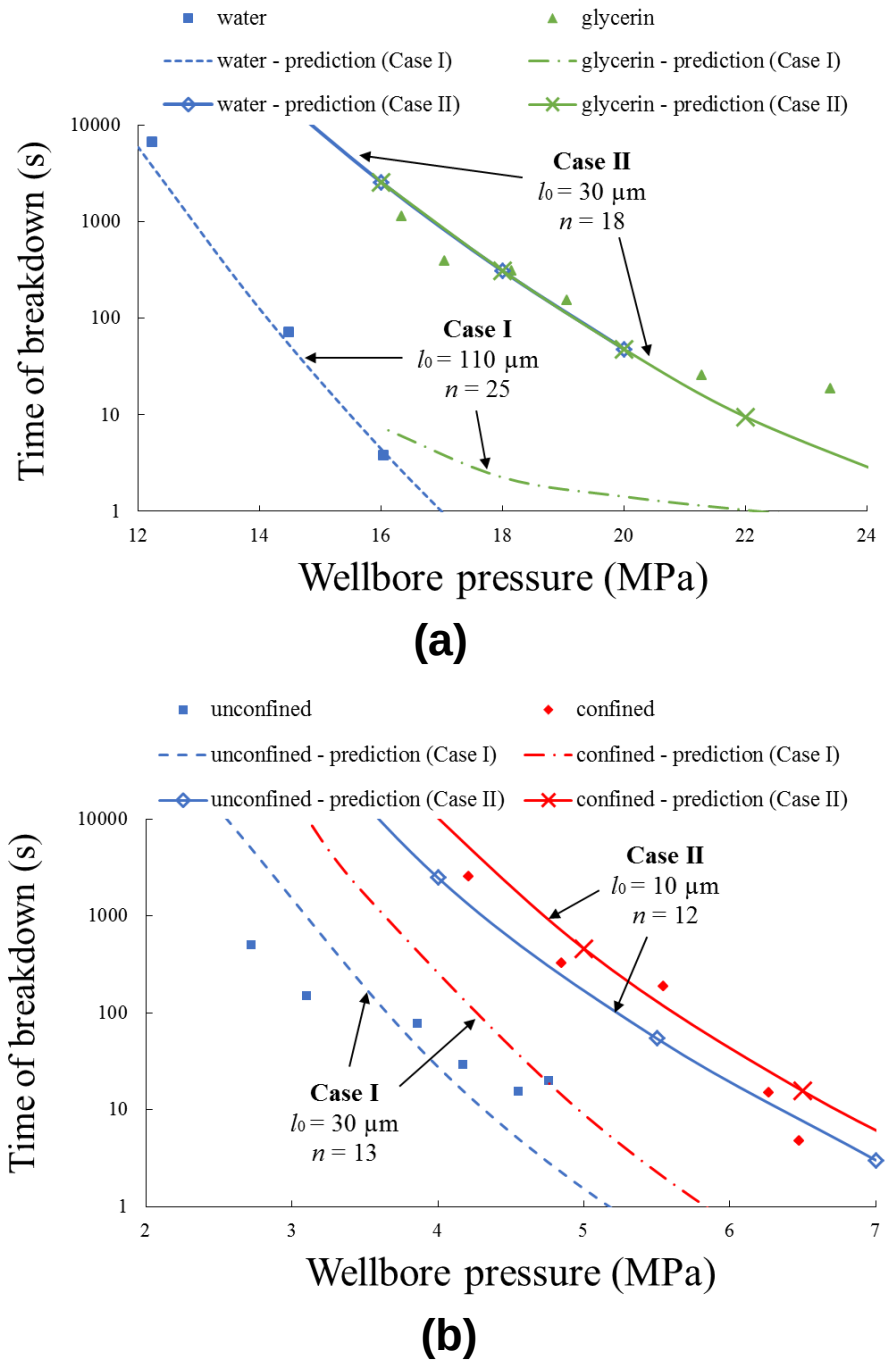

Figure C3: Numerical prediction of time to breakdown by the model without roughness correction for (a) granite and (b) sandstone. For each rock, two cases of l_0 and n values are used, and each combination of the values is derived by the best fit to the experimental data.

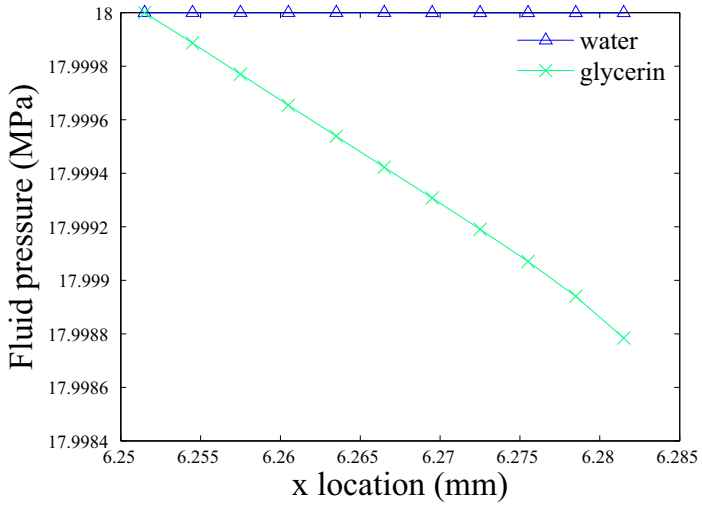

Figure C4: Distribution of fluid pressure obtained from the numerical model for granite tests injected by water and glycerin under the wellbore pressure of 18 MPa. For both fluids, $l_0 = 30\,\mu$m, and $n = 18$ as in Case II of Fig. C3.a

for the water case. Furthermore, for Case II, the difference between the predictions for water and glycerin becomes negligible (as indicated in the figure that the two curves almost overlap with each other). The fluid pressure distribution in the initial flaws for both water and glycerin cases under the wellbore pressure of 18 MPa is plotted in Fig. C4. As can be seen the fluid pressure is uniformly distributed along the initial crack in the case of water, and the pressure change along the crack in the glycerin case is almost zero - with variation occuring in the fifth digit. Therefore, it is implied by Fig. C4 that both water and glycerin cases are both characterized by fully penetrating fluid in the toughness-dominated regime. Hence, the difference in the time to breakdown must somehow be accounted for via the fluid's influence on resistance to crack propagation. For this reason we propose to adopt the roughness-viscosity correction described in Section IV.E.4.

Similar comparison has been carried out on the sandstone tests in Fig. C3.b. Case I gives the numerical prediction based on values of $l_0 = 30\,\mu$m, and $n = 13$ that fit the unconfined data set, and predictions in Case II use $l_0 = 10\,\mu$m, and $n = 12$. For both cases, we see a shift

in pressure, Δp, from unconfined to confined solutions. However, the shift is not sufficient in either of the two cases to enable simulation of both by choosing one combination of l_0 and n. Additionally, it is useful to note that fitting the data by making l_0 smaller for larger viscosity and/or larger confining stress cases, as we have done here, is similar to increasing the fracture toughness of the rock for these cases.

Based on these observations, we conclude that the numerical model without any correction term underestimates both the viscosity and the stress effect on the lifetime versus pressure relation, and it is necessary to adopt a correction. One possible route is to choose a correction bringing in a larger apparent fracture toughness for higher viscosity and higher confining stress. Hence, we are driven to adopt the roughness correction described in Section IV.E.4.

BIBLIOGRAPHY

Abbas, S. and Lecampion, B. (2013). Initiation and breakdown of an axisymmetric hydraulic fracture transverse to a horizontal wellbore. In Bunger, A. P., McLennan, J., and Jeffrey, R. G., editors, *Effective and Sustainable Hydraulic Fracturing*, chapter 19. Intech, Rijeka, Croatia.

Abbas, S., Lecampion, B., and Prioul, R. (2013). Competition between transverse and axial hydraulic fractures in horizontal wells. In *Proceedings SPE Hydraulic Fracturing Technology Conference and Exhibition*, The Woodlands, Texas, USA. SPE 163848.

Adachi, J. I. (2001). *Fluid-driven fracture in permeable rock*. PhD thesis, University of Minnesota, Minneapolis.

ASTM (2010a). ASTM E111-04 Standard test method for young's modulus, tangent modulus, and chord modulus. ASTM International, West Conshohocken, PA.

ASTM (2010b). ASTM E132-04 Standard test method for poisson's ratio at room temperature. ASTM International, West Conshohocken, PA.

Atkinson, B. K. (1984). Subcritical crack growth in geological materials. *J. Geophys. Res. Solid Earth*, 89(B6):4077–4114.

Atkinson, B. K. (1987). *Fracture mechanics of rock*. Elsevier.

Batchelor, G. (1967). *An Introduction to Fluid Dynamics*. Cambridge University Press, Cambridge UK.

Bunger, A. P. (2005). *Near-Surface Hydraulic Fracture*. PhD thesis, University of Minnesota, Minneapolis, MN.

Bunger, A. P. (2013). Analysis of the power input needed to propagate multiple hydraulic fractures. *Int. J. Solids Struct.*, 50:1538–1549.

Bunger, A. P. and Cardella, D. J. (2015). Spatial distribution of production in a marcellus shale well: Evidence for hydraulic fracture stress interaction. 133:162–166.

Bunger, A. P., Jeffrey, R. G., and Zhang, X. (2014). Constraints on simultaneous growth of hydraulic fractures from multiple perforation clusters in horizontal wells. *Soc. Pet. Eng. J.*, 19(04):608–620.

Bunger, A. P., Kear, J., Dyskin, A. V., and Pasternak, E. (2015). Sustained acoustic emissions following tensile crack propagation in a crystalline rock. *Int. J. Fract.*, 193(1):87–98.

Bunger, A. P., Lakirouhani, A., and Detournay, E. (2010). Modelling the effect of injection system compressibility and viscous fluid flow on hydraulic fracture breakdown pressure. In *Proceedings 5th International Symposium on In-situ Rock Stress*, pages 59–67, Beijing, P.R. China. ISRM-ISRS-2010-008.

Bunger, A. P. and Lu, G. (2015). Time-dependent initiation of multiple hydraulic fractures in a formation with varying stresses. *Soc. Pet. Eng. J.*, 20(06):1317–1325.

Bunger, A. P., Zhang, X., and Jeffrey, R. G. (2012). Parameters affecting the interaction among closely spaced hydraulic fractures. *Soc. Pet. Eng. J.*, 17(1):292–306.

Carter, E. (1957). Optimum fluid characteristics for fracture extension. In Howard, G. and Fast, C., editors, *Drilling and Production Practices*, pages 261–270. American Petroleum Institute, Tulsa OK.

Charles, R. J. (1958). Static fatigue of glass. i. *J. Appl. Phys.*, 29(11):1549–1553.

Crouch, S. and Starfield, A. (1983). *Boundary Element Methods in Solid Mechanics*. Unwin Hyman, London.

Crouch, S. L. (1976). Solution of plane elasticity problems by the displacement discontinuity method. i. infinite body solution. *Int. J. Numer. Meth. Engng*, 10(2):301–343.

Cruden, D. (1974). The static fatigue of brittle rock under uniaxial compression. *Int. J. Rock Mech. Min. Sci.*, 11(2):67–73.

Desroches, J., Lecampion, B., Ramakrishnan, H., Brown, J. E., and Prioul, R. (2014). Benefits of controlled hydraulic fracture placement: Theory and field experiment. In *SPE/CSUR Unconventional Resources Conference*, Calgary, Alberta, Canada. SPE 171667.

Detournay, E. and Carbonell, R. (1997). Fracture-mechanics analysis of the breakdown process in minifracture or leakoff test. *SPE Production & Facilities*, August:195–199. SPE 28076.

Detournay, E. and Peirce, A. (2014). On the moving boundary conditions for a hydraulic fracture. *Int. J. Eng. Sci.*, 84:147–155.

Dundurs, J. and Mura, T. (1964). Interaction between an edge dislocation and a circular inclusion. *J. Mech. Phys. Solids*, 12(177-189).

El Rabaa, W. (1989). Experimental study of hydraulic fracture geometry initiated from horizontal wells. In *Proceedings SPE Annual Technical Conference and Exhibition*, San Antonio, TX, USA. SPE 19720.

Evans, A. G. (1972). A method for evaluating the time-dependent failure characteristics of brittle materials — and its application to polycrystalline alumina. *J. Mater. Sci.*, 7(10):1137–1146.

Fernau, H., Lu, G., Bunger, A., Prioul, R., Aidagulov, G., et al. (2016). Load-rate dependence of rock tensile strength testing: Experimental evidence and implications of kinetic fracture theory. In *Proceedings 50th US Rock Mechanics/Geomechanics Symposium*. ARMA 16-369.

Fisher, M. K., Heinze, J. R., Harris, C. D., Davidson, B. M., Wright, C. A., and Dunn, K. P. (2004). Optimizing horizontal completion techniques in the Barnett shale using microseismic fracture mapping. In *Proceedings SPE Annual Technology Conference and Exhibition*, Houston, Texas, USA.

Gale, J. F. W., Reed, R. M., and Holder, J. (2007). Natural fractures in the Barnett shale and their importance for hydraulic fracture treatments. *AAPG Bull.*, 91(4):603–622.

Garagash, D. (2015). Roughness-dominated hydraulic fracture propagation. In *AGU Fall Meeting Abstracts*.

Garagash, D. I. and Sarvaramini, E. (2012). Equilibrium of a pressurized plastic fluid in a wellbore crack. *International Journal of Solids and Structures*, 49(1):197–212.

Germanovich, L. N., Ring, L. M., Astakhov, D. K., Shlyopobersky, J., and Mayerhofer, M. J. (1997). Hydraulic fracture with multiple segments II: Modeling. *Int. J. Rock Mech. Min. Sci.*, 34(3-4):472.

Gordeliy, E. and Detournay, E. (2011a). Displacement discontinuity method for modeling axisymmetric cracks in an elastic half-space. *Int. J. Solids Struct.*, 48(19):2614–2629.

Gordeliy, E. and Detournay, E. (2011b). A fixed grid algorithm for simulating the propagation of a shallow hydraulic fracture with a fluid lag. *Int. J. Numer. Anal. Meth. Geomech.*, 35(5):602–629.

Gordeliy, E. and Peirce, A. (2013). Implicit level set schemes for modeling hydraulic fractures using the xfem. *Computer Methods in Applied Mechanics and Engineering*, 266:125–143.

Gradshteyn, I. S. and Ryzhik, I. M. (2007). *Table of Integrals, Series, and Products*. Elsevier.

Haimson, B. and Fairhurst, C. (1967). Initiation and extension of hydraulic fractures in rocks. *Soc. Pet. Eng. J.*, pages 310–318. , SPE 1710.

Haimson, B. and Fairhurst, C. (1969). In-situ stress determination at great depth by means of hydraulic fracturing. In *Proceedings of The 11th U.S. Symposium on Rock Mechanics*, pages 559–584, Berkeley, CA.

Haimson, B. C. and Cornet, F. H. (2003). ISRM Suggested Methods for rock stress estimation – Part 3: hydraulic fracturing (HF) and/or hydraulic testing of pre-existing fracture (HTPF). *Int. J. Rock Mech. Min. Sci.*, 40:1011–1020.

Hills, D., Kelly, P., Dai, D., and Korsunsky, A. (1996). Solution of Crack Problems: The Distributed Dislocation Technique. volume 44 of *Solid Mechanics and its Applications*. Kluwer Academic Publ., Dordrecht.

Holder, J., Olson, J. E., and Philip, Z. (2001). Experimental determination of subcritical crack growth parameters in sedimentary rock. *Geophys. Res. Lett.*, 28(4):599–602.

Hubbert, M. and Willis, D. (1957). Mechanics of hydraulic fracturing. *Trans. AIME*, 210:153–168.

Irwin, G. R. (1957). Analysis of stresses and strains near the end of a crack transversing a plate. *ASME J. Appl. Mech.*, 24(3):361–364.

Kear, J. and Bunger, A. P. (2014). Dependence of static fatigue tests on experimental configuration for a crystalline rock. *Advanced Materials Research*, 892:863–871. Proceedings 11th International Fatigue Congress, Melbourne, Australia, 2-7 March.

Keer, L. M., Luk, V. K., and Freedman, J. M. (1977). Circumferential edge crack in a cylindrical cavity. *J. Appl. Mech.*, 44(2):250–254.

Kirsch, G. (1898). *Die theorie der Elastizität und die Bedürfnisse der Festigkeitslehre*. Springer.

Kuruppu, M., Obara, Y., Ayatollahi, M., Chong, K., and Funatsu, T. (2014). Isrm-suggested method for determining the mode i static fracture toughness using semi-circular bend specimen. *Rock Mechanics and Rock Engineering*, 47(1):267–274.

Lakirouhani, A., Bunger, A. P., and Detournay, E. (2008). Modeling initiation of hydraulic fractures from a wellbore. In *Proceedings 5th Asian Rock Mechanics Symposium*, pages 1101–1108, Tehran, Iran.

Lakirouhani, A., Detournay, E., and Bunger, A. (2016). A reassessment of in-situ stress determination by hydraulic fracturing. *Geophys. J. Int.*, 205(3):1859–1873.

Lecampion, B. (2012a). Hydraulic fracture initiation from an open-hole: Wellbore size, pressurization rate and fluid-solid coupling effects. In *Proceedings 49th US Rock Mechanics/Geomechanics Symposium*. American Rock Mechanics Association.

Lecampion, B. (2012b). Modeling size effects associated with tensile fracture initiation from a wellbore. *Int. J. Rock Mech. Min. Sci.*, 56:67–76.

Lecampion, B. and Desroches, J. (2015). Simultaneous initiation and growth of multiple radial hydraulic fractures from a horizontal wellbore. *J. Mech. Phys. Solids*, 82:235 – 258.

Lecampion, B., Peirce, A., Detournay, E., Zhang, X., Chen, Z., Bunger, A. P., Detournay, C., Napier, J., Abbas, S., Garagash, D., and Cundall, P. (2013). The impact of the near-tip logic on the accuracy and convergence rate of hydraulic fracture simulators compared to reference solutions. In Bunger, A. P., McLennan, J., and Jeffrey, R. G., editors, *Effective and Sustainable Hydraulic Fracturing*, chapter 43. Intech, Rijeka, Croatia.

Lhomme, T., Detournay, E., and Jeffrey, R. (2005). Effect of fluid compressibility and borehole radius on the propagation of a fluid-driven fracture. *Strength, Fracture, and Complexity*, 3(2-4):149–162.

Lim, P. V., Goddard, P., Sink, J., and Abou-sayed, I. S. (2014). Hydraulic fracturing: A Marcellus case study of an engineered staging completion based on rock properties. In *SPE/CSUR Unconventional Resources Conference*, Calgary, Alberta, Canada. SPE 171618.

Lu, G., Gordeliy, E., Prioul, R., Aidagulov, G., and Bunger, A. P. (Submitted). Modeling simultaneous initiation and propagation of multiple hydraulic fractures under subcritical conditions. *Comput. Geotech.*

Lu, G., Gordeliy, E., Prioul, R., Aidagulov, G., Uwaifo, E. C., Ou, Q., and Bunger, A. P. (In review). Time-dependent hydraulic fracture initiation. *J. Geophys. Res. Solid Earth.*

Lu, G., Gordeliy, E., Prioul, R., and Bunger, A. P. (2017a). Modeling initiation and propagation of a hydraulic fracture under subcritical conditions. *Computer Meth. Appl. Mech. Eng*, 318:61–91.

Lu, G., Uwaifo, E. C., Ames, B. C., Ufondu, A. U., Bunger, A. P., Prioul, R., and Aidagulov, G. (2015). Experimental demonstration of delayed initiation of hydraulic fractures below breakdown pressure in granite. In *Proceedings 49th US Rock Mechanics/Geomechanics Symposium*. ARMA 15-190.

Lu, Q., Lu, G., Bunger, A. P., Prioul, R., and Aidagulov, G. (2017b). Impact of fluid acidity on the time-dependent initiation of hydraulic fractures in carbonate rocks. In *Proceedings 51th US Rock Mechanics/Geomechanics Symposium*. ARMA 17-0200.

Meyer, B. and Bazan, L. (2011). A discrete fracture network model for hydraulically induced fractures-theory, parametric and case studies. In *Proceedings SPE Hydraulic Fracturing Technology Conference and Exhibition*, The Woodlands, Texas, USA. SPE 140514.

Miller, C., Waters, G., and Rylander, E. (2011). Evaluation of production log data from horizontal wells drilled in organic shales. In *Proceedings SPE North American Unconventional Gas Conference and Exhibition*, The Woodlands, Texas, USA. SPE 144326.

Nilson, R. and Proffer, W. J. (1984). Engineering formulas for fractures emanating from cylindrical and spherical holes. *ASME J. Appl. Mech.*, 51:929–933.

Olson, J. E. (1993). Joint pattern development: Effects of subcritical crack growth and mechanical crack interaction. *J. Geophys. Res. Solid Earth*, 98(B7):12251–12265.

Olson, J. E. (2004). Predicting fracture swarms – the influence of subcritical crack growth and the crack-tip process zone on joint spacing in rock. In Cosgrove, J. W. and Engelder, T., editors, *The initiation, propagation, and arrest of joints and other fractures*, volume 231, pages 73–87. Geological Society, London.

Olson, J. E. and Dahi-Taleghani, A. (2009). Modeling simultaneous growth of multiple hydraulic fractures and their interaction with natural fractures. In *Proceedings SPE Hydraulic Fracturing Technology Conference and Exhibition*, The Woodlands, Texas, USA.

Peirce, A. and Detournay, E. (2008). An implicit level set method for modeling hydraulically driven fractures. *Computer Meth. Appl. Mech. Eng*, 197:2858–2885.

Peirce, A. P. and Bunger, A. P. (2015). Interference fracturing: Non-uniform distributions of perforation clusters that promote simultaneous growth of multiple hydraulic fractures. *Soc. Pet. Eng. J.*, 20(02):384–395.

Rice, J. (1968). Mathematical analysis in the mechanics of fracture. In Liebowitz, H., editor, *Fracture, an Advanced Treatise*, volume II, chapter 3, pages 191–311. Academic Press, New York NY.

Rosakis, A., Samudrala, O., and Coker, D. (1999). Cracks faster than the shear wave speed. *Science*, 284(5418):1337–1340.

Savitski, A. and Detournay, E. (2002). Propagation of a penny-shaped fluid-driven fracture in an impermeable rock: asymptotic solutions. *Int. J. Solids Struct.*, 39:6311–6337.

Scholz, C. H. (1972). Static fatigue of quartz. *Journal of Geophysical Research*, 77(11):2104–2114.

Shin, D. H. and Sharma, M. M. (2014). Factors controlling the simultaneous propagation of multiple competing fractures in a horizontal well. In *SPE Hydraulic Fracturing Technology Conference*, Woodlands, TX, USA. SPE 168599.

Slocombe, R., Acock, A., Fisher, K., Viswanathan, A., Chadwick, C., Reischman, R., and Wigger, E. (2013). Eagle Ford completion optimization using horizontal log data. In *Proceedings SPE Annual Technology Conference and Exhibition*, New Orleans, Lousiana, USA. SPE 166242.

Soliman, M. Y., Hunt, J. L., and El-Raaba, A. M. (1990). Fracturing aspects of horizontal wells. *J. Pet. Tech.*, 42(8):966–973.

Swanson, P. L. (1984). Subcritical crack growth and other time- and environment-dependent behavior in crustal rocks. *J. Geophys. Res. Solid Earth*, 89(B6):4137–4152.

Tada, H., Paris, P. C., and Irwin, G. R. (2000). *The Stress Analysis of Cracks Handbook*. ASME, New York, 3rd edition.

Thomas, A. L. and Pollard, D. D. (1993). The geometry of naturally deformed rocks the geometry of echelon fractures in rock: implications from laboratory and numerical experiments. *J. Struct. Geol.*, 15(3):323 – 334.

Uwaifo, E. (2016). *Time-Dependent Initiation of Multiple Hydraulic Fractures in Rocks*. PhD thesis, University of Pittsburgh.

Williams, D. and Evans, A. (1973). A simple method for studying slow crack growth. *J. Test. Eval.*, 1(4):264–270.

Wu, K. and Olson, J. E. (2016). Mechanisms of simultaneous hydraulic-fracture propagation from multiple perforation clusters in horizontal wells. *Soc. Pet. Eng. J.*, 21(03):1000–1008.

Xu, G. and Wong, S.-W. (2013). Interaction of multiple non-planar hydraulic fractures in horizontal wells. In *IPTC 2013, International Petroleum Technology Conference*.

Zhang, X., Jeffrey, R. G., Bunger, A. P., and Thiercelin, M. (2011). Initiation and growth of a hydraulic fracture from a circular wellbore. *Int. J. Rock Mech. Min. Sci.*, 48:984–995.